Extending the operational stability of inverted Perovskite solar cells with a novel, low synthetic complexity humidity-tolerant Hole Transport Layer

Michail Loizos

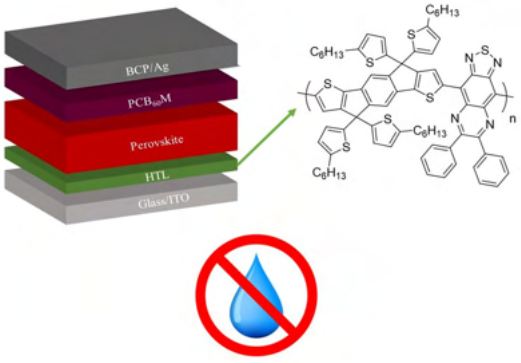

ΕΛΛΗΝΙΚΟ ΜΕΣΟΓΕΙΑΚΟ ΠΑΝΕΠΙΣΤΗΜΙΟ

A thesis presented for the degree of
Master in "Nanotechnology for Energy Applications"

Hellenic Mediterranean University
Department of Electrical & Computer engineering

Extending the operational stability of inverted Perovskite solar cells with a novel, low synthetic complexity humidity-tolerant Hole Transport Layer

Επεκτείνοντας το χρόνο ζωής περοβσκιτικών φωτοβολταϊκών κελιών ανεστραμμένης δομής με ένα νέο, χαμηλής συνθετικής πολυπλοκότητας και ανθεκτικό στην υγρασία στρώματος μεταφοράς οπών

Abstract

Organic conjugated polymers are a family of materials that are widely used as Hole Transport Layers Hole Transport Layer (HTL) in Perovskite solar cells Perovskite solar cells (PSCs). Specifically, poly(3,4-ethylenedioxythiophene) polystyrene sulfonate (PEDOT:PSS) is a widely used conjugated polymer in inverted PSCs, that suffers from poor stability. In this thesis, the operating lifetime of inverted PSCs is extended to almost 900h by employing for the first time the hydrophobic conjugated polymer Indacenodithiophene thiadiazolequinoxaline (PIDTTDQ). The performance of the optimized PIDTTDQ device reaches a maximum Power Conversion Efficiency (PCE) of 14.70%, while the corresponding one for the reference device with PEDOT:PSS is 12.16%. The enhanced PCE is due to better band alignment as well as improved HTL/Perovskite interface confirmed by Transient measurements. Time Resolved Photoluminescence (TRPL) measurements have also revealed the suppression of non-radiative recombination compared to PEDOT:PSS, which can be attributed to the reduced number of defects. The hydrophobic nature of PIDTTDQ improved the lifetime of inverted PSCs when compared to the reference device and to Polybis(4-phenyl)(2,4,6-trimethylphenyl)amine (PTAA), the most efficient HTL in inverted devices. The low cost of this material makes it a potential candidate for large area devices.

ΠΕΡΙΛΗΨΗ

Τα οργανικά συζυγιακά πολυμερή είναι μια κατηγορία υλικών η οποία χρησιμοποιείται ευρέως ως Στρώμα Μεταφοράς Οπών σε περοβσκιτικά φωτοβολταϊκά κελιά. Συγκεκριμένα, το Poly(3,4-ethylenedioxythiophene) polystyrene sulfonate (PEDOT:PSS) είναι ένα ευρέως χρησιμοποιημένο συζυγιακό πολυμερές σε περοβσκιτικά φωτοβολταϊκά κελιά ανεστραμμένης γεωμετρίας, το οποίο υποφέρει από μεγάλη αστάθεια. Σε αυτή την εργασία, ο χρόνος ζωής των ανεστραμμένων περοβσκιτικών φωτοβολταϊκών κελιών επεκτάθηκε σε σχεδόν 900 ώρες χρησιμοποιώντας για πρώτη φορά το υδρόφοβο συζυγιακό πολυμερές Indacenodithiophene Thiadiazolequinoxaline (PIDTTDQ). Η απόδοση των βελτιστοποιημένων φωτοβολταϊκών διατάξεων με το PIDTTDQ έφτασε τη μέγιστη τιμή του 14.70%, ενώ η αντίστοιχη για τις διατάξεις με PEDOT:PSS ήταν 12.16%. Η αύξηση στη κβαντική απόδοση οοφείλεται στη καλύτερη ευθυγράμμιση των ενεργειακών επιπέδων καθώς και στην βελτίωση της διεπιφάνειας ανάμεσα στο στρώμα μεταφοράς οπών και στο ενεργό στρώμα περοβσκίτη, κάτι που επιβεβαιώθηκε με χρονομεταβαλλόμενους οπτοηλεκτρονικούς χαρακτηρισμούς. Οι μετρήσεις χρονομεταβαλλόμενης φωτοφωτάυγειας έδειξαν μείωση στα επίπεδα μη ακτινοβολιτικής επανασύνδεσης σε σχέση με το PEDOT:PSS, το οποίο μπορεί να αποδοθεί στον μειωμένο αριθμό ατελειών στη διεπιφάνεια ή/και

στο ενεργό στρώμα. Η υδρόφοβη φύση του PIDTTDQ παράτεινε τον χρόνο ζωής των φωτοβολταϊκών κελιών σε σχέση με τη διάταξη αναφοράς με το PEDOT:PSS αλλά και σε σύγκριση με το Polybis(4-phenyl)(2,4,6-trimethylphenyl)amine (PTAA), το πιο αποτελεσματικό στρώμα μεταφοράς οπών σε ανεστραμμένη δομή. Το χαμηλό κόστος του υλικού αυτού το καθιστά υποψήφιο για κατασκευή φωτοβολταϊκών διατάξεων μεγαλύτερης επιφάνειας.

Acknowledgements

First off all,i would like to thank Prof. Kymakis for providing me the opportunity to work and contribute in his lab.Second, i would like to thank Dr. Chochos C.L. for his collaboration and for providing the PIDTTDQ material along with all the material related characterizations.I also thank very much Dr. Tountas M. for his collaboration,supervision and discussions regarding the experiments and the characterization methods.I also want to thank the PhD students Tzoganakis N.,Anagnostou K. and Polyzoidis C. for their guidance and help in the experimental procedures and in Cyclic Voltammetry and contact angle measurements,respectively.Finally, i would like to thank Dr.Zervos C., Chatzimanolis N. and Dr. Krassas M. for their guidance and discussions regarding the experimental protocols and the whole NANO group.

Contents

List of Figures

List of Tables

List of Acronyms

HTL

Hole Transport Layer. 38, 39, 43, 48, 49, 58, 77, 78, 86, 87, 97, 98, 103, 107, 108, 113, 114, 122, 124–127, 129, 130, 132

PSCs

Perovskite solar cells. 5, 9–12, 21–23, 25, 26, 29, 31, 33, 34, 38–49, 51, 57, 77, 89, 97, 98, 103, 114, 129–132

PEDOT:PSS

poly(3,4-ethylenedioxythiophene) polystyrene sulfonate. 21, 39, 43, 49, 97–101, 103, 106–108, 113, 114, 118, 120, 122, 124–131

PIDTTDQ

Indacenodithiophene thiadiazolequinoxaline. 98, 99, 101, 103–114, 118–120, 122, 124–132

PCE

Power Conversion Efficiency. 7, 8, 30–32, 34, 36, 38–40, 42–45, 49, 51, 67, 73, 74, 97, 98, 101, 110, 112, 114, 129, 131, 132

TRPL

Time Resolved Photoluminescence. 69–71, 124–128, 132

PTAA

Polybis(4-phenyl)(2,4,6-trimethylphenyl)amine. 22, 39, 49, 97–99, 101, 105, 106, 108, 127, 129–131

PL

Photoluminescence. 33, 48, 65–68, 124, 125

MW

Megawatt. 3

GW

Gigawatt. 3

CVD

Chemical Vapor Deposition. 4

MBE

Molecular beam epitaxy. 4

CIGS

Copper Indium Gallium Selenide. 4

DSSC

Dye Sensitized Solar cells. 5, 8, 9, 11, 38, 89

OPV's

Organic Photovoltaics. 5–7, 11, 12, 19, 21–23, 89

BHJ

Bulk Heterojunction. 6, 12

$PC_{60}BM$

Phenyl-C_{60}-butyric acid methyl ester. 6, 19, 23, 39, 43, 49, 99, 102

NFAs

Non-Fullerene Acceptors. 7

EPFL

École Polytechnique Fédérale de Lausann. 8

FTO

Fluorine Doped Tin Oxide. 8, 38

m-TiO_2

Mesoporous Titanium Dioxide. 8, 9, 38, 39

Spiro-MeOTAD

2,2',7,7'-Tetrakis[N,N-di(4-methoxyphenyl)amino]-9,9'-spirobifluorene. 9, 98

HOMO

Highest Occupied Molecular Orbital. 17, 60, 77, 78, 104, 114

LUMO

Lowest Unoccupied Molecular Orbital. 17, 60, 78

CNTs

Carbon Nanotubes. 17, 24

P3HT

Poly(3-hexylthiophene-2,5-diyl). 19, 22, 39

OLEDs

Organic Light-Emitting Diodes. 21, 22

ETL

Electron Transport Layer. 23, 39, 43, 44, 49, 58, 77, 78, 102

XRD

X-ray Diffraction. 23

FA

Formamidinium. 26, 31, 47, 48, 101

MA

Methylammonium. 26, 31, 46–48, 101

DFT

Density Functional Theory. 28

VB

Valence Band. 29, 32, 43, 66, 67, 81

V_{OC}

Open Circuit Voltage. 31, 43, 44, 67, 73, 76–78, 80, 82, 89, 90, 93, 97, 98, 112, 114, 119, 127, 131

DMSO

Dimethyl Sulfoxide. 32, 36, 99, 101

DMF

Dimethyl Formamide. 32, 36, 99, 101, 109

CB

Conduction Band. 33, 66, 67, 81

GBL

γ-Butyrolactone. 36

c-TiO_2

Compact Titanium Dioxide. 38, 39

Spiro-OMeTAD

2,2',7,7'-Tetrakis[N,N-di(4-methoxyphenyl)amino]-9,9'-spirobifluorene. 38, 39, 48, 49, 51

ITO

Indium Tin Oxide. 38, 39, 98, 100, 102, 103, 105–107, 127

CuI

Copper(I) Iodide. 39

CuSCN

Copper(I) Thiocyanate. 39

Li-TFSI

Lithium bis(trifluoromethanesulfonyl)imide. 39, 48, 49, 132

NiO_x

Nickel Oxide. 39, 43

ZnO

Zinc Oxide. 39, 49

BCP

2,9-Dimethyl-4,7-diphenyl-1,10-phenanthroline. 39, 43, 102

PFN

Poly [(9,9-bis(3'-(N,N-dimethylamino)propyl)-2,7-fluorene)-alt-2,7-(9,9–dioctylfluorene)]. 39

LiF

Lithium Fluoride. 39

Ag

Silver. 39, 102

Al

Aluminium. 39

Cu

Copper. 39

PEI

polyethylenimine. 43

FF

Fill Factor. 43, 44, 73, 75, 80–82, 112, 114

GBs

Grain Boundaries. 44, 75, 81, 82, 122

PEAI

Phenethylammonium Iodide. 44

PhenHCl

Phenformin Hydrochloride. 45

PET

Polyethylene Terephthalate. 47

tBP

4-tert-Butylpyridine. 49, 132

AFM

Atomic Force Microscopy. 55, 56, 107, 112

SEM

Scanning electron Microscopy. 56

CV

Cyclic Voltammetry. 60, 61, 63, 104

Fc

Ferrocene. 61

TCSPC

Time Correlated Single Photon Counting. 69

PMT

Photomultiplier Tubes. 69

IRF

Instrument Response Function. 70

J_{SC}

Short Circuit Current Density. 73, 78–80, 82, 84, 112, 114, 118

MPP

Maximum Power Point. 73

AM1.5G

Air Mass Global. 74, 82, 84

QFLS

Quasi-Fermi level splitting. 77, 78, 83

IQE

Internal Quantum Efficiency. 79, 80, 83

SRH

Shockley Read Hall. 80, 81

SQ

Shockley-Queisser. 80–82

EQE

External Quantum Efficiency. 82–84, 118

SCLC

Space Charge Limited Current. 85, 86, 127

TAS

Transient Absorption Spectroscopy. 88

TPV

Transient Photovoltage. 88–92, 119, 120, 122, 127

TPC

Transient Photocurrent. 88, 92, 119, 120, 122, 127

PbI_2

Lead Iodide. 98, 101

$PbBr_2$

Lead Bromide. 98, 101

CsI

Cesium Iodide. 98, 101

RbI

Rubidium Iodide. 98, 101

FAI

Formamidinium Iodide. 98, 101

MABr

Methylammonium Bromide. 99, 101

BCP

2,9-Dimethyl-4,7-diphenyl-1,10-phenanthroline-Bathocuproine. 99

NBu_4NPF_6

Tetrabutylammonium Hexafluorophosphate. 99, 104

IPA

2-Propanol. 99, 100, 102

ppm

Parts Per Million. 100

GPC

Gel permeation Chromatography. 102

NMR

Nuclear Magnetic Resonance. 102, 103

RMS

Root Mean Square. 107

SC

Synthetic Complexity. 130

Chapter 1

Introduction

1.1 Renewable Energy sources

The constant technological development of our world has caused an increase in the energy needed to satisfy our daily needs and activities. Unfortunately, many of these activities are not friendly to the environment, contributing to its growing pollution levels and therefore reducing our quality of life. A characteristic example of environmental damage is the increase of CO_2 emissions, one of the most common greenhouse gases, for more than the last 30 years, as indicated in figure 1.1 . So how can we produce energy without burdening the environment? The use of Renewable energy sources can offer a solution to this problem. Common renewable energy sources include Solar, Wind, Hydro, tidal, geothermal, and biomass energy. Their use has been growing during the past decades (orange area in figure 1.2)

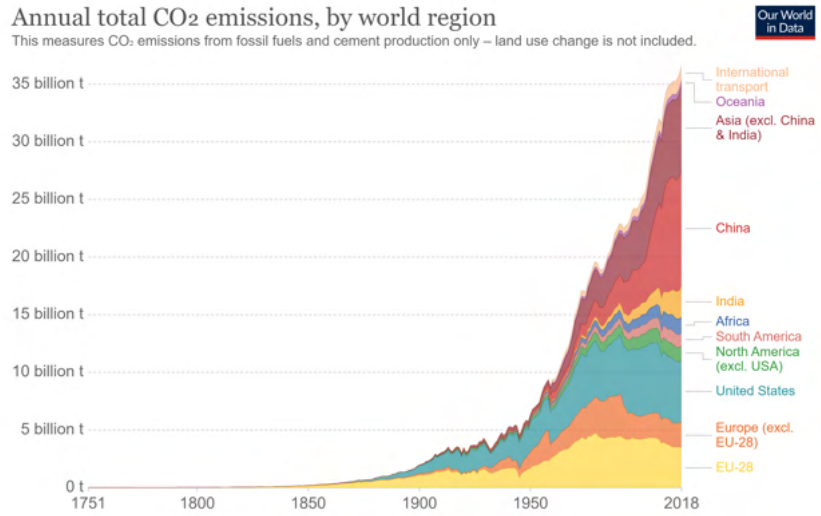

FIGURE 1.1: Total amount of CO_2 emissions per year in the world for the era 1751-2018. [1]

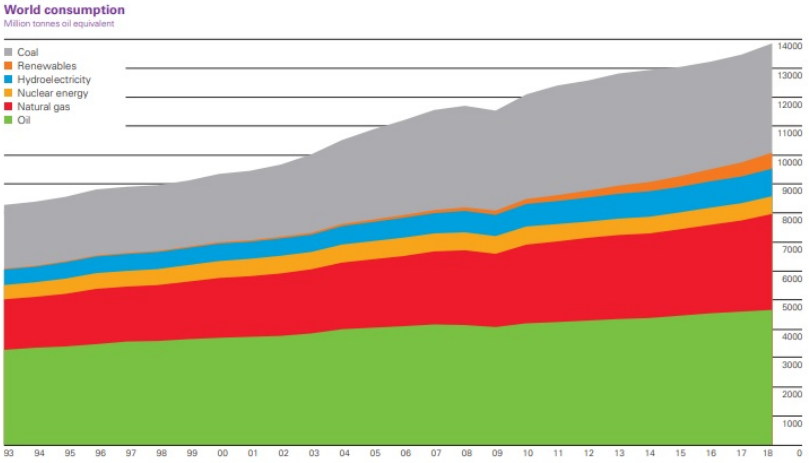

FIGURE 1.2: World Energy consumption for the last 20 years.[2]

1.2 History of solar cells

1.2.1 Discovery of the photovoltaic effect

One of the initial discoveries regarding the photovoltaic effect took place in 1839 by the Physicist Edmund Becquerel. He realized that when the two plates of a battery embedded in an electrolyte solution are illuminated by sunlight, there was an increase in the battery's measured voltage [3]. After a couple of decades, Willoughby Smith reported that Selenium can conduct current under sunlight illumination [4]. A few years later, Adams & and Day also confirmed the existence of the photovoltaic effect in selenium [5]. The first-ever solar cell device based on selenium was built by Charles Fritts in 1883 with an efficiency of converting light into electricity less than 1 % . Foundations for further improvement in photovoltaics were achieved through the observation of the photoelectric effect by Heinrich Hertz in 1887. [6], following its explanation by Albert Einstein in 1905 [7], for which he won the Nobel Prize in Physics in 1918. In general, the photovoltaic effect is comprised of the following steps: In general, photovoltaic operation is based on these steps:

- Absorption of sunlight by the light absorbing material
- Seperation of charges
- Collection of charges from the anode and the cathode respectively

1.2.2 Evolution of solar cells

For the era 1900-1950, many major findings gave room for establishing solar technology. In 1918, Jan Czochralski produced a method for crystal growth on a metal. This method will be extensively used in the future for the production of monocrystalline silicon. In 1932, the photovoltaic effect was observed in Cadmium selenide. From 1950 to 1970 solar efficiencies were improved dramatically, and new materials such as Germanium were used. The first commercial solar devices were also built for space technology applications. The decade 1970-1980 marked the evolution of the first solar companies, establishing the use of solar cells. In the following decade, solar plants were constructed using several modules, pushing the output power of a single solar plant to the range of Megawatts. The technology of solar cell production and thin-film technology kept improving, with efficiencies reaching and exceeding 20 %. Production of modules and power plants continued, with several countries involved and investing in renewable sources, reaching the decade of 2000 with the production of several Megawatt (MW) solar power plants. The commercial use of solar cells caused as a consequence further decrease of the cost per Watt of solar modules [8]. A characteristic example of the solar industry growth is showed in figure 1.3, with the vertical axis representing the PV capacity in Gigawatt (GW) and the horizontal axis is the time evolution since 2006.

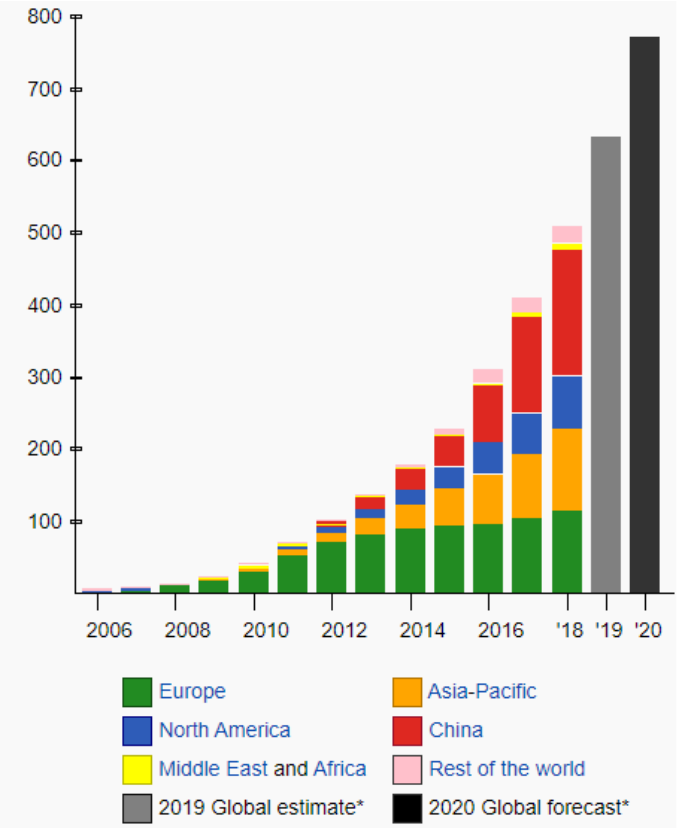

FIGURE 1.3: Capacity of PV systems (in Gigawatts) per region from 2006 until today. [9]

1.3 From silicon to perovskites

As shown in figure 1.4(a), solar cells can be divided into three generations: The first generation includes single and polycrystalline silicon-based devices. Monocrystalline silicon has the same periodic structure everywhere in the lattice, while polycrystalline silicon has a specific periodic structure for each grain (figure 1.4(b)). First-generation solar cells are the most efficient and mature technology, with the cost per Watt following a continuously declining trend, as we can see in figure 1.5. The first generation remains the most efficient compared to the second, but production costs are very high because silicon crystals are grown using very expensive, high temperature and precise methods such as Chemical Vapor Deposition (CVD) or Molecular beam epitaxy (MBE) [10].

The second generation of solar cells, which is also called thin-film generation, consists of Amorphous silicon, Copper Indium Gallium Selenide (CIGS) and Cadmium Telluride (CdTe) cells. This generation exhibits high absorption coefficients, and lower production costs compared to traditional Si cells. The photovoltaic

performance of these materials is inferior compared to traditional silicon cells. Also, another problem is the toxicity of used materials (Cd for example) and the lack of abundance [11].Third generation of thin-film solar cells include Dye Sensitized Solar cells (DSSC), Organic Photovoltaics (OPV's) and PSCs, having the potential to become a cheaper alternative to widely used first and second-generation cells. One of the main reasons to search for alternatives for silicon is to reduce fabrication costs and establish the use of solar cells using flexible substrates (for example wearables and car rooftops).

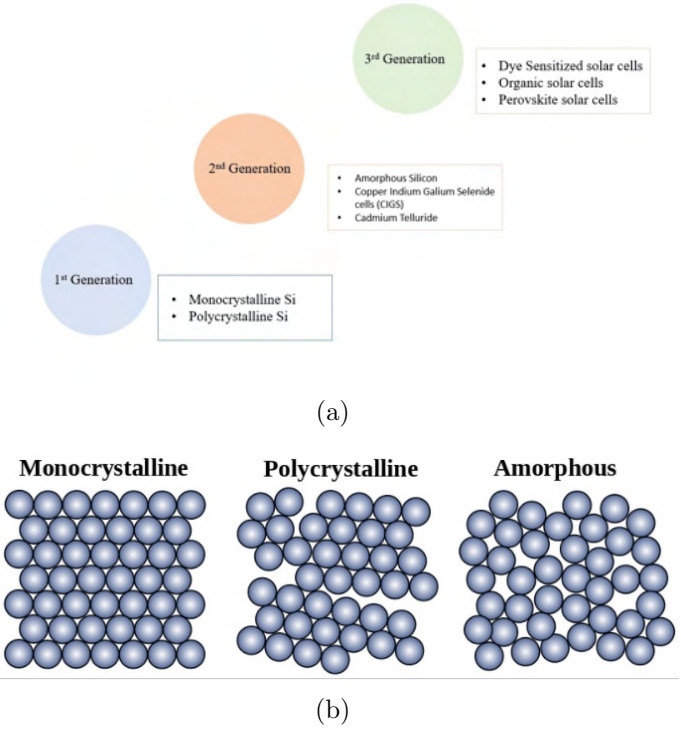

FIGURE 1.4: a)Solar cell generations ,b)Allotropic forms of silicon [12]

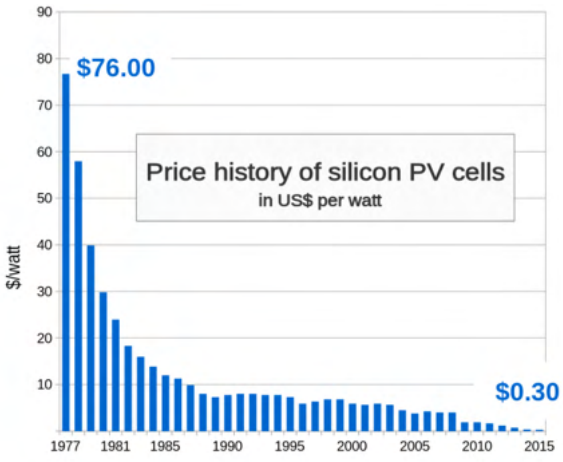

FIGURE 1.5: Cost per watt for silicon PV cells from 1977 to 2015. [13]

1.4 The emergence of Perovskite solar cells

1.4.1 Organic solar cells

The starting point of research on organic solar cells was after the realization in 1977 that polyacetylene is conductive [14]. Then, the isolation of the buckminsterfullerene C_{60} followed in 1985 [15]. The isolation of the fullerene molecule followed the discovery that electrons can transfer from a conductive polymer to the fullerene, which led the way for the fabrication of OPV's. Even though the first organic solar cell was fabricated in 1958, the efficiency was very poor. During the period 1991-1995 the first Bulk Heterojunction devices composed of a polymer-C_{60} active layer were fabricated. Initially, the first organic devices consisted of a bilayer structure, that is a polymer film with the fullerene thin film on top. However, this configuration is not very efficient. The reason is that the bound electron-hole pairs (excitons) that are formed have high binding energy, on the order of 0.5-1eV [16], therefore the bound exciton state can separate only in the polymer-fullerene interface. The high exciton binding energy is due to the low permittivities of organic materials that result in insufficient Coulomb potential screening. The main drawback of the bilayer structure is that the carrier diffusion length is small in OPV's, $\approx$ 1-10nm [17, 18], which means that a limited amount of excitons reaches the polymer-fullerene interface to dissociate and inject at the respective electrodes. To overcome this obstacle, a more efficient morphology was employed, which is called Bulk Heterojunction (BHJ) and is achieved by mixing the polymer-fullerene blend. The bilayer and BHJ morphologies are illustrated in figure 1.6.

The polymer-fullerene Heterojunction blend is called the Donor-Acceptor blend. The electron donor is a p-type material while the electron acceptor is a p-type material. A common donor-acceptor blend is the conjugated polymer P3HT and the fullerene derivative Phenyl-C_{60}-butyric acid methyl ester ($PC_{60}BM$), which contains chemical groups that improve solubility in common solvents such as Chlorobenzene. The photovoltaic effect in OPV's consists of the following steps:

- Light absorption by the Donor-acceptor blend
- The excitation of an electron from the Donor HOMO to LUMO, leaving behind a hole. The electron and hole form a bound state through Coulomb interaction, the exciton.

- The exciton separation in the Donor-Acceptor interface. The separation occurs when the energy offset between the LUMO of the donor and the acceptor is larger than the exciton binding energy
- Charge Collection. The separated electrons and holes reach the cathode and the anode through the assistance of electron and hole transport layers that sandwich the active layer

Because of the reasons mentioned, the PCE of OPV's is typically low, on the order of 4.5-5% [19]. However, the use of fullerene acceptors raises some concerns, which include weak absorption in visible and IR region, thermal and chemical instability, and high production cost. Since 2015 many organic materials Non-Fullerene Acceptors (NFAs) were employed [20]. These materials tackle these problems and improved dramatically the PCE of OPV's, reaching even a PCE of 18.4 % [21]. The merits OPV's offer are the following [22]:

- Use of cheap organic materials with low toxicity
- High absorption coefficients
- Easy, low-temperature processing from solution, with potential to reduce cost in large-area devices.

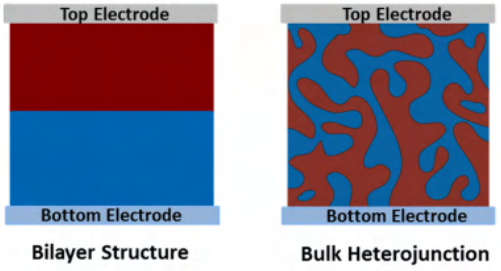

FIGURE 1.6: Bilayer structure and Bulk Heterojunction blend in OPVs [23]

1.4.2 Dye sensitized solar cells

Main advantages of the third-generation solar cell are the ability to fabricate devices using low-temperature, solution-processed techniques resulting in lower fabrication costs, the adjustable bandgap of the absorbing material along the ability to produce flexible substrates. The main concerns for these materials are toxicity (most perovskite-based devices contain lead) along with instability while exposed

to oxygen, moisture, and heat [24, 25]. Regarding perovskite solar cells(PSCs), their emergence arises from dye-sensitized solar cells.

DSSC (or Grätzel cell) were invented for the first time in 1988 by Michael Grätzel and Brian O'Regan at UC Berkeley. They later moved on École Polytechnique Fédérale de Lausann (EPFL) where they published in 1991 the first work on high-efficiency Dye-sensitized solar cells [26]. A DSSC consists of the following:(figure 1.7) glass, a transparent conductive anode, (usually Fluorine Doped Tin Oxide (FTO)), a liquid electrolyte, and a mesoporous oxide. Mesoporous Titanium Dioxide (m-TiO_2) (n-type semiconductor), a dye (ruthenium is widely used % [27]) which is attached with covalent bonds on the surface of the oxide and enhances light absorption and finally a cathode (also known as counter electrode) attached to glass, typically Platinum.

Operational principle of dye-sensitized solar cell can be summarized as follows [28]:

- Light enters the transparent conductive oxide and reaches titanium dioxide, where light is absorbed by the dye, exciting an electron
- The excited electron diffuses from titanium dioxide into the transparent oxide and enters the outside circuit giving power to a load. The dye now is oxidized, and gains the lost electron from I_3^- ions, reducing the dye at its initial form, $3I^- \longrightarrow I_3^- + 2e^-$
- The electron travels through the counter electrode and enters again the cell where it reaches the electrolyte
- The electron returns to the dye through the electrolyte. The electron causes reduction of iodide ions : $I_3^- + 2e^- \longrightarrow 3I^-$

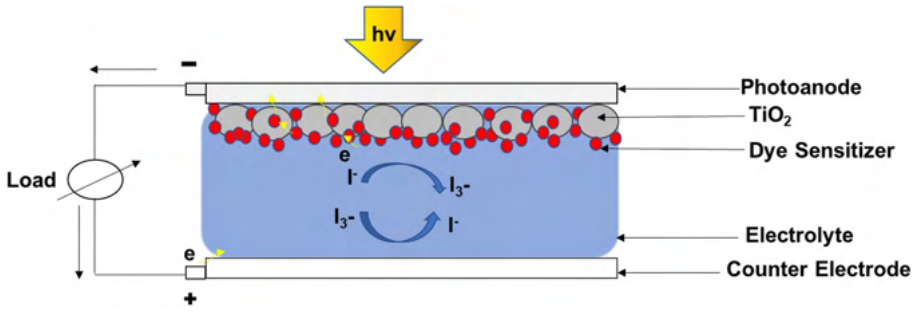

FIGURE 1.7: Schematic presentation of a DSSC. [29]

Typical PCE of DSSC's ranges to approximately 10 % [27] and have exceeded 12 % [30]

One of the main advantages of this technology is that it reduces fabrication costs compared to silicon. Furthermore, these cells can operate in wide angles and can work in non-ideal conditions such as low illumination or during a cloudy day. While the performance of inorganic materials such as silicon deteriorates with temperature as we will see in chapter 2, this problem is no longer met in DSSC's. Also, these materials are solely based on electrons, resulting in insignificant recombination effects.

On the other hand, a major drawback for DSSC's is the use of a liquid electrolyte. The material can freeze at low temperatures or start evaporating at high temperature, causing leakage of solvents which can be hazardous for humans. Because of the use of the electrolyte, there is a limit in achieved efficiencies which limits further improvement of measured efficiencies [28].

1.4.3 Brief history of Perovskite solar cells

The first milestone for the transition to PSCs was to replace the liquid electrolyte with another material called spirobifluorene, which acts as a hole transport layer. [27].A first attempt to fabricate perovskite-based devices was reported back in 2009 [31], with an efficiency of 3.8 %. Another effort in 2011 pushed the efficiency to 6.5 % [32], using the perovskite as a sensitizer along with m-TiO_2.However, the device degraded fast because the perovskite dissolves quickly in the electrolyte solution. In 2012, measured efficiency was increased to 9 % by using the material 2,2',7,7'-Tetrakis[N,N-di(4-methoxyphenyl)amino]-9,9'-spirobifluorene (Spiro-MeOTAD) and thermally evaporating a gold electrode on top as the anode [33]. After the replacement of the liquid electrolyte and the use of a hole transport layer, a series of efficiency records have been achieved. This was achieved by improving the fabrication conditions and methods along with simultaneous efforts to improve the measuring protocols and studying phenomena related to device operation such as hysteresis [34]. By 2015, the efficiency of PSCs has reached 21.0 %, becoming a serious rival to first and second-generation solar cells. In 2021, the efficiency of PSCs has reached 25 % [35]. The rapid evolution of efficiency, compared with other generations of solar cells, is shown in figure 1.8(a), where it is evident that efficiency exceeded 21 % in less than a decade, making PSCs the most rapidly evolving solar technology. Figure 1.8(b) shows the exponential increase in publications regarding PSCs, which is a characteristic of the research interest and the amount of effort put into improving device quality.

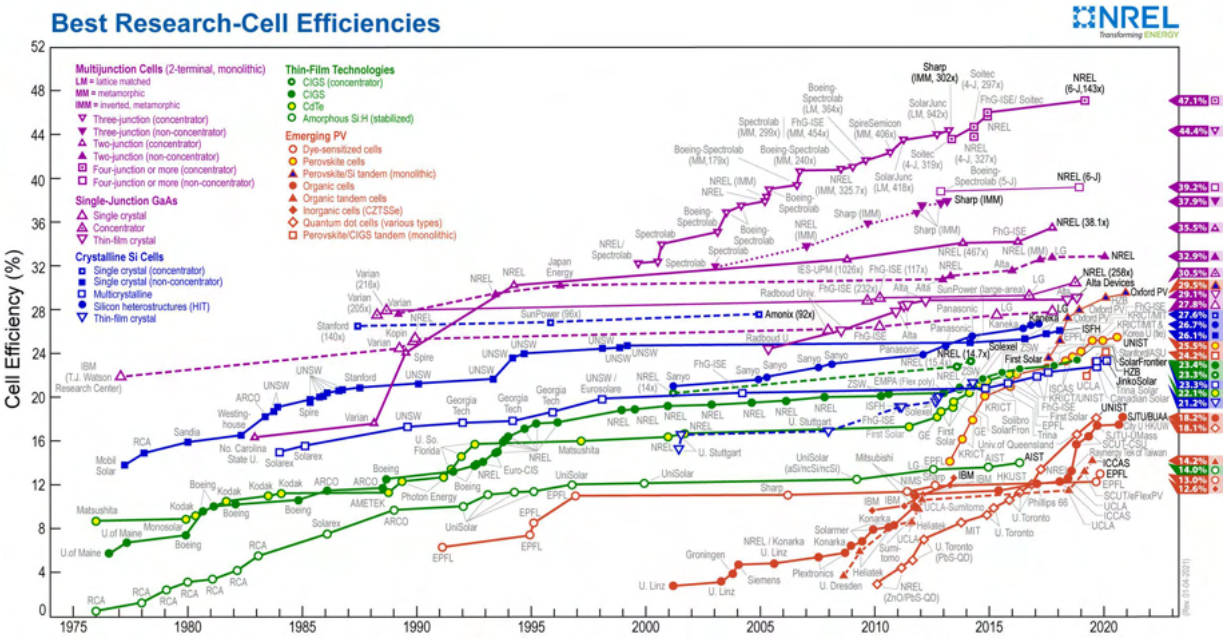

(a)

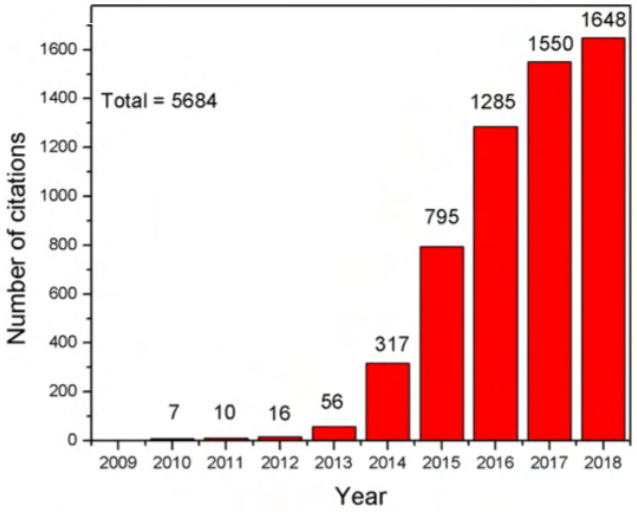

(b)

FIGURE 1.8: a)Number of publications per year for PSCs, b)NREL's efficiency chart for all PV technologies.[36, 37]

1.4.4 The sweet spot for solar technology

While the cost per watt of PSCs is less than half the cost per watt for Si solar cells according to figure 1.9(a), and measured efficiencies are very close, the main issue is operational stability. The sweet spot for any solar cell is being optimized in terms of cost, efficiency, and stability, as shown in figure 1.9(b).

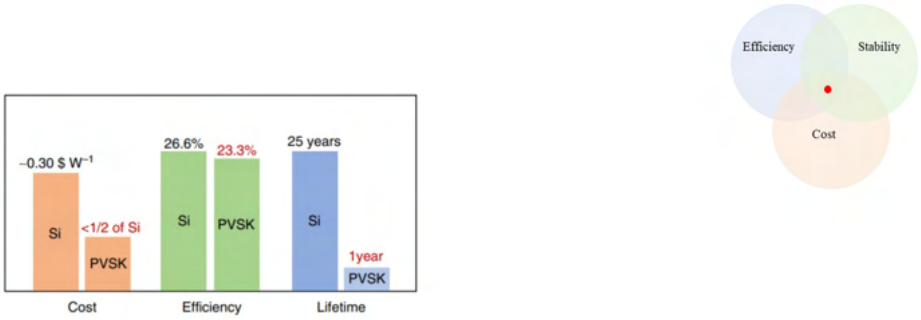

(a) (b)

FIGURE 1.9: a) Comparison between Si and PSCs [38], b)the sweet spot for solar technology .

1.5 An introduction to perovskite solar cells

Perovskite solar cells are an emerging, constantly developing technology with a potential for commercial use either as standalone or in a tandem architecture along with Silicon.

PSCs promise to remove the obstacles of OPV's and DSSC and produce high efficiency solar cells, having the following advantages and disadvantages [39–41]:

- High absorption coefficient
- Adjustable bandgap
- Fabrication using low-cost , solution-processed techniques.
- Low effective mass, high mobility and long diffusion lengths
- Ability to fabricate flexible, large area substrates

Disadvantages:

- Lead toxicity
- Degradation under exposure in oxygen, moisture, heat and continuous light illumination that reduce operational stability of devices. For instance, Si solar panels come with a guarantee a lifetime of $\approx$ 25 years [42], while the highest lifetime for PSCs is 1 year [43, 44].
- Structural instability

The principles of operation of PSCs are similar to those of OPV's, but the perovskite absorber has some advantages compared to BHJ blends. These include high mobilities that can be comparable with inorganic materials [45] and diffusion lengths on the order of a few μm. [46].The photovoltaic effect in perovskites involves the formation of a low exciton binding energy that dissociates and the hole and electron are diffusing through the respective charge selective contacts and is collected at the respective electrode.

Chapter 2

Organic semiconductors and Conjugated polymers

2.1 From Inorganic to organic materials

The properties of inorganic semiconductors are well known and widely studied. For the past 3 decades, another family of semiconductors based on organic materials has emerged. The main advantage of organic materials when compared to the inorganic is the low cost and the low-temperature processing based on solutions, which reduces fabrication cost for various types of devices (LEDs, transistors, solar cells, photodetectors, etc.), This enables the fabrication of large-area devices for commercial use. The main difference between organic and inorganic semiconductors is the charge transfer mechanism. In general, the main disadvantage of organic semiconductors is that they suffer from low mobilities when compared to inorganic materials. The term organic semiconductors refers to materials with weak intermolecular interactions (π bonding) and conjugated polymers. The latter is composed mainly of carbon and hydrogen atoms that might contain heteroatoms such as Nitrogen, sulfur, oxygen, or fluorine [47]. These materials remain bound mainly through weak Van Der Waals Interactions, which affects their electrical properties [48]. Conjugated materials are successfully employed in a variety of applications as it can be seen in figure 2.1

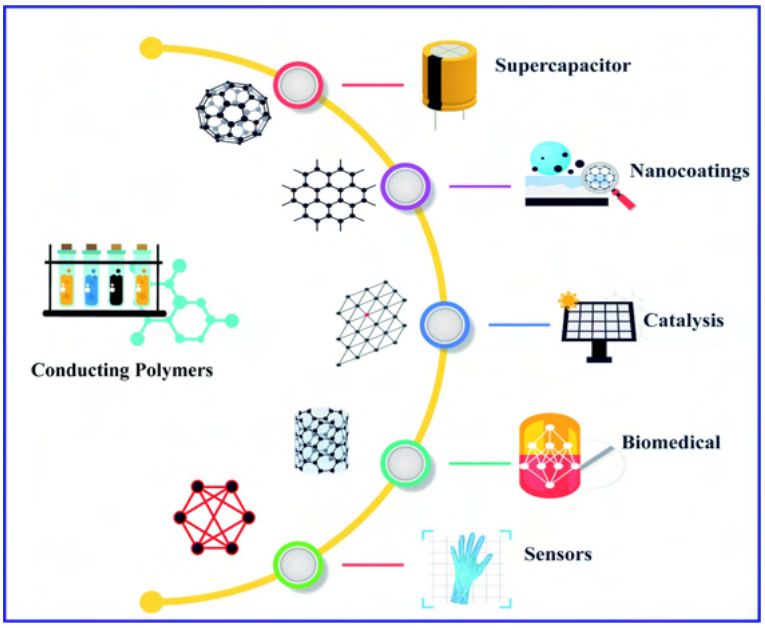

FIGURE 2.1: Applications of conjugated polymers.[49]

2.2 π-Bond Molecules

The main conduction mechanism in organic semiconductors arises from π- electrons. To be able to explain the conductivity of organic semiconductors, we need to take a closer look at π bond systems. π electrons stem from sp^2 or sp^3 hybridized atoms. The molecule will then obtain a 3D tetrahedral shape. Two representative examples are provided in figure 2.2 For the case of ethene (C_2H_4), a sp^2 hybridization occurs.The electron configuration of a carbon atom is $1s^2 2s^2 2p^2$. The 2s orbital lies lower in energy than the 2p orbital, but all of them belong to the valence orbital (n=2) of carbon and can participate in chemical bonding. To create a bond with the second carbon atom, in each carbon atom one 2s electron will transfer to the third empty p-orbital while the remaining 2s electron will raise its energy and reach the 2p orbital. The third electron transferred to the third empty 2p orbital will further rise in energy. This will result in 3 hybridized sp^2 orbitals with an energy between the energies of the initials and p orbitals, and an unhybridized p orbital. When the ethene molecule is formed, the carbon atoms will form a strong σ bond in the x-axis along with their nuclei and a weak π bond that lies in a plane perpendicular to that of the sigma bond, in the z-axis. The s orbitals of the 4 hydrogen atoms will overlap with the remaining 2 sp^2 orbitals in such a way as to minimize their energy. The molecule will then form on a 2D plane. Similar reasoning can be followed for the case of the acetylene molecule (C_2H_2). In this

case, one of the 2s electrons will transfer to the third unoccupied p orbital. Then, the remaining 2s electron and one p orbital electron will form a hybrid orbital. The remaining 2p electrons will raise in energy and remain unhybridized. This will lead to 1 sp^1 orbital with energy intermediate to the initials and p orbitals. The formed molecule will be linear (1D). The triple C-C bond is then composed of one sigma bond along the x-axis and 2 weak π bonds along the z and y-axis. The 2 s orbitals of hydrogen atoms will overlap with the remaining electrons that occupy the sp^1 orbital along the x-axis. The triple bond is stronger than the double due to the presence of an extra π bond, and the double bond is also stronger than the single bond.

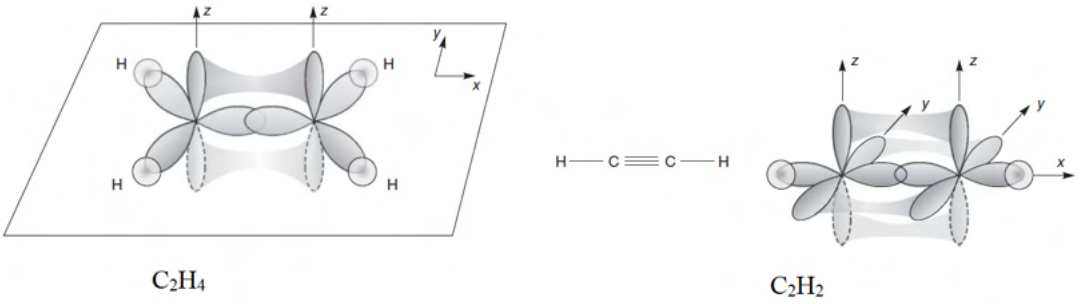

FIGURE 2.2: The formation of ethene (C_2H_4) and acetylene (C_2H_2) molecules through hybridization [50]

2.3 Delocalization

To explain the concept of delocalization, we will use as reference the Benzene molecule. A benzene molecule is shown in figure 2.3. The present double bonds between carbon atoms give the molecule a planar geometry. However, we concluded previously that double bonds are stronger than single bonds, which could give the molecule a non-perfect, hexagonal structure, as the length of the double bond is smaller than that of a single bond. In contrast, experimental results show that the bond length between all 6 carbon bonds is the same [51], giving the molecule a perfect hexagonal structure. This is due to delocalization. The classical Valence bond theory assumes that all formed bonds are localized between adjacent atoms, where each one contributes to the bonding by offering valence electrons. This assumption leads to errors as in the case of Benzene. The chemical bonds are not necessarily localized, which means that if electrons can lower their energy by moving further away from adjacent atoms, this movement will be more preferable. As a consequence, the π electrons in Benzene will further extend their

wavefunctions along the hexagonal chain which will lower their energy. This will lead to a delocalized motion along the hexagonal chain. As depicted in figure 2.4 , the delocalized electrons leave behind carbon ions, which will equally attract the delocalized electrons and act as attractive potential wells. Despite the presence of delocalized electrons that can be considered "free", benzene cannot conduct electricity. The main reason is the limited movement of delocalized electrons along with the hexagon which makes it impossible for them to "jump" to another molecule.

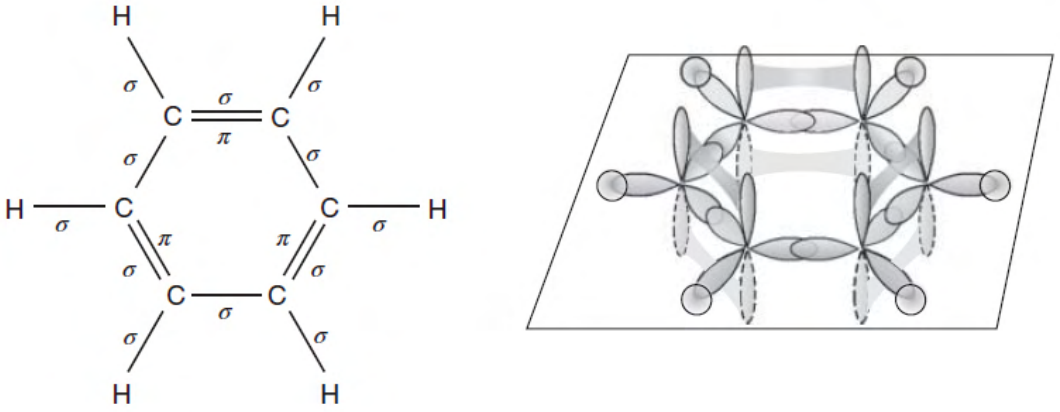

FIGURE 2.3: The planar Benzene molecule with indicated σ and π bonds and it's orbital stucture.[50]

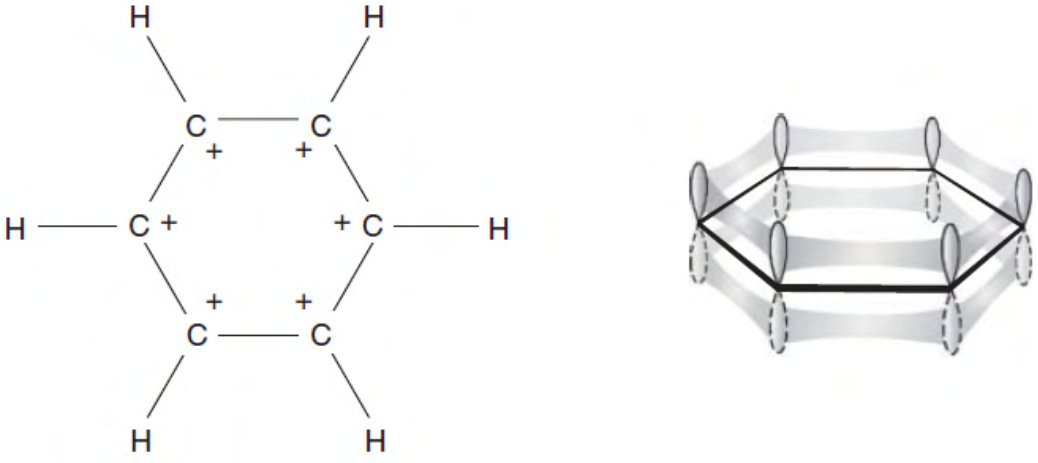

FIGURE 2.4: Delocalization in Benzene.π electrons are free to move in the hexagonal chain, where they are attracted from positive carbon ions [50]

2.4 Molecular energy levels and Conjugation

When a molecule is formed, the energy levels of the molecule will be modified compared to the single atoms that are composed of. The simplest molecule to start is the hydrogen molecule. The molecule is composed of two hydrogen atoms with a $1s^1$ configuration. The 2 1s orbitals will form the molecule. The resulting molecule will also be composed of 2 orbitals because we started with 2 orbitals. The first strong bonding σ_{1s} molecular orbital will lie lower in energy than the atomic 1s orbitals because electrons in the hydrogen molecule are now interacting with both hydrogen atom nuclei, which lowers their energy. This orbital is called the bonding orbital. The second formed σ^*_{1s} orbital will be empty and will lie higher in energy than the separate 1s atomic orbitals, and is called an anti-bonding orbital. The formation of the hydrogen molecule is shown in figure 2.5. The bonding σ_{1s} orbital is called the Highest Occupied Molecular Orbital (HOMO), while the anti-bonding σ^*_{1s} orbital is the Lowest Unoccupied Molecular Orbital (LUMO). Similar reasoning can be applied to the case of organic materials.

Let us now return to the case of the ethene molecule. There are in total 2 π electrons, one from each carbon atom. Again, there must be 2 molecular orbitals, equal in number to the 2 initial unhybridized p orbitals. The first one will be the bonding π orbital and the second one the antibonding π^* orbital. The overlapping of the two unhybridized p orbitals can be achieved by two possible scenarios, as shown in figure 2.6(a) : Either the orbitals combine constructively, which corresponds to the bonding case, or they combine destructively, which corresponds to a higher energy state. In the destructive case, a node is formed between the combined orbitals. A node represents a spatial area where the probability of finding an electron is very small due to the small overlapping of the wavefunctions. Now for the case of the sigma molecular orbitals, electrons will occupy the energetically favorable σ bonding molecular orbital. The stronger σ bonding results in a larger energy gap between the bonding and antibonding molecular orbitals, as seen from figure 2.6(b) . The energy gap between the two π bonding and antibonding orbitals corresponds to the smallest electronic energy transition of the molecule. This means that the HOMO level is the π energy level and the LUMO is the π^* level. Organic compounds which contain a series of connected p orbitals with delocalized electrons set up a Conjugated system. Conjugated materials include compounds such as conductive polymers, graphite, graphene, and derivatives such as Carbon Nanotubes (CNTs), small molecules, porphyrins and several aromatic and non-aromatic compounds. Many of these materials have been successfully employed in

photovoltaic devices. Here, we will mainly focus on Conjugated polymers.

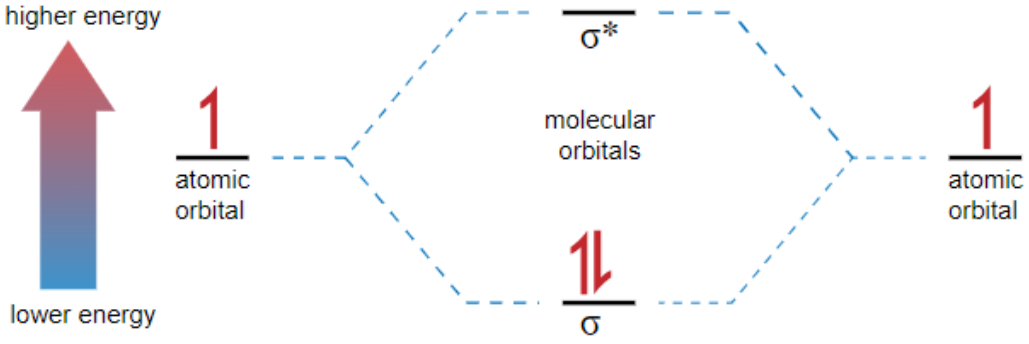

FIGURE 2.5: Formation of molecular energy levels in the Hydrogen Molecule. [52]

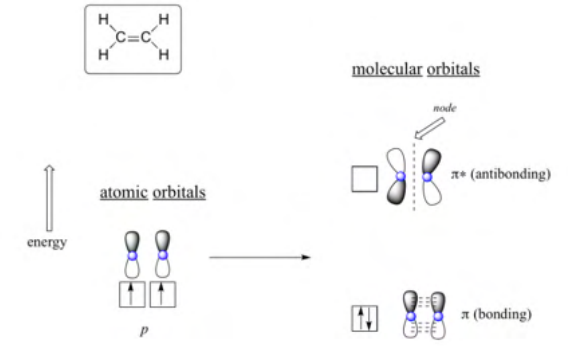

(a)

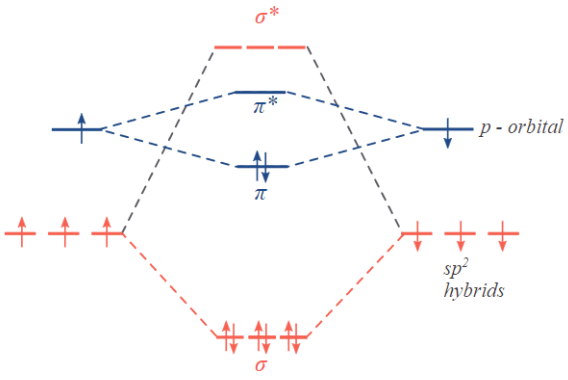

(b)

FIGURE 2.6: a)Orbital overlapping scenarios of π electrons in ethene.[53],b)Molecular energy level occupation in the ethene molecule.[54]

2.5 Conjugated Polymers

2.5.1 Brief History

The word "polymer" was used for the first time in 1832. Two years after, the first report on the polyaniline molecule, the first-ever conjugated polymer came out. Efforts to establish the use of conjugated polymers as we know them today date back to 1960, from the research of Donald Weiss on polypyrrole and the work of *Rene* Buvet and Marcel Jozefowicz on polyanilines [55]. Almost a decade later, in 1977, Hideki Shirakawa reported the synthesis of halogen derivatives of polyacetylene [56].MacDiarmid and Heeger also contributed to the field by studying the Poly(sulfur nitride) molecule and by performing a series of modifications in the polyacetylene molecule such as doping or efforts to improve its purity and study its effect on the material conductivity. The two latter along with Shirakawa won the Nobel Prize in Chemistry in 2000 for their contributions. In 1970 another π compound was discovered and isolated, the Buckminsterfullerene [15]. The fabrication of the first OPV's started in 1986. In 1992, the Poly(3-hexylthiophene-2,5-diyl) (P3HT) conjugated polymer was synthesized and used in OPV's [57, 58].Then, the discovery that due to the limited solubility of the pure fullerene, another derivative was produced, $PC_{60}BM$, which is soluble in common solvents and used in OPV's as stated in section 1.4.1, which expanded the use of OPV's

2.5.2 Conduction Mechanism and Charge Transport

Conjugated polymers are usually made of a macromolecule chain where a chemical structure is repeated several times. This structure is the monomer. This chain is called the backbone of the polymer. In this chain, several chemical groups or heteroatoms might be attached to the backbone. The delocalized electrons are in the backbone of the polymer. The chain might have carbon atoms connected with single or alternating single-double bonds. This is illustrated in the polyacetylene molecule in figure 2.7, where the carbon atoms make up the backbone of the polymer. The formation of bands in conjugated polymers is shown in figure 2.8. As the number of monomers increases, the number of π electrons increases, occupying more energy levels with a very small spacing which eventually leads to the formation of the two bands, similarly with solid crystals. The energy gap is the bandgap of the polymer.

The conductivity of undoped conjugated polymers ranges from nearly metallic to insulator, as shown in figure 2.9. This results in bandgaps larger than 2eV. The low conductivity of undoped polymers can change even several orders of magnitude after a small amount of doping. Doping can be achieved either by oxidation (mainly), which corresponds to the removal of delocalized electrons or by reduction (addition of an electron in an unfilled band) [59]. A higher degree of crystallinity in the material can also lead to improved conductivity. In the case of oxidation/reduction processes, charged ions are left behind after the addition or removal of an electron in the molecule. These ions in the molecular crystal can be displaced from their equilibrium positions since they can oscillate around them. Crystal oscillations are called phonons. The ions can interact with the free electrons, the so-called electron-phonon coupling. A molecular crystal has also defects as in the case of any inorganic crystal. These defects can trap the free electrons and create a bound state, a quasi-particle called Polaron. A polaron quasi-particle has an increased effective mass and decreased mobility. The conduction mechanism relies on the hopping of the electron between the defects. The term hopping refers to electrons that can be found in a smaller area than the total area of the material, meaning that their wave function is located in this smaller area. Polaronic effects are strong in presence in organic semiconductors and one of the main reasons for the low obtained mobilities and conductivities. Organic materials are in general highly disordered systems and sometimes considered amorphous, meaning that they possess a significantly larger defect population. These defects produce potential wells which can trap electrons and limit the conduction of these molecules, as the wavefunction is localized in the trap region. The only possible way for conduction is then tunneling the electrons from one potential well to another. However, if the spacing between the impurities is high, then the conduction is very poor, we have an insulating behavior.

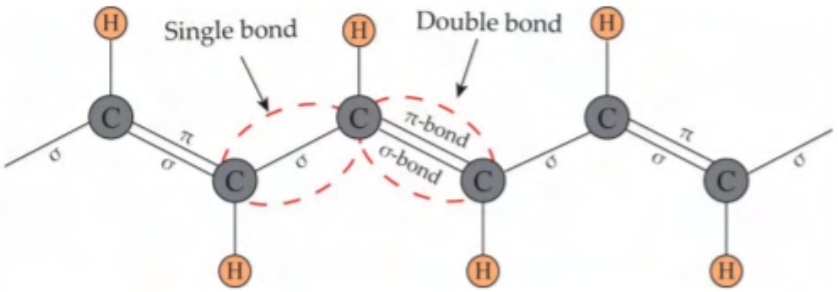

FIGURE 2.7: Polyacetylene molecular structure.The connected carbon atoms make up the backbone of the polymer.[60]

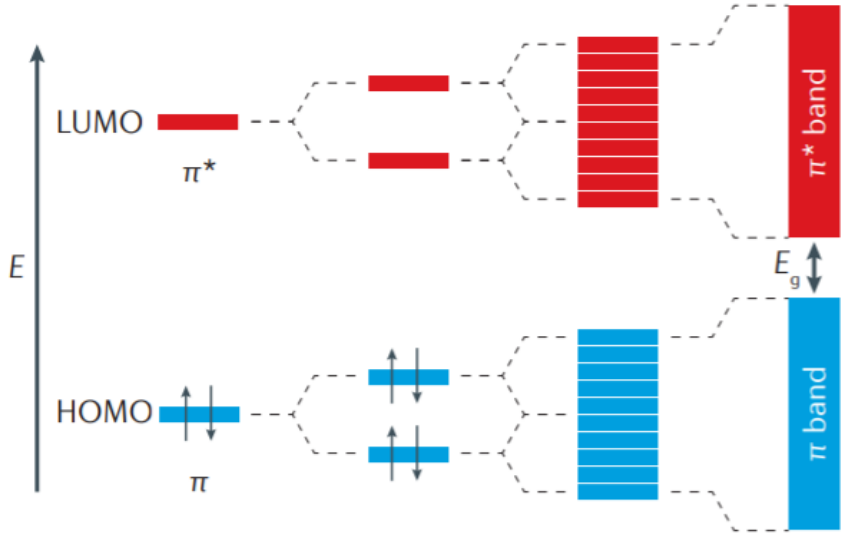

FIGURE 2.8: Band formation in conjugated polymers. [61]

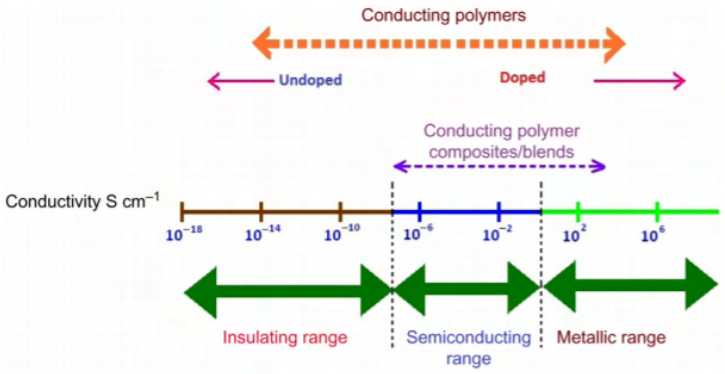

FIGURE 2.9: Range of conductivity values of Conjugated Polymers [62]

2.6 Common π conjugated systems and applications

2.6.1 Conjugated Polymers

PEDOT:PSS: PEDOT:PSS is a common conjugated polymer used in a wide range of applications in thin-film electronics:It has been successfully employed in Organic Light-Emitting Diodes (OLEDs), organic transistors, OPV's , PSCs and sensors. [63–68]. PEDOT:PSS films are deposited by an aqueous dispersion using various thin film deposition methods such as spin coating, slot die coating, doctor blade, spray coating, inkjet, and screen printing. It is cheap and suitable

for low-temperature processing and produces smooth and uniform films with low roughness. It is transparent in visible wavelengths (transparency $> 80\%$) and has an acceptable conductivity which can be tuned by various methods as we will see. The energy levels of the material are suitable for the various electronic applications that it is used. The main drawbacks of PEDOT that we will further examine are the acidic and aqueous nature, which reduce device stability [69]. The chemical structure of PEDOT:PSS is shown in figure 2.10(a).

P3HT: P3HT is another common conjugated polymer employed in a variety of organic electronic devices such as thin-film transistors, OPV's, PSCs and sensors. [70–74]. It possesses a low bandgap of ≈ 1.9 eV and relatively high hole mobility for an organic material. It also produces transparent uniform films with a low cost and ability to use in large-area devices [75]. The chemical structure of P3HT is shown in figure 2.10(b)

PTAA: PTAA is a conjugated polymer which is employed in a variety of organic electronic devices such as OLEDs, transistors, and PSCs [76–78]. It is also transparent as it absorbs mainly in the UV region, and produces uniform films with low roughness. Even though it has been successfully employed in high-efficiency perovskite solar cells, the main drawback of the material is the high cost, therefore it is not employed in large-area devices. The chemical structure of PTAA is illustrated in figure 2.10(c)

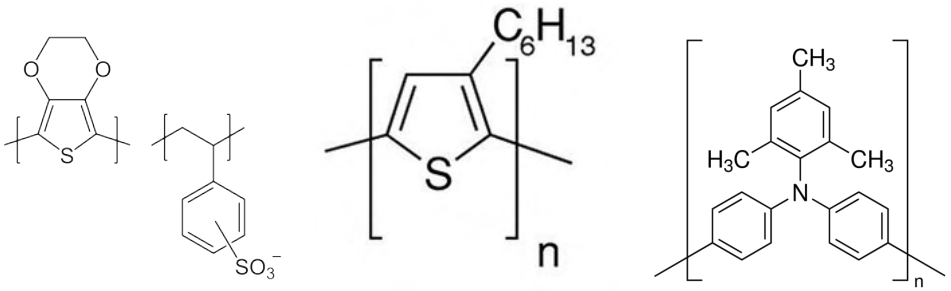

(a) (b) (c)

FIGURE 2.10: a)PEDOT:PSS chemical structure [79],b)P3HT chemical structure [80],c)PTAA chemical structure [81]

2.6.2 Other π bond materials

Fullerene & Derrivatives: Fullerene and its derivatives have been extensively used in organic electronics. Fullerenes are usually employed in organic electronic devices such as Transistors,OLEDs, PSCs, sensors and as an electron acceptor in

OPV's [82–84]. They are also used as Electron Transport Layer (ETL).Typically, fullerenes employed in organic electronics are in the form of C_{60} or $PC_{60}BM$ or $PC_{70}BM$.The chemical structure of the fullerene derivative is presented in figure 2.11 The difference between the former 2 materials is the extension of the absorption range in visible wavelengths in the case of $PC_{70}BM$. Fullerene derivatives are used as a solution,as discussed earlier, while C_{60} is deposited through thermal evaporation due to poor solubility in common solvents. The main disadvantage of employing fullerenes in organic devices is the very high cost, a reason that led to the synthesis of non-fullerene acceptors in OPV's. However, fullerenes are still employed in inverted PSCs.

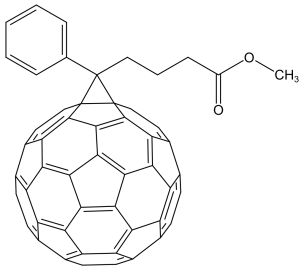

FIGURE 2.11: The chemical structure of $PC_{60}BM$ [85]

Graphite and its derivatives: There are several allotropic forms of carbon as shown in figure 2.12. Graphite, which is used in pencils and lubricants, is another material where π conjugation exists. Graphite has a hexagonal structure of sp^2 bonded carbon atoms, which results in strong σ bonds. The delocalized π electrons are located in the plane vertical to the bonded carbon atoms. Graphite is a good conductor of electricity and heat.

Graphite is composed of several stacked graphene monolayers, as it has been found from the isolation of graphene in 2004 by Andre Geim and Konstantin Novoselov by the scotch tape method [86]. All the Graphene monolayers interact through a non-covalent interaction called π -π stacking. This interaction occurs between aromatic rings because of the presence of π electrons and can be experimentally confirmed by X-ray Diffraction (XRD) techniques. There is evidence for the presence of π-π stacking in both Graphite and Benzene that we studied previously. Furthermore, the non-covalent nature of this interaction assists the process of supramolecular assembly where molecules are held by non-covalent interactions [87]. Similarly to graphite, Graphene has a hexagonal "honeycomb" lattice structure with π electrons (2.12(c),2.12(b)) and it is a very good conductor of electricity as it is considered semimetal, a semiconductor of zero bandgap since it

has a zero bandgap as the two π, π^* bands formed are half-filled with free electrons. Graphene has been used in a series of applications including biomedical, coatings, electronics, energy, membranes, and sensor research. Another allotropic form of carbon is CNTs with a nanometer diameter. CNTs have been employed in thin-film electronics, Biomedical applications, coatings, composite materials, energy storage, and coatings.

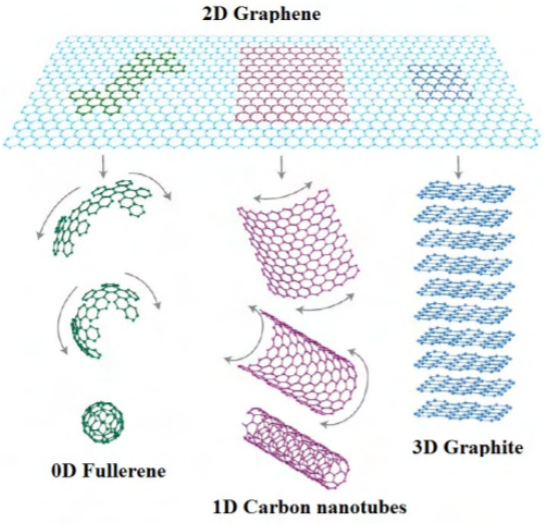

(a)

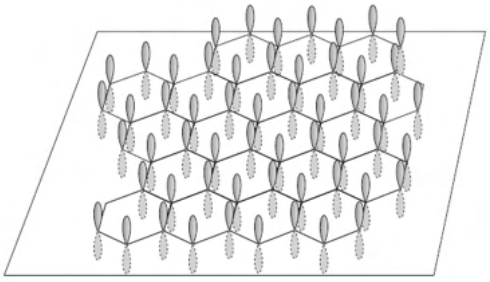

(b)

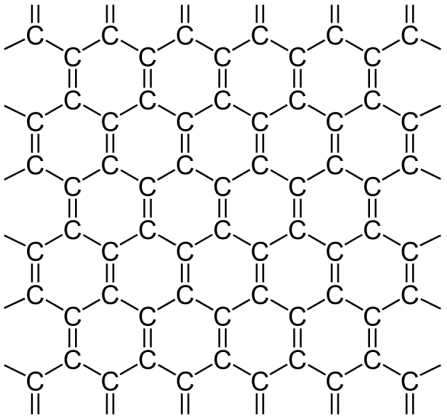

(c)

FIGURE 2.12: a)Allotropic forms of carbon [88],b)The honeycomb lattice of Graphene with indicated π electrons [50],c)and Double bonds of sp^2 hybridized carbon atoms in Graphene [89]

Chapter 3

An overview on Perovskite Materials and devices

3.1 Perovskite Compounds and structure

Perovskite is a mineral that was discovered in 1839 by Gustav Rose. The mineral had the structure $CaTiO_3$. The name perovskite was adopted by the name of the Russian mineralogist L. A Perovskiy [90]. After this discovery, several other compounds such as $BaTiO_3$,$PbTiO_3$,$SrTiO_3$ were discovered to possess the perovskite structure, so commonly perovskite compounds are metal oxides with the structure ABO_3.

These materials did not possess good semiconductor properties and could not be used for photovoltaic applications. The perovskite oxides exhibit both ferroelectric and piezoelectric properties [91] mainly. Almost two decades back, the idea of fabricating highly efficient PSCs from solution was a fiction. However, the replacement of the oxides with halogen anions could be a potential fit for use in photovoltaics due to the suitable semiconducting properties. In general, the perovskite structure is a crystal structure of the form ABX_3, where A is a monovalent cation, B is a divalent cation, and X is a monovalent anion. These atoms have the orientation as shown in figure 3.1. In this structure, the B cations occupy the 12 corners of the cube, the A cation is at a body-center position and the X anions are in face-centered like positions. In the second equivalent structure, the A cations are now occupying the corners of the cube, the B cation is at a body center position and the X anions are still at the faces of the cube.

Over the years, a variety of different elements and compounds have been employed in perovskites. Different elements have been used for each of the A, B,

X components, as pictured in table 3.1. Formamidinium (FA) ($(CH_3)_2NH_2^+$) and Methylammonium (MA) ($CH_3NH_3^+$)are used as components as FA and MA based materials posses good semiconductor properties and can be used in PSCs. So is it possible to form a perovskite structure with any combination or even more materials than the ones listed in 3.1? Are there any criteria that determine whether a crystal structure will be a perovskite? The answer to this question is the tolerance factor (τ) proposed by Goldschmidt [92]. This empirical rule determines whether a certain combination of elements and compounds will form a perovskite crystal or not, based on the ionic radii of each compound. The tolerance factor is given by the equation

$$t = \frac{R_A + R_X}{\sqrt{2}(R_B + R_X)} \tag{3.1}$$

, where R_A is the ionic radius of the A cation, R_B is the ionic radius of the B cation, and R_X is the ionic radius of the halide X anion. When $0.8 < t < 1$, the cubic perovskite structure is obtained. However, when $t < 0.8$ or $t > 1$ a non-perovskite phase with orthorhombic and hexagonal structure is formed respectively [93]. From all the A cations that are included in 3.1, only the FA, MA, and Cs can stabilize the cubic perovskite structure due to their ionic radius, while there is evidence that K, Na, and Rb most likely do not incorporate into the lattice and act as additives, even though they provide benefits for the PSCs [94]

TABLE 3.1: Elements and compounds that make up the Perovskite structure

A Cation	B Cation	X Anion
FA	Pb	I
MA	Sn	Br
K		Cl
Na		
Cs		
Rb		

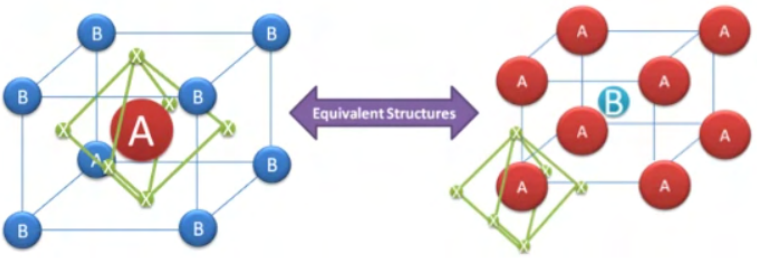

FIGURE 3.1: The two equivalent forms of a Perovskite crystal structure [95]

3.2 Phase Transitions

Perovskite materials can undergo a series of phase transitions either by a change in temperature or pressure. Among them, these are separated into 3 perovskite phases denoted by the greek letters α, β, and γ. There is a fourth, non-perovskite phase transition denoted by the Greek letter δ. This phase is known to be existent in the $FAPbI_3$ and the $CsPbI_3$ perovskite.All the described phase transitions are shown in 3.2(a),3.2(b).It is worth mentioning that all phase transitions are reversible.[40] Lets briefly review each phase:

- α **phase:** The α phase is the basic black perovskite phase and the most stable among all. It has a cubic symmetry and is usually formed for temperatures above $\approx$ 323K.For instance, in the $MAPbI_3$ perovskite the α phase is stable for $T >$ 330K and in the $FAPbI_3$ for $T >$ 300K.

- β **phase:** The β phase is a case of lower symmetry than the α phase. The process of symmetry lowering is called twinning. For mixed perovskites, the transition from the α to the β phase occurs for mixed perovskites in the range $150K < T < 300K$. An exception occurs in the case of $MAPbI_3$ where the transition is observed at $\approx$ 333K. For the $FAPbI_3$ perovskite transition occurs at $T < 130K$ and occurs from the δ phase. The symmetry lowering leads to a tilting of the octahedra formed by the halogens which leads to tetragonal symmetry. [40, 96]

- γ **phase:** Further reduction of the temperature at $\approx$ 100K and below leads to the γ phase, which possesses an orthorhombic symmetry. For the case of the $MAPbI_3$ it is encountered below 160K and for the $FAPbI_3$ perovskite it is non-existent. [40, 96]

- δ **phase:** Specific perovskite crystals such as the $FAPbI_3$ and $CsPbI_3$ can undergo the δ phase, a transition that leads to a non-perovskite structure. The δ phase occurs for $FAPbI_3$ at $130K < T < 300K$ while for $CsPbI_3$ it occurs at $\approx 292K$. [40, 96]

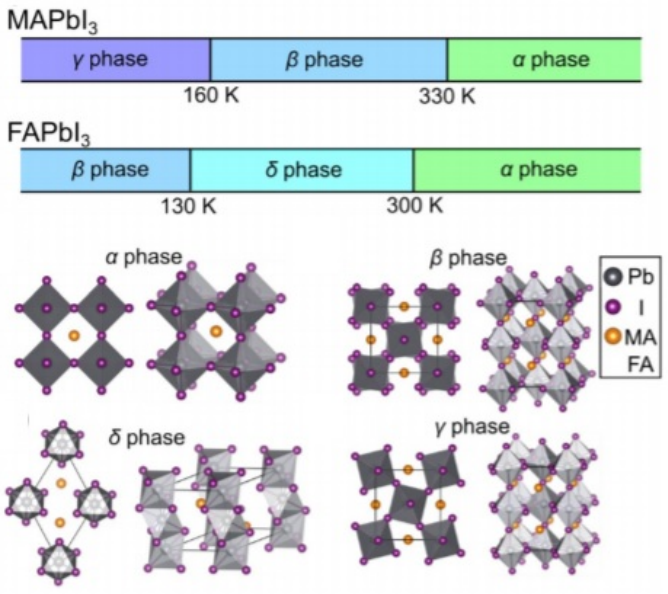

(a)

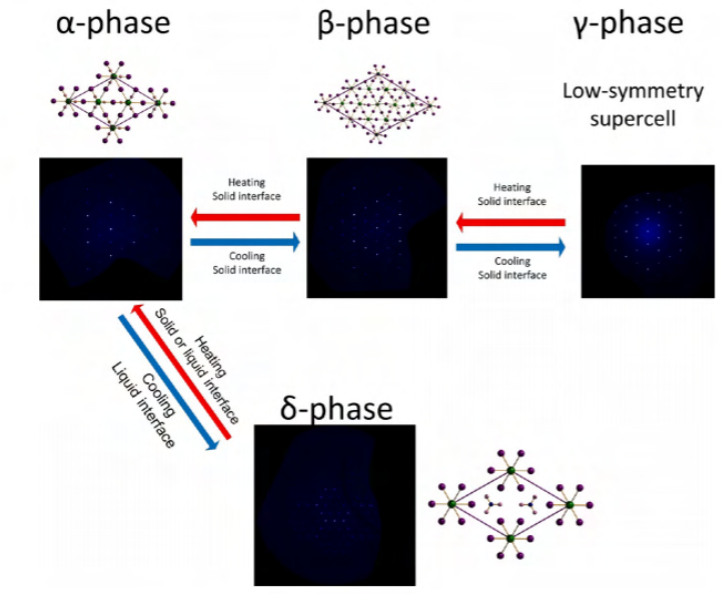

(b)

FIGURE 3.2: a) Phase Transitions on $MAPbI_3$ and $FAPbI_3$ Perovskite [97],b) General Mechanism of phase transitions in Perovskites [40]

3.3 Influence of A,B cations & X anion

- **A Cation:** Density Functional Theory (DFT) has shed more light into the effect of mixing a series of A cations on the optoelectronic properties of perovskites. The 6s orbital of the lead atom (Pb) interacts with the 6p and

5p orbitals of Iodide (I). Then, the bottom of the Valence Band (VB) is formed by the empty 6p orbitals of Pb and possibly by the interaction of the 6p orbital of Pb with the 5p orbital of the iodide atom. This shows that the A cation does not heavily influence the band structure but mostly contributes to sustaining the stability of the structure. This means that a change in the presence of A cations can either reduce or increase the crystal lattice. As it is evident from figure 3.3, doping the perovskite with a series of A cations does not have a significant effect on the bandgap. The addition of more A cation elements can have a series of positive aspects for the devices. These are summarized in figure 3.4,and refer to mixed perovskites that are often used in PSCs

ID	doping	E_g [eV]	λ_{max} [nm]	I_{max} [a.u.] (1E6)
1	-	1.638	777	0.96
2	6% Cs	1.639	771	0.69
3	6% Rb	1.627	790	0.52
4	6% K	1.627	780	1.74
5	6% Na	1.613	788	1.46
6	3% Cs, 3% Rb	1.635	775	0.81
7	3% Cs, 3% K	1.632	762	0.85
8	2% Cs, 2% Rb, 2% K	1.630	774	1.97

FIGURE 3.3: Effect on the perovskite bandgap after doping with various A cations.[37]

role and effects of Cs	role and effects of Rb	Role and effects of K
•gets incorporated into lattice at A-site	•most likely not incorporated into lattice at A-site	•most likely not incorporated into lattice A-site
•helps in formation of cubic perovskite phase (complete removal of yellow phase)	•segregation preferably near to the ETL and at grain boundaries	•shift of XRD peaks/lattice expansion (contrary to what expected if it was incorporated)
•enhanced stability	•enhanced stability	•reduction/elimination of hysteresis
•reduces trap states	•enhancement in charge mobility	•hinders formation of δ-$FAPbI_3$
•resists phase segregation in mixed I/Br perovskites (improves photostability)	•no effect on trap landscape	•grain boundary passivation

FIGURE 3.4: How the addition of K,Cs and Rb cations affects the overall device [37]

- **B Cation:** In the B cation, there is only one alternative to the toxic Pb component, tin (Sn). Tin was first employed as it has a closer ionic radius to Pb. The introduction of tin increases significantly the bandgap at ≈ 1.3 eV, increasing the absorption edge of the perovskite up to 1000nm. Tin perovskites have large electron mobilities that can be as high as ≈ 2000 $cm^2V^{-1}s^{-1}$ and long diffusion lengths. The main two problems with tin

are poor stability and film quality. The stability is limited due to the rapid oxidation of Sn^{2+} to Sn^{4+}. The poor film quality is due to the rapid crystallization in Sn perovskite films. Several methods have been employed such as solvent engineering, using a variety of additives and precursors (e.g N_2H_4 or SnF_2) and different thin film deposition techniques, but as it is clear from figure 3.5 the PCE of Sn devices remains much inferior compared to lead-based Perovskites [37]. The presence of Lead in the perovskite increases the bandgap up to 1.6 eV, while the addition of tin reduces it.

Sn perovskite (with additives)	device structure	J_{SC} (mA/cm^2)	V_{OC} (V)	FF	PCE (%)
$MASnI_3$ (with 20% SnF_2)	regular	3.3	0.23	41	0.3
$MASnI_3$ (with 20% SnF_2)	regular	26.2	0.23	3	2.3
$MASnI_3$ (with 20% SnF_2)	regular	21.4	0.32	46	3.2
$MASnI_3$ (with 20% SnF_2 and N_2H_4)	regular	19.9	0.38	52	3.9
$MASnI_3$ (with 20% SnF_2)	inverse	11.8	0.45	40	2.1
$FASnI_3$ (with 20% SnF_2)	regular	24.5	0.24	36	2.1
$FASnI_3$ (with 10% SnF_2 and pyrazine)	regular	23.7	0.42	63	4.8
$FASnI_3$ (with 20% SnF_2)	regular	23.1	0.38	60	5.3
$FASnI_3$ (with 10% SnF_2)	inverse	22.1	0.47	60	6.2
$CsSnI_3$ (with 10% SnF_2)	regular	22.7	0.24	37	2.0
$CsSnI_3$ (with 20% SnF_2 and N_2H_4)	regular	30.8	0.17	35	1.8
$CsSnI_2Br$ (with 60% SnF_2 and H_3PO_2)	regular	16.7	0.33	53	3.2
$CsSnBr_3$ (2.5% SnF_2)	inverse	2.4	0.4	55	0.6
$CsSnBr_3$ (20% SnF_2)	regular	6.6	0.41	48	1.3
$CsSnBr_3$ (with 20% SnF_2)	regular	9.1	0.4	56	2.1
$CsSnBr_3$ (with 20% SnF_2 and N_2H_4)	regular	14.0	0.37	59	3.0
$MA_{0.9}Cs_{0.1}SnI_3$	inverse	4.5	0.2	36	0.3
$FA_{0.8}Cs_{0.2}SnI_3$	inverse	16.1	0.24	36	1.4
$FA_{0.5}MA_{0.5}SnI_3$ (with SnF_2)	inverse	21.3	0.53	52.4	1.3
$FA_{0.75}MA_{0.25}SnI_3$ (with SnF_2)	inverse	21.2	0.61	62	8.12
$FASnI_3$ (with SnF_2)	regular	22.5	0.48	66	7.14
$(BA)_2(MA)_3Sn_4I_{13}$ (with SnF_2)	regular	24.1	0.229	45.7	2.53
$(PEA)_2(FA)_8Sn_9I_{28}$	inverse	14.4	0.59	69	5.97

FIGURE 3.5: PCE of various Sn based perovskites using different approaches [37]

- **X Anion:**

  Unlike the case of cations, a change in the halide content can have a large impact on the optical and electrical properties of perovskites and even in parameters such as the diffusion length and carrier lifetime. The introduction of Cl leads to no detection of it in the final perovskite film. However, the addition of Cl has a positive, non-direct impact on the perovskite film morphology and crystallinity. Several chloride components such as MACl,$PbCl_2$ and NH_4Cl have been incorporated successfully. This improvement originates by slowing down the crystallization process which results in uniform,pinhole-free films and consequently higher PCE. The situation however is different in the case of I and Br. Their addition in the perovskite has a direct and clear effect on the optoelectronic properties such as the bandgap. The addition

of bromide anions of smaller sizes increases the bandgap of mixed halide perovskites. Mixed perovskites can be composed of stoichiometric ratios of I and Br. A simple case of a mixed perovskite is the $MAPbI_{3-x}Br_x$. The same increase in the bandgap has been observed in FA based perovskites $FAPbI_{3-x}Br_x$. The only difference in this perovskite composition is that after a threshold molar ratio of Bromine, a non-crystalline phase is formed. The effect of adding bromide on the optical absorption and film quality of the $MAPbI_{3-x}Br_x$ perovskite is shown in figure 3.6.

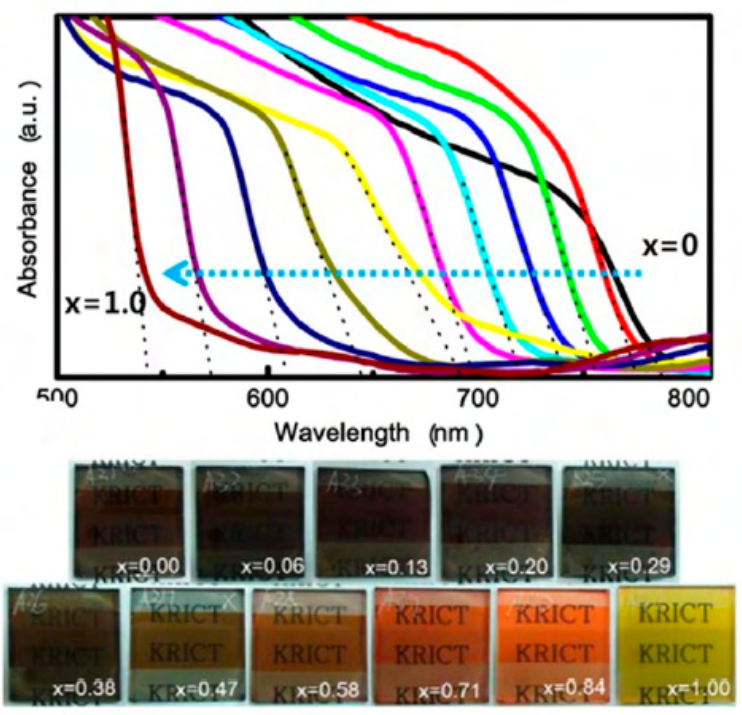

FIGURE 3.6: Effect of bromine addition in the optical absorption and obtained perovskite film. [37, 39]

- **A cation/X anion Mixed Perovskites:** A series of $FA_xMA_{1-x}PbI_{3-x}Br_x$ perovskites have been successfully employed in devices. The addition of both A and X cations and anions can improve the PCE and the stability of PSCs. The addition of Br increases the Open Circuit Voltage (V_{OC}) and the co-existence of FA and MA increases the tolerance factor and stabilizes further the perovskite structure. Several devices have been fabricated with mixed perovskites, yielding PCEs of more than 20%[37] for a FA/MA ratio of 83/17. Even though the MA cation with a smaller size than FA stabilizes the perovskite structure, a small amount of the yellow non-perovskite δ-phase is present in the resultant film of $FA_xMA_{1-x}PbI_{3-x}Br_x$. This issue was

resolved by introducing the Cs cation into the structure. The mechanism for the stability of the structure is due to an intermediate phase formed by Pb^{2+},Cs^{+} and the Dimethyl Sulfoxide (DMSO) solvent, one of the two perovskite solvents along with Dimethyl Formamide (DMF), which suppresses the formation of the yellow δ phase [98].

- **Excess AX or BX_2:** The addition of excess AX or BX_2 has been extensively studied. These components can enhance crystallinity and surface morphology. For instance, excess MAI can reach the grain boundaries and suppress non-radiative recombination. The addition of MACl has also been beneficial for crystallinity and film morphology, even though the added MACl leads to no detection of chloride in the final perovskite film. The addition of AX can be also detrimental. Unreacted MAI can remain on the perovskite surface leading to a drop in current density. Similarly, the addition of BX_2 can be beneficial or detrimental for the device's performance. In most of the cases, excess PbI_2 is used in the perovskite precursor solution.PbI_2 can lead to defect passivation and improve the PCE, as the PbI_2 phase is found within the grain boundaries of the perovskite. However, overestimating the amount of added PbI_2 in the precursor can have detrimental effects on the PCE and can lead to poor stability due to degradation caused by exposure in humidity or light, due to the photodecomposition of PbI_2.

3.4 Semiconductor Properties of Perovskites

3.4.1 Optical properties

Perovskites can be considered as cheap semiconductors compared to the expensive Silicon and all III-V semiconductors. Perovskite compounds exhibit large absorption coefficients in the visible range, on the order of 10^5 cm^{-1}, which is comparable with the established first-generation silicon and GaAs as we can see from figure 3.7. As we previously saw in figure 3.3 the optical properties of the perovskite, and therefore the bandgap can be tuned to 1.1-3 eV by changing each of the 2 cations or the anion. The tunable bandgap makes perovskites potential candidates to be used in tandem devices where two different absorbers, for example, silicon and Perovskite are used. The absorbance spectra of the perovskite and the Silicon are almost complementary as we will see. The optical properties of perovskites are affected by their band structure. The VB of the perovskite consists of mixed np^6

orbitals from the halide and ns^2 orbitals from the metal cation.The Conduction Band (CB)contains empty np^0 orbitals from the metal cation.[99]

Another issue regarding the optical properties of PSCs is the formation of photoexcited states, i.e excitons. Excitons in perovskites have been a controversial issue in the research community. It is widely accepted that the excitons in perovskites are of the Wannier-type excitons with low binding energy ranging from few meV up to almost 100 meV. These values are much lower than the binding energies(100-1000 meV) of Frenkel-type excitons that exist in organic semiconductors due to the small dielectric constants that cannot screen effectively the Coulomb potential. These binding energies in perovskites can generate a large number of free charge carriers due to the quick exciton dissociation at room temperature. This has a large impact on device performance as the charge transfer and collection processes are enhanced due to the quick transport of free carriers at the electrodes due to strong built-in electric fields in the device.[100]

The excitonic state is the case where the photoexcited species (excitons) are dissociated and collected by the electrodes. However, these states have a finite lifetime, then the generated electron and hole pair recombine after their generation by an incident light source on the perovskite. The emission of light or PL from the perovskite film upon excitation is detected near the IR range, with the generally accepted emission peak wavelength at ≈ 770nm. Perovskite materials exhibit strong PL emissions. The PL peak of perovskites can also be detected in a variety of wavelengths ranging from 750-820nm. This variation is caused due to the different film deposition conditions and the presence and types of defects.

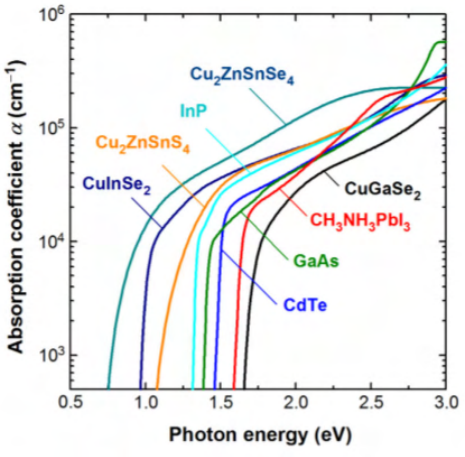

FIGURE 3.7: Absorption coefficients as a function of energy for various absorbers for photovoltaic applications [101]

3.4.2 Charge Transport Properties

Perovskite materials possess balanced, ambipolar charge transport properties.The reason is the similar electron and hole effective masses with respective values of $0.23m_0$ and $0.29m_0$ [102]. A balanced charge transport can significantly affect the PCE of PSCs. However, the perovskite materials can show both p and n-type properties, depending on the interfacial layer.

Another important parameter for an efficient device is the diffusion length. Perovskites exhibit long diffusion lengths on the order of a few μm, which is much larger than the ones of Organic semiconductors. The less the diffusion length the more severe are the recombination effects within the material. The diffusion length depends on the degree of crystallinity, the size of the polycrystalline perovskite grains, and the presence of traps.[100]. The mobility of perovskites is usually tenths or hundreds of $cm^2\ V^{-1}\ s^{-1}$. These values are comparable with the typical inorganic semiconductors. Factors which limit the mobility are mostly morphological, such as the interactions with the lattice (intrinsic factor) or grain boundaries, defects, and crystal impurities (extrinsic). The mobility values usually range due to many factors that induce errors such as lab conditions, thin film preparation, and spin coating parameters, etc. Mobility measurements are also performed in thick single crystals for more precision.[103, 104]

3.4.3 Morphological Properties

The morphological properties are affected by the processing conditions (deposition, environment, annealing of perovskite films, pinholes, traps, etc.). Perovskites are polycrystalline materials, meaning the perovskite grains are surrounded by grain boundaries, which in turn have an impact on the non-radiative recombination, charge transport, and collection. A characteristic of the dependence on processing conditions is the following: Changing the annealing process of the perovskite film can increase the diffusion length by 1 μm! The larger grain size of the perovskite films is associated with higher charge mobility.

3.5 Perovskite film deposition

3.5.1 Film formation mechanism

The perovskite film formation is based on the nucleation process. The term nucleation refers to the formation of another phase particles in a mother phase.

Nucleation can be either homogenous or heterogeneous. Homogeneous nucleation occurs spontaneously,while heterogenous (predominant mechanism compared to homogeneous) nucleation occurs at a specific surface or a foreign particle in the mother phase called nucleation sites. The nucleation process in a perovskite film that is produced occurs as follows: According to figure 3.8, we have 3 stages. In stage I, initially, the perovskite precursor exists in the form of ions and molecules in the solution. During the spin coating and the heat treatment (annealing) of the film, the concentration of the solution increases until it reaches the point of supersaturation. Supersaturation is the difference in the chemical potential of the mother phase and the new phase (perovskite grains). This means that below supersaturation, energy is need for crystal growth. In stage II, as the concentration reaches and goes above C_s the perovskite crystal nuclei begin to form and grow by the continuous supply of solute molecules and ions through diffusion. The concentration of the solution reaches a maximum value and starts to decrease because when the nuclei have reached a supercritical size, then energy is released and the nuclei keep growing, and nucleation no longer occurs. This happens because the consumption of the solutes is faster than their evaporation. In stage III, the growth of the formed nuclei continues until the complete depletion of the precursor solution. The surface dependence lies in the contact angle between the solution and the substrate used.

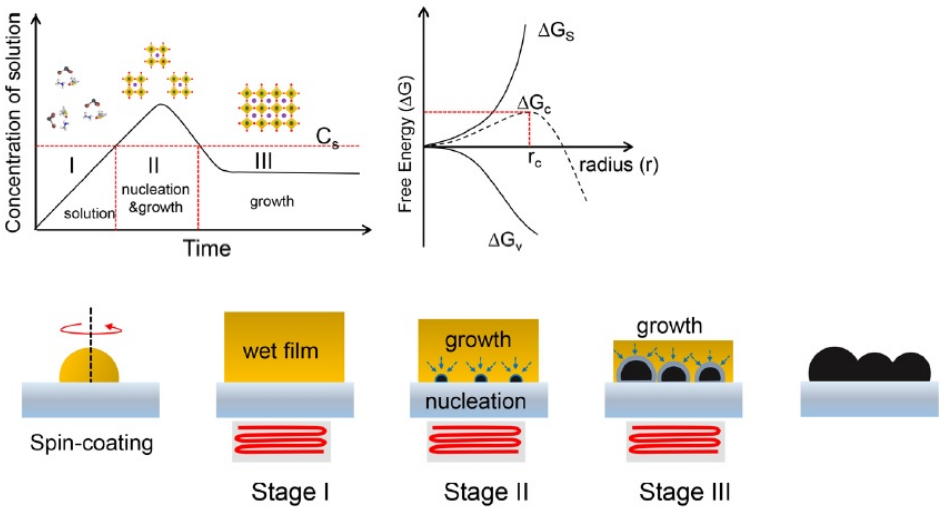

FIGURE 3.8: The nucleation mechanism for the perovskite thin film growth. [39]

3.5.2 One-step vs two-step deposition

A variety of techniques are used for the formation of perovskite thin films. One of the simplest and most employed deposition techniques is spin coating. It is a very simple technique that requires no special equipment for solution-processed materials. A proper amount of solution from the material of interest is deposited in a substrate (usually glass substrates) before the start or during the spinning process. The solvent evaporates due to the centrifugal force and a thin film of a few up to hundreds of nanometers is obtained.

For the case of the perovskite film, the film is obtained from the initial colloidal solution. Typically, the perovskite precursor solution includes all the precursor components, such as PbI_2,$PbBr_2$, FAI, MABr, MAI, MACl, CsI, or even RbI and KI.These precursors added in stoichiometric ratios are dissolved in polar , aprotic solvents such as DMF,DMSO and γ-Butyrolactone (GBL).The use of DMF results in large grains. The drawbacks of DMF are the high boiling point and low vapor pressure which leads to slow nucleation and rapid growth, which prevents the formation of uniform grains. This leads to a rough, uncovered surface with pinholes due to the uncontrolled crystal growth. On the other hand, the use of DMSO leads to the formation of an intermediate phase PbI_2-MAI-DMSO, which retards the crystallization process due to the stronger interaction of Pb^{2+}-DMSO compared to DMF. This leads to the formation of uniform and dense films.Nowadays, a combination of these 2 solvents is employed with a usual ratio being DMF: DMSO 4:1. There are 2 approaches to prepare high-quality-dense black, pinhole, and crack-free perovskite films: These include one-step and two step processes which will be briefly discussed separately. Each process is presented in figure 3.9

- **One step deposition:** In the case of one step deposition, all the precursors used for the desired perovskite composition are dissolved in a DMF: DMSO mixture. The solution is directly cast on a glass substrate. By spin coating, a thin film is obtained through the process described previously, which is thermally annealed in temperatures ranging between 100-150°. Since the early days of perovskites, this approach was found to be problematic due to issues that prevented high PCEs. The use of DMF only led to poor substrate coverage along with the drawbacks that were mentioned. This led to solvent engineering attempts that were focused on solvent removal. The solvent engineering method is the famous anti-solvent method [105], in which a proper amount of a solvent that is polar, miscible with the used polar

aprotic solvents, and does not dissolve any perovskite precursor is applied. This approach removes quickly the solvent during spin coating and assists the uniform nucleation. Many anti-solvents have been employed, even though Chlorobenzene is the most widely used. Other anti-solvents employed include toluene, Hexane, ethyl acetate, diethyl ether, and anisole. This approach is sensitive to environmental lab parameters. Furthermore, in mixed perovskites, the interaction between the perovskite precursor and solvent molecules differs upon the composition of precursors. This affects the solvent evaporation rate, the solubility of precursors in the solution, and optimization must be performed to find the best timing for the correct anti-solvent dropping.[39] The use of anti-solvent improves film morphology and reproducibility and promotes crystal growth because it induces fast supersaturation. [106].

- **Two step deposition:** Sequential deposition or two-step process for perovskite deposition is another option. In this case, first, the Pb-based precursors such as PbI_2 are spin-coated. Then, the deposition of an organic salt such as MAI or exposure in a liquid or vapor is followed. In the two-step deposition, the reaction between Pb and the organic salts can be more controllable. This induces the crystallization process that is achieved through interdiffusion and is enabled by heat treatment (thermal annealing). An issue that might arise from the two-step process is the remnant unreacted PbI_2 due to incomplete MAI or FAI diffusion.

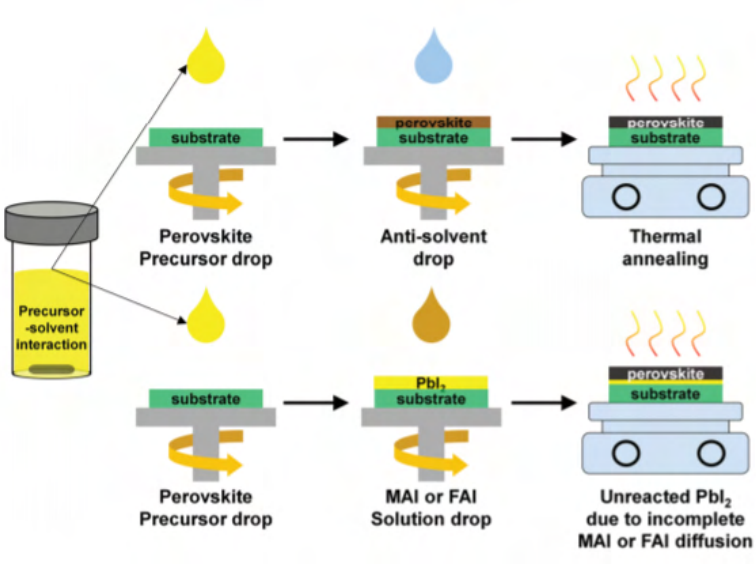

FIGURE 3.9: Graphical illustration of one and two step perovskite film deposition. [106]

3.6 Device Geometries

During the last decade,the PCE of PSCs has dramatically increased,reaching recently 25.2 % [107], which is very close to Si solar cells.The evolution of the performance of PSCs is evident from figure 3.10. These high values along with several other attempts have been achieved by employing two possible geometries: Normal PSCs, which can be divided into two subcategories: i)Planar and ii) Mesoscopic PSCs and Inverted PSCs. Let's have a brief summary of the three structures presented in figure 3.11:

no.	PCE (%)	perovskite composition	device structure (coating procedure)	institute[d] (year)
1	3.8	$MAPbI_3$	liquid junction	Toin U (2009)
2	6.5	$MAPbI_3$	liquid junction	SKKU (2011)
3	9.7	$MAPbI_3$	solid-state mesoscopic TiO_2	SKKU (2012)
4	10.9	$MAPbI_3$	solid-state mesoscopic Al_2O_3	Oxford U (2012)
5	12	$MAPbI_3$	mesoscopic TiO_2	KRICT (2013)
6	14.1[b]	$MAPbI_3$	mesoscopic TiO_2 (two-step)	EPFL (2013)
7	16	$FAPbI_3$	mesoscopic TiO_2	SKKU (2014)
8	17	$MAPbI_3$	mesoscopic TiO_2 (two-step)	SKKU (2014)
9	17.9[b]	$(FAPbI_3)_{0.85}(MAPbBr_3)_{0.15}$	mesoscopic TiO_2	KRICT (2014)
10	19.3	$MAPbI_3$	normal planar, Y:TiO_2 ETM	UCLA (2014)
11	20.1[b]	$(FAPbI_3)_{0.95}(MAPbBr_3)_{0.05}$	mesoscopic TiO_2	KRICT (2014)
12	20.4	$MAPbI_3$	mesoscopic TiO_2	SKKU (2015)
13	22.1[b]	$(FAPbI_3)_{0.95}(MAPbBr_3)_{0.05}$	mesoscopic TiO_2	KRICT (2016)
14	22.7[b]	$(FAPbI_3)_{0.95}(MAPbBr_3)_{0.05}$	mesoscopic TiO_2, fluorene-terminated HTM	KRICT (2017)
15	23.7[b]	$FA_{0.92}MA_{0.08}PbI_3$	normal planar, SnO_2 ETM	ISCAS (2018)
16	24.2[b]			KRICT/UNIST (2019)
17	25.2[b]			KRICT/MIT (2019)

[b]Certified value. [c]"Solar Cell Efficiency Tables" published in *Progress in Photovoltaics: Research and Applications*. [d]Institutes: SKKU = Sungkyunkwan University; KRICT = Korea Research Institute of Science and Technology; ISCAS = Institute of Semiconductors, Chinese Academy of Sciences.

FIGURE 3.10: The rapid Efficiency evolution of PSCs in the last decade. [39]

- **Mesoscopic (n-i-p) Structure:** Mesoscopic PSCs was the first device geometry that was employed.In the early days, it was assumed that the perovskite device works in the same manner as the dye in DSSCs, where the perovskite is coated in a m-TiO_2 layer in a liquid electrolyte based electrochemical cell. However, further experiments on devices with an insulating Al_2O_3 mesoporous layer or without any mesoporous layer (Compact Titanium Dioxide (c-TiO_2) was used) showed that both electrons and holes can eventually transport in the perovskite film without the need to use any scaffold layer. This was the milestone of differentiating the working mechanism of PSCs from DSSCs and correlating it with the operation of conventional PN junction solar cells. The mesoscopic (n-i-p) structure consists of a front electrode which is usually FTO,a TiO_2 layer (which can be either compact or mesoporous), the perovskite absorber,a HTL which is typically 2,2',7,7'-Tetrakis[N,N-di(4-methoxyphenyl)amino]-9,9'-spirobifluorene (Spiro-OMeTAD) (Spiro is a small molecule HTL), and a metal back contact, usually Au(Indium Tin

Oxide (ITO)/c-TiO_2/m-TiO_2/Perovskite/Spiro-OMeTAD/Au). Many of the record PCEs over the years have been achieved by employing the Mesoscopic architecture. The main drawback of the mesoporous structure is the high-temperature sintering ($> 400°$) [39] that is required to activate the mesoporous scaffold layer for the perovskite to be infiltrated.The c-TiO_2 is deposited through spray pyrolysis.Mesoscopic PSCs achieve PCEs of more than 20%.

- **Planar (n-i-p) Structure:**. This geometry is the same with Mesoscopic without the Mesoporous scaffold. It usually consists of ITO/SnO_2/Perovskite/Spiro-OMeTAD/Au. As an electron transport layer TiO_2 and ZnO are also used. Alternatively, as HTL, P3HT and copper-based inorganic materials such as Copper(I) Iodide (CuI) or Copper(I) Thiocyanate (CuSCN) are used [108]. Most of the efficiency records over the years have been achieved by the use of Planar PSCs. However, the stability of n-i-p devices is limited. Spiro-OMeTAD requires doping with the lithium salt, Lithium bis(trifluoromethanesulfonyl)imide (Li-TFSI) in order to increase the conductivity of Spiro-OMeTAD [109].The doping is achieved through oxidation by exposing the devices in ambient environment under controlled humidity. This results to a HTL that is highly hygroscopic, which accelerates device degradation.

- **Inverted (p-i-n) Structure:** Inverted PSCs is another device geometry that is used,structured as ITO/HTL/Perovskite/ETL/Ag or Al. Initially, most inverted devices used PEDOT:PSS as the HTL, which limited the efficiency. Nowdays, the most efficient PSCs are fabricated using PTAA as the HTL. Another common HTL used is Nickel Oxide (NiO_x). Common ETL include $PC_{60}BM$or evaporated C_{60} and Zinc Oxide (ZnO). An interlayer between the ETL and the metal is either spin coated or evaporated. This consists of a few nm of the insulating material 2,9-Dimethyl-4,7-diphenyl-1,10-phenanthroline (BCP) to improve the contact between Ag and $PC_{60}BM$ and device stability.Other alternatives to BCP are Poly [(9,9-bis(3'-(N,N-dimethylamino)propyl)-2,7-fluorene)-alt-2,7-(9,9–dioctylfluorene)] (PFN) and Lithium Fluoride (LiF) [110]. The back metal contact is either Silver (Ag),Aluminium (Al) or Copper (Cu).Despite that most records have been achieved using the planar or mesoscopic geometries, inverted devices have caught up, achieving PCEs close to 23% [111–114].

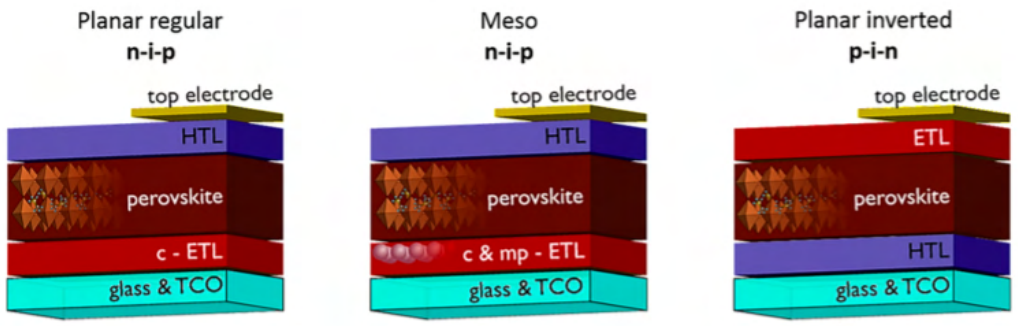

FIGURE 3.11: Schematic illustration of device geometries used in PSCs.[115]

3.7 Hysteresis

At the very early stages of fabricating PSCs, rather unusual behavior was observed initially by Snaith et al. in 2014 [116]: The PCE of perovskite solar cells while scanning in both directions, forward and reverse is NOT the same. The presence of hysteresis is mainly due to the perovskite absorber, but the severity depends on the interfacial transport layers used. Even though it is still an active area of research, there are three different scenarios for the origin of the hysteresis behavior in PSCs [117]:

- Bulk or surface defects that act as carrier traps
- Ferroelectric behavior of perovskites due to polarization effects
- Presence of excess ions due to interstitial defects (which are either Iodide or organic cations)

The hysteresis effect was confirmed by comparing the photocurrent response under-voltage sweeps for the hysteresis-free Silicon solar cells and PSCs. While no dependence on time was found for the photocurrent in the case of Si, the perovskite device's photocurrent response was time-dependent. It increased exponentially and remained constant in the case of Forward scan and decreased exponentially and remained constant in Reverse scan. The exponential dependence of the photocurrent response is due to the presence of capacitive current. This is a strong indicator that PSCs can act as capacitors. This brings the question of whether the capacitive effects originate from the bulk or the interfaces? To answer this question, the effect was studied on both normal and inverted devices, which correspond to reversed polarity, leaving the bulk of the perovskite unchanged for both cases. It was found

that normal devices experienced more severe hysteresis compared to Inverted PSCs. These two situations described previously are shown in figure 3.12(a),3.12(b).

The next question that must be answered is what is the origin of the capacitive current? The answer is the 3 bullets mentioned previously. For the case of defects, in the perovskite film, there is the mechanism of charge trapping/de-trapping. The present traps are whether shallow, near the conduction band or deep traps which are located within the bandgap and contribute to non-radiative recombination. The latter contributes to hysteresis because charge transport is affected by charge trapping detrapping, and these sites are located mostly at the interfaces or surface and grain boundaries. Furthermore, the presence of Schottky defects in the $MAPbI_3$ perovskite seems to facilitate ion transport. Real-time photoluminescence measurements under the application of an electric field confirmed the migration of iodine anions. Ferroelectricity has not yet be confirmed as a possible mechanism as there are reports that confirm and argue about its existence. The most probable mechanism is the presence of ion migration with interfacial trap-assisted recombination.

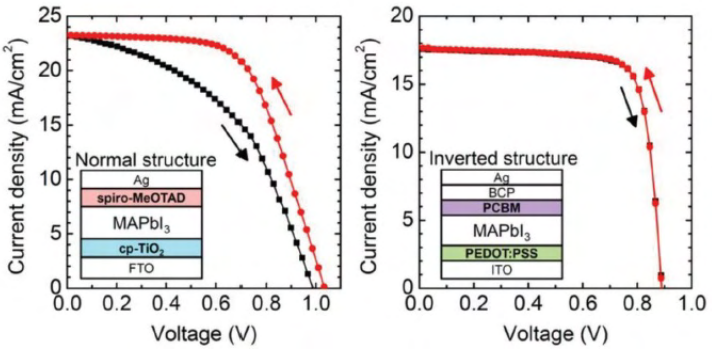

(a)

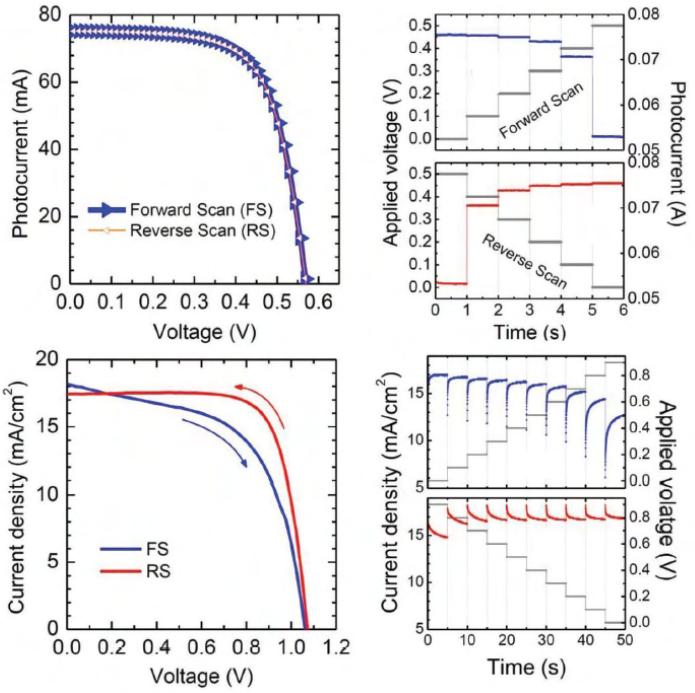

(b)

FIGURE 3.12: a) A comparison of IV curve hysteresis in Normal and Inverted PSCs and b) Observation of photocurrent transients in PSCs after voltage sweeps.[118]

3.8 Strategies to increase efficiency

After the initial PCE improvements and continuous improvements in device processing and perovskite film deposition, along with establishing measuring protocols for the devices by taking into account effects such as hysteresis, several other strategies have been adopted to further increase the PCE of PSCs. The most common are the following:

- **Interface Engineering:** Since PSCs are typically stacks of different layers such as electron and transport layers where 4 interfaces are formed,as the architecture is for example electrode/HTL/Perovskite/ETL/electrode. It is crucial to create good interfaces as these affect device properties such as recombination, charge transport, and charge extraction. Interfaces can be distinguished into electrode/transport layer or perovskite/transport layer interfaces. For the case of electrode/transport layer, band alignment is often an important parameter. The work function of metals such as Al is low, at 4.1eV. These contacts are preferred for collecting electrons. To collect holes, metals with deeper work functions such as Au (5.3 eV) are preferred to match the VB of the perovskite. Zhou and Yang et al. have treated the ITO with polyethylenimine (PEI),resulting to increased conductivity,decreased series resistance and Fill Factor (FF) [119]. Treatment with the same material in inverted PSCs at the surface of the $PC_{60}BM$ ETL, reduced the work function of the silver electrode and increased the FF.Another example is the BCP interlayer (< 5nm) between $PC_{60}BM$ and Ag, which enhances the FF. A possible mechanism suggested by Shibayama et al. is that a thin BCP layer improves electron collection by changing the Shottky contact at the PCBM/Ag interface into ohmic.[120] Most interface engineering attempts are focused on the perovskite/transport layer interface. Improving these interfaces can significantly improve the PCE. Park et al. have treated the NiO_x HTL with PEDOT:PSS .The PCE improved to 15.1 % and the FF reached 72% [121]. Another case of interface engineering is for the case of TiO_2 which has limited electron transfer abilities. A triblock fullerene derivative (PCB-2CN-2C8) was used which improved charge extraction, the V_{OC} and the FF,along with reduced hysteresis [122].The possible strategies for efficient interface engineering are presented in figure 3.13

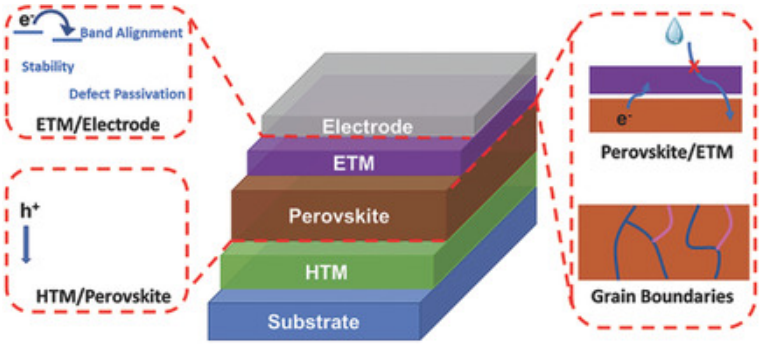

FIGURE 3.13: Schematic illustration of various interface engineering prospects in PSCs.[123]

- **Defect/Grain Boundary Passivation:** Polycrystalline perovskite films in PSCs have a significant number of defects.These defects have a variety of different origins including vacancies, interstitials, Grain Boundaries (GBs), interfaces, impurities and charge segregation/clustering. The density of these defects can largely affect the PCE and mainly the V_{OC} and the FF, because all these types of defects can act as non-radiative recombination centers. Reducing the defect density can dramatically improve the PCE. The passivation can occur in the Bulk of the perovskite films. In the bulk, defects such as cation/anion vacancies, interstitials, or exchanged ions are usually found. Son et al. investigated the effect of alkali metal ions on the hysteresis of PSCs. He concluded that the severity of I-V hysteresis depends on the size of the alkali metals[124]. Min et al. incorporated the divalent cation of methylene diammonium ($H_3N^+ - CH_2 - NH_3^+$-MDA). The $MDACl_2$ molecules were introduced at the $\alpha - FAPbI_3$ perovskite. Doping percentage up to 5% stabilized the α phase of the perovskite due to stronger ionic interactions of the divalent molecules, leading to a PCE of 23.7% and good thermal stability after exposure at 150° for over 20h. Furthermore, the introduction of Cl^- interstitial anions in the lattice increased the carrier lifetime [125]. Another route is the passivation of GBs or Surface defects. Specifically, Alkylammonium halides with long alkyl chains such as ethyl ammonium (EA^+) or octyl ammonium (OA^+) have been employed. These materials can either form two-dimensional perovskite layers or directly act as passivation agents, as in the case of octyl ammonium [126]. The Phenethylammonium Iodide (PEAI) alkylammonium halide has been recently employed. Jiang et al. spin-coated a PEAI passivation layer into the perovskite, which led to the high PCE of 23.2% in planar n-i-p PSCs with an SnO_2 ETL. The optimized passivation effect was found to be without heating (annealing), as this led to the formation of the 2D perovskite PEA_2PbI_4. The passivation mechanism involved the synergistic effect of the π-conjugated structure of Benzene rings that promote charge transport, and the formation of hydrogen bonds between the amine groups with iodide ions, with the iodide ions filling the iodine vacancies.The passivation mechanism for this case is shown in figure 3.14

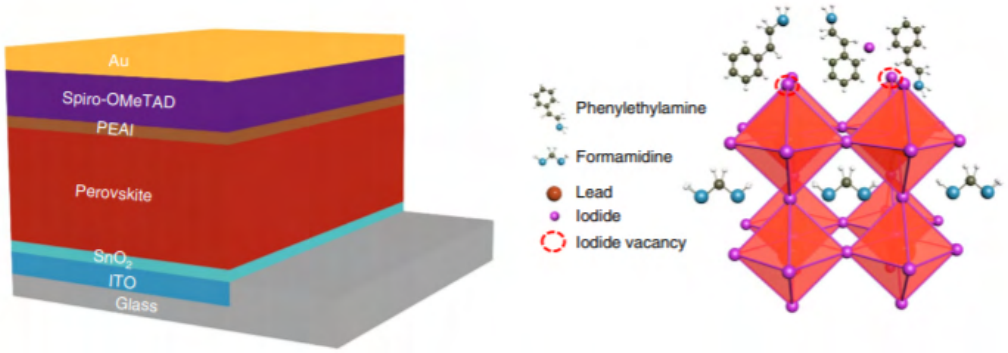

FIGURE 3.14: Device geometry and proposed mechanism of defect passivation in the bulk of the perovskite with PEAI molecules. [127]

- **Tandem Geometry:** The main target of Tandem devices is to overcome the Shockley–Queisser limit, which takes into account factors such as spectral losses and band-to-band recombination. This sets an upper theoretical limit of 33.7% PCE for single pn junctions. Tandem devices can overcome this limit, by stacking 2 device configurations together with 2 absorbers. The first light-harvesting material (top cell) absorbs the high-energy photons, while the second material (bottom cell) absorbs the low-energy photons that have been transmitted through the top cell (figure 3.15(a)). Tandem devices with two subcells are called Monolithic two-terminal. The two subcells are connected through a tunnel junction or a recombination layer, where the overall current density of the tandem device is limited to the lowest current of each of the two subcells. [39] A combination of two absorbers can be Si and Perovskite, with bandgaps of 1.12 and $\approx$ 1.6 eV respectively, or a Perovskite-Perovskite absorber with a high bandgap Pb based perovskite and a tin-based low bandgap absorber [128].This leads to complementary absorption spectra (figure 3.15(b)).Al. Ashouri et al. fabricated tandem Si/Perovskite devices by employing the triple cation perovskite $Cs_{0.05}(FA_{0.77}MA_{0.23})_{0.95}(I_{0.77}Br_{0.23})_3$ in a p-i-n geometry (figure 3.15(a)).This attempt led to a PCE of $>$ 29 % [128]. In a similar manner, Isikgor et.al have fabricated monolithic Si/Inverted PSCs devices and enhanced the PCE from 25.4% to 27.4% by using Phenformin Hydrochloride (PhenHCl) to passivate the perovskite defects [129]

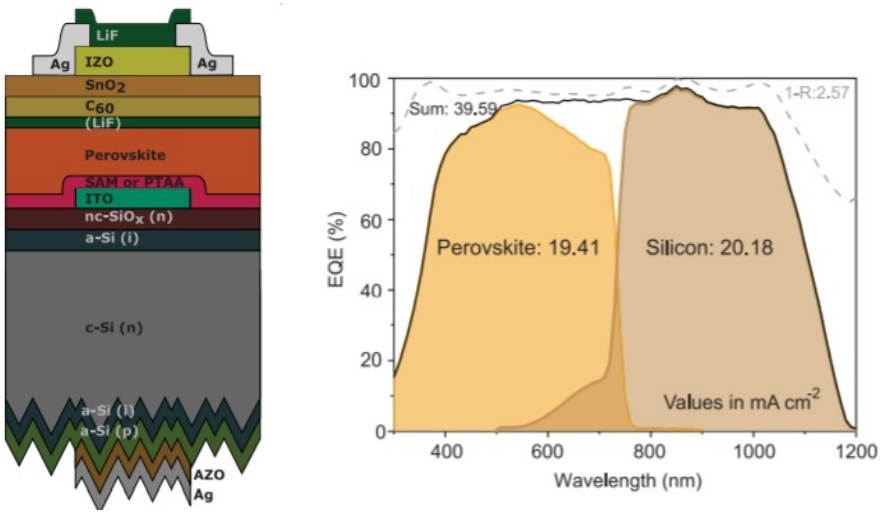

(a) (b)

FIGURE 3.15: a) Device geometry of a Silicon/Inverted Perovskite solar cell monolithic junction and b) Complementary spectra of Silicon and Perovskite absorbers. [130]

3.9 Device stability

In chapter 1 we have seen that the operational lifetime of PSCs is much less than the lifetime of Si cells. The factors that limit the stability of PSCs can be divided into 2 major categories: The first is the structural/intrinsic factors limiting the stability, and the second category is related to External/Environmental stability issues. Each one will be analyzed separately.

3.9.1 Structural/Intrinsic factors:

In section 3.2 we studied phase transitions in perovskites. The Goldschmidt tolerance factor can give a prediction of whether a combination of anions and cations will form a stable perovskite α phase. For $0.8 < \tau < 1$ we have the ideal cubic structure or a structure with tilted octahedra. The first case is for $0.9 < \tau < 1$ and the second for $0.8 < \tau < 1$. When $\tau < 0.8$ $\tau > 1$ a non-perovskite phase is formed. Hence, when τ values are close in the middle between 0.8 and 1, a stable α phase is formed [131] (figure 3.16). Moving away from 0.9 leads to the formation of non-perovskite phases, as in the cases of $FAPBI_3$ and $CsPbI_3$, where τ is close to 1 and 0.8 respectively. On the opposite, $MAPbI_3$ is close to 0.9 and therefore forms the black α phase. This explains the stabilization of the cubic α phase in $FAPBI_3$ when MA or Cs or both are introduced. However, tolerance factors

are more difficult to calculate in mixed perovskites and are estimated by using Vegard's law. That being said, the situation becomes trickier for mixed perovskites, as secondary non-perovskite phases can be formed above a certain concentration. This means that the tolerance factor rule can no longer predict the structural stability of mixed perovskites and is suitable only for choosing the proper cations. The difference in ionic radii in the added alkali metals and the FA,MA cations can stabilize the structure as long as no secondary phases exist. This means that phase purity is another important parameter. Another factor is the symmetry of each structure. In practice, $MAPbI_3$ is less stable than a mixed three cation perovskite with FA, MA, Cs. Experimentally, it has been found that $MAPbI_3$ has a tetragonal symmetry while triple mixed perovskite has a cubic symmetry.

Another factor that contributes to intrinsic stability is the ion migration, which also contributes to the Hysteresis phenomena. Ion migration can occur whether the device is normally operating or by applying a bias in dark conditions. Calculations on ion migration activation energies have revealed that iodide is the most easily migrating ion [132, 133]. Furthermore, in polycrystalline systems such as perovskites, it is assumed that the grains might contribute to ion migration. This however has been proven wrong, since ions can also migrate in high quality $MAPbI_3$ and $MAPbBr_3$ single crystals [134, 135]. Additional to atomic/ionic factors affecting the structural stability, the polycrystalline nature of perovskites can also affect structural stability. It has been found by Zhao et al. that the thermal strain produced during thermal annealing induces degradation of the perovskite. The strain is due to the difference in thermal expansion of the Glass/ITO substrate and the perovskite film. Different levels of strain led to different degradation rates [136].Rolston et al. concluded the same by studying perovskite films on Polyethylene Terephthalate (PET) [137]. Strelcov et al. observed a spontaneous phase transition from cubic to tetragonal under applied stress in $MAPbI_3$ in perovskites.Furthermore, crystal orientation is important as some orientations are more prone to moisture, which leads to crystal planes that degrade faster than the others.[138, 139]

3.9.2 External/Environmental Factors

External factors like moisture, oxygen, heat, light exposure, externally applied voltage affects the stability of PSCs, even if we assume that every issue regarding the intrinsic factors is resolved. Water molecules can easily attach to the perovskite through hydrogen bonding and form hydrated compounds which can cause local

changes in the structure of the perovskite. These changes can be reversible up to a point, while further water penetration makes these changes irreversible. A proper encapsulation (sealing) of the devices is required to prevent the degradation caused by humidity. This might increase the overall cost but will offer good protection of the perovskite device. Moisture tolerance can be improved by adopting various strategies including the introduction of hydrophobic HTLs as a replacement of Spiro-OMeTAD, with interlayers between the perovskite and the HTL or by passivating the defects of the perovskite with small molecules or with a 2D perovskite capping layer which contains hydrophobic organic groups [44, 140–142]. The introduction of large organic cations that are more hydrophobic than FA and MA can improve moisture resistance.

Moisture protection is one of the issues regarding perovskite stability. However, the perovskite layer is also affected by vacuum, O_2 or N_2 environment, hence these factors affect the optical and electronic properties of the perovskite and their effect on PSCs can be more concerning than humidity itself. It has been found that the PL intensity of single-crystal $MAPbBr_3$ is two orders of magnitude higher in the air than in vacuum [143]. Another study has shown that the adsorption of O_2 on the $MAPbI_3$ can passivate the trap states which results in enhanced luminescence [144]. A more concerning case is the simultaneous effect of light and oxygen exposure. Oxygen exposure can even occur in a N_2 atmosphere glovebox. Exposure to both oxygen and light leads to the formation of superoxide by electron transfer from the photoexcited perovskite to the surface of the molecular oxygen. This decomposes the perovskite by deprotonating the MA cation. Developing perovskite compositions that are more oxygen-tolerant is a potential solution to this issue [37]. Electronic processes like ion migration, defect generation, etc. also affect the stability of PSCs and are affected by light or light bias. An example of this issue is the photocatalytic degradation by TiO_2 [145]. Phase segregation is another issue that occurs in mixed perovskites with iodide and bromide which leads to the formation of low bandgap trap states [146]. Increasing the Cs or FA content can improve crystallinity and morphology, as it is believed that defects such as halogen vacancies promote this phase separation.

The stability of PSCs depends not only on the perovskite layer but on the selection of charge selective contacts as well [147]. Spiro-OMeTAD is the most efficient HTL in n-i-p devices, but suffers from stability issues.As we saw previously, dopants are required to enhance the conductivity of Spiro-OMeTAD. The Li-TFSI dopant is highly hygroscopic, which accelerates perovskite degradation. Another

issue is the diffusion of Li into the perovskite. Other degradation mechanisms are crystallization, photooxidation, reaction of iodide with oxidized spiro, and chemical reactions between the additives 4-tert-Butylpyridine (tBP) and Li-TFSI that lead to the formation of voids at elevated temperatures [37].Aggregates have been observed for the case of fullerenes in p-i-n devices with a decrease in PCE. These are formed due to the hydrophobic nature of the fullerene and the hydrophilic nature of the perovskite. Metal oxides on the other hand are more robust than organic materials, as in the case of MoO_x. Another issue is material photostability. As an example, fullerenes provide better shielding to UV irradiation than the unstable TiO_2 ETL. SnO_2 that is widely used in n-i-p devices has a wide bandgap of 3.6 eV, making it photostable. Metal oxides can generally perform better in elevated temperatures, with the only exception of ZnO, causing deprotonation of the perovskite resulting in degradation. Organic molecules can also enhance the oxygen/moisture stability as in the case of the combination of $PC_{60}BM$ with Rhodamine. On the other hand, metal oxides such as SnO_2 are not affected by moisture or heat but severely affect the perovskite growth and defect density when they are placed as bottom substrates in PSCs. PTAA which is the most efficient HTL in p-i-n devices shows better stability than Spiro-OMeTAD in n-i-p devices but shows poor thermal stability.Copper-based materials with high mobility and conductivity also possess robust chemical stability. Another polymer, PEDOT:PSS shows poor stability due to its acidic nature (pH=1.5) that corrodes the ITO and its hydrophilic nature that accelerates device degradation [147]. Last but not least, the electrodes can affect the device's stability. A common example is the formation of silver iodide or the diffusion of Au in the Spiro-OMeTAD layer [148]. An example of the effect of charge selective contacts is shown in figure 3.17(a), where perovskite films with different HTLs are exposed under heat. The perovskite film with PTAA degrades with the fastest rate among all materials tested, demonstrating its poor thermal stability. The possible strategies that can be adopted to improve the operational stability of PSCs are presented in figure 3.17(b).

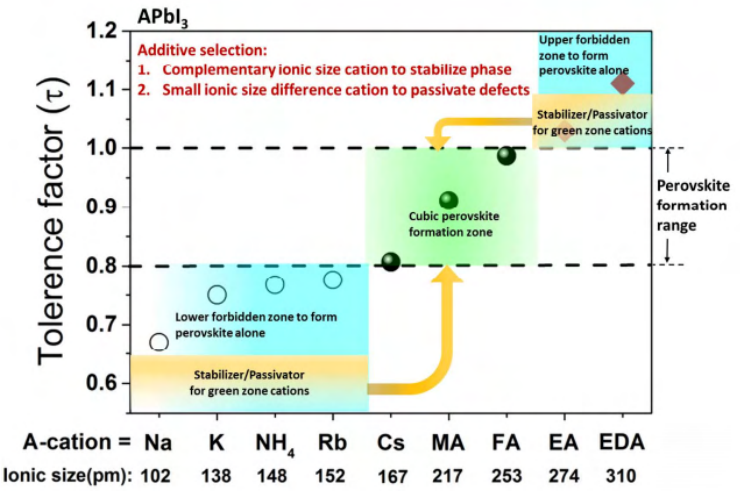

FIGURE 3.16: Tolerance factor for a variety of cations with the illustrated perovskite formation green zone and the formation of non-perovskite phases.[149]

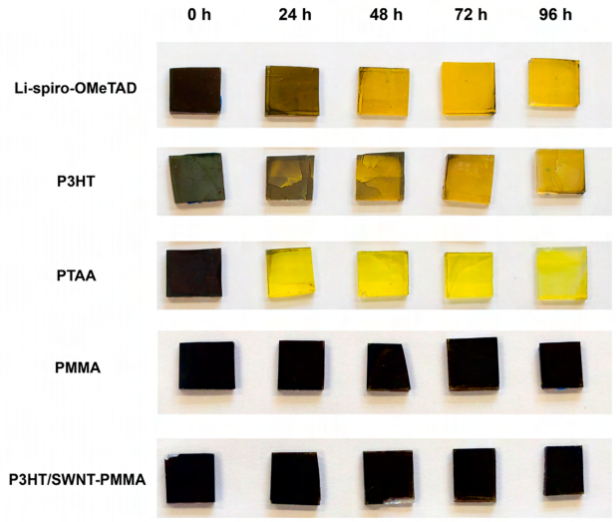

(a)

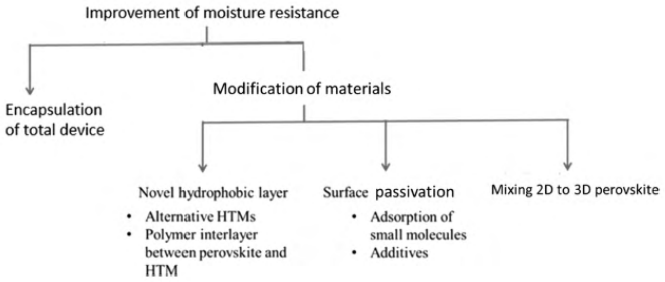

(b)

FIGURE 3.17: a)Effect of thermal stress in perovskite films with different spin coated HTLs.[150],b)Strategies to improve the operational stability of PSCs. [37],

3.10 Moving to large scale

The high PCEs achieved in small area lab cells is very promising, though it has to be translated into high PCE in large area cells/modules. A series of factors contribute to the difference in the PCE between small area and large-area devices. These include the increase in Sheet Resistance, the homogeneity of the film in a large area, and modifications on the precursor solution, the deposition, and the formation of the perovskite film to obtain robust uniform films with good reproducibility and similar PCE values with small area cells. Device scaling up can be based on the current state of the art for small area device geometries or establishing procedures that lead to different device geometries. Scalable deposition routes must be found for the deposition of charge transport layers. A variety of deposition techniques are used for thin film deposition including blade coating, slot-die coating, inkjet printing, screen printing, spray coating, vapor phase deposition and electrodeposition have been applied, as shown in figure 3.18(a).PCEs ranging from 10-14 % have been achieved in large-area devices in a series of attempts illustrated in figure 3.18(b). These values are encouraging but still lack behind efficiencies of small area devices. Un-optimized design for large are devices/modules can severely limit the output power. The difference in film quality-morphology between the spin coating and scale-up methods like slot-die coating can result in the observed difference in PCE between lab cells and large-area devices. Further optimization of the ink/solution and the annealing drying conditions can reduce this difference. For instance, the anti-solvent dripping method is not practical to use in large-scale devices. Instead, methods such as anti-solvent spraying or bath can be employed. Two-step depositions can also be employed but it is very likely modifications will be needed. More advanced methods to avoid long annealing periods of 1h have been adopted. These include rapid annealing methods like IR-sintering, intense -pulse sintering, or photonic flash annealing. A good understanding of the perovskite precursor solution chemistry will eventually improve the large area film formation and reproducibility. Solution aging is a phenomenon that has been systematically observed in PSCs and should be also taken into account for large-area devices. The processing conditions must be carefully studied, to reduce the impact of device processing in ambient conditions. Lastly, cost considerations lead to avoiding expensive materials like Spiro-OMeTAD. HTM-free devices with carbon electrodes are suitable for large area devices as they can reduce fabrication costs significantly. Carbon-based devices are another growing branch to move to large-area devices.

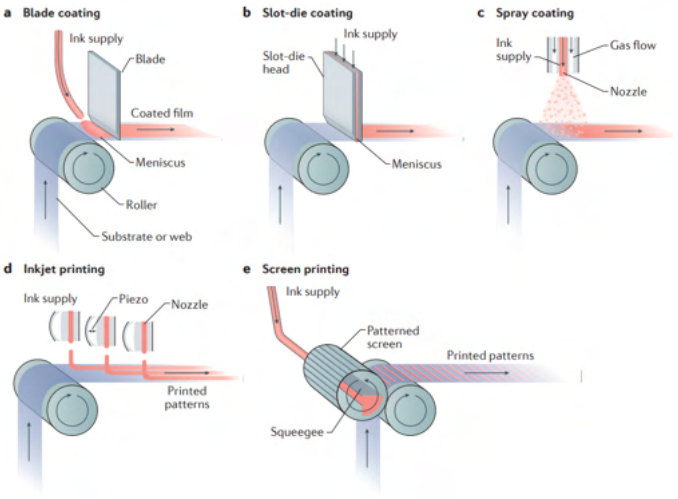

(a)

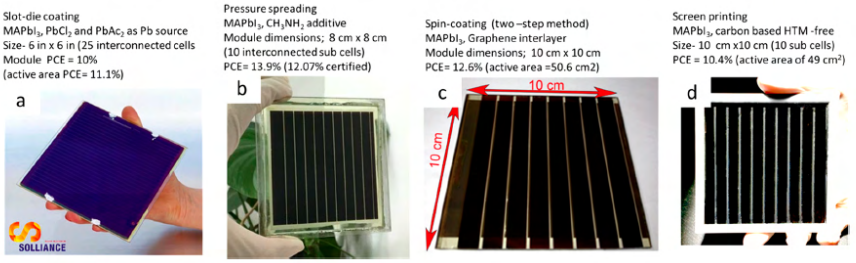

(b)

FIGURE 3.18: a) Film Deposition techniques to scale up the production of PSCs, b)A series of fabrication attempts of large area devices and modules [37]

Chapter 4

Experimental Techniques

4.1 Contact Angle Measurement

The contact angle is an indicator of how well or bad a drop of liquid can spread over a surface, as it is shown in figure 4.1(a). Knowledge of a material's wettability in experimental procedures like thin film deposition is important. The wettability depends solely on the material itself. Surface tension in liquids can explain their wetting or non-wetting behavior. The surface tension is determined by studying the interactions between the molecules of the liquid. Molecules located in the bulk of the liquid experience forces from all adjacent molecules, leading to a net force of zero. On the opposite, liquid molecules at the surface do not have the same amount of neighbors as molecules in the bulk which leads to an inward, non-zero net force as illustrated in figure 4.1(b). The wetting of a liquid and hence the contact angle are determined from the interplay between cohesion and adhesion. Cohesion refers to the attraction forces between molecules of the same type while the forces acting between molecules of different types are named adhesive forces. When cohesive forces dominate, the liquid has non-wetting properties. If adhesive forces are dominating, the liquid has good wetting properties.

The symbol of surface tension is usually the greek letter γ and is measured in Newtons per meter $\left(\frac{N}{m}\right)$. The contact angle is measured through a liquid, where a liquid-vapor phase (the vapor phase is air in most cases) meets a solid interface. As a consequence, three interfaces are formed: the solid-vapor, the solid-liquid, and the liquid-vapor phases. The surface tensions of each interface are indicated by the symbols γ_{SV},γ_{SL}, and γ_{LV}, respectively. The forces exerted by the surface's tensions from each surface are shown in figure 4.1(c) . All forces are pulling away from the equilibrium point, hence under equilibrium, all forces in the horizontal

axis are equal.According to the force diagram, the resulting formula for equilibrium condition is the following:

$$\gamma_{SV} = \gamma_{SL} + \gamma_{LV} \cdot cos\theta \tag{4.1}$$

where θ is the contact angle. If we solve equation 4.1 for cosθ we get the expression

$$cos\theta = \frac{\gamma_{SV} - \gamma_{SL}}{\gamma_{LV}} \tag{4.2}$$

From this formula we have two different scenarios:

- $\gamma_{SV} < \gamma_{SL}$: In this case, cos$\theta$ <0 and therefore θ <90°,making the liquid Wetting.This occurs in a high surface energy solid (eg. a metal) or a liquid with a low surface tension.

- $\gamma_{SV} > \gamma_{SL}$: Here, cos$\theta$ > 0,hence θ >90° and the liquid is non-wetting.This occurs either in low surface energy solids or in high surface tension liquids like Water.

(a)

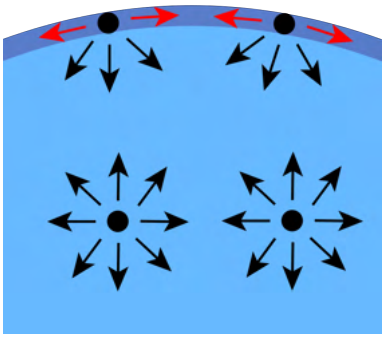

(b)

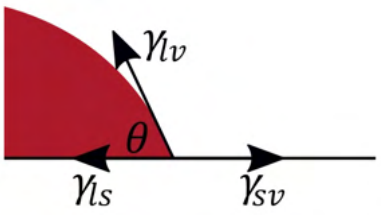

(c)

FIGURE 4.1: a)Wetting and non-wetting behavior of a liquid drop b)Interactions between molecules in the bulk and at the surface of a liquid,c)Diagram of all forces exerted by each interface. [151],[152]

The Contact angle measurement consists of two steps: Recording an image and analyzing it through software. The equipment needed is pretty simple. The

components are a light source, a camera, and a tilting stage. The stage which is under illumination is aligned for droplets to not move, a droplet of the liquid is deposited in the stage and then images are captured using a camera. The image is then analyzed by using code or software which yields the value of the contact angle. These steps are presented in figure 4.2(a). The measurement should be performed with caution to avoid unnecessary effects such as low clarity, low resolution and magnification of the droplet, low contrast, and poor illumination. Another important aspect of the measurement is to contain the whole droplet under the camera's depth of field (figure 4.2(b)).

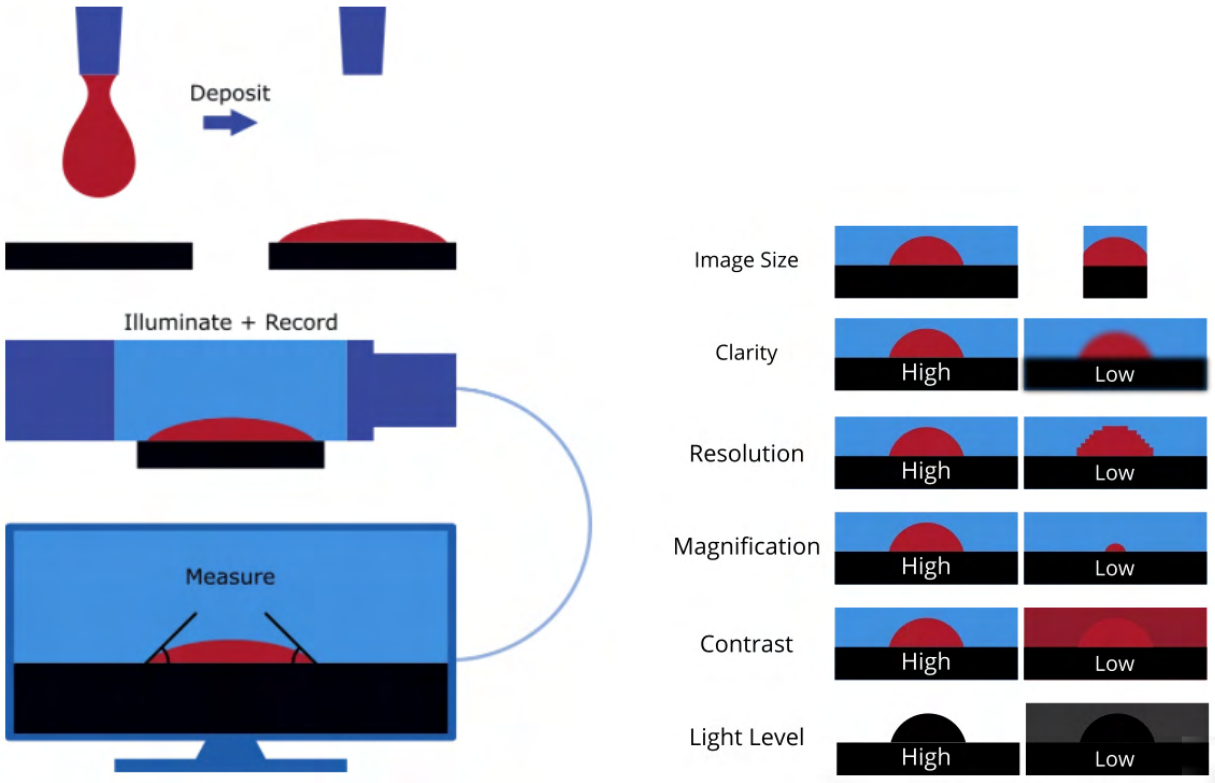

(a) (b)

FIGURE 4.2: a)Contact Angle measurement setup,b)Factors contributing to poor image quality. [151]

4.2 Atomic Force Microscopy (AFM) Imaging

Atomic Force Microscopy (AFM) is a high resolution, a non-optical imaging technique that was initially employed in 1985. It is a very powerful imaging tool that provides non-destructive, precise measurements of the topological, electrical, chemical, and a variety of other properties of a sample surface. The AFM can be

used to obtain 2D and 3D images,where Scanning electron Microscopy (SEM) provides 2D projections from two dimensional images of the sample.The operation of AFM is presented in figure 4.3(a).The AFM probe consists of a cantilever with a sharp tip located on top of the sample. The tip is typically made of silicon or silicon nitride. A piezoelectric scanner controls the tip and its vertical position on the sample's surface. As the AFM tip scans through the surface of the sample, it comes across regions of different heights, therefore the tip's height position is varying. This deflection is monitored using a laser with its beam striking the tip. The reflected beam is directed to a photodetector. The obtained DC signal passes through a detector and a series of electronics. A feedback loop algorithm is used, which is an algorithm that takes part of the output and converts it to input to maintain an optimum situation, meaning that a series of positive and negative feedback loops will keep the system optimized by avoiding tip damage. This mechanism controls the vertical extension of the scanner to keep a constant deflection and hence a constant interaction force. The AFM imaging system can operate in a variety of the following operational modes:

- **Contact Mode:** In contact mode (figure 4.3(b)), the cantilever scans across the surface of the tip by maintaining a constant contact with it and consequently a constant interaction force. The feedback loop is used to achieve constant interaction. The force between the tip and the surface of the sample is repulsive. To minimize damage to the tip and the sample, cantilevers with low spring constants are used. This also helps to enhance the sensitivity of the measurement.

- **Non-Contact Mode:** In this case (figure 4.3(c)), the AFM tip oscillates at a frequency close to its resonance frequency, while it keeps a distance of several nanometers from the sample. In some cases, the feedback loop algorithm might keep a constant interaction between the tip and the surface of the sample. As the tip comes across height deviations in the surface of the sample, when the tip is very close to the surface, the oscillating amplitude damps. This mode provides a more precise force control and high-resolution images

- **Tapping Mode:** In tapping mode (figure 4.3(d)), the AFM tip oscillates through an piezoelectric actuator located at the cantilever.This produces oscillations of a frequency at or near the resonance frequency. The tip reaches a close distance from the surface of the sample and touches it slightly.

Because of the contact with the sample's surface, the oscillation is damping. The feedback loop keeps the amplitude and the interaction produced by the cantilever constant. In this mode, the interaction forces between the sample and the tip are repulsive. The tip-surface distance must be small, otherwise, as we see from figure 4.3(e) this interaction force can become attractive. For tapping mode, cantilevers with spring constants ranging from 10-100 N/m are used along with oscillation frequencies of several kHz. These conditions do not allow cantilevers to stick to the surface due to attractive forces. For soft samples, low spring constants from 0.1-10 N/m are used.

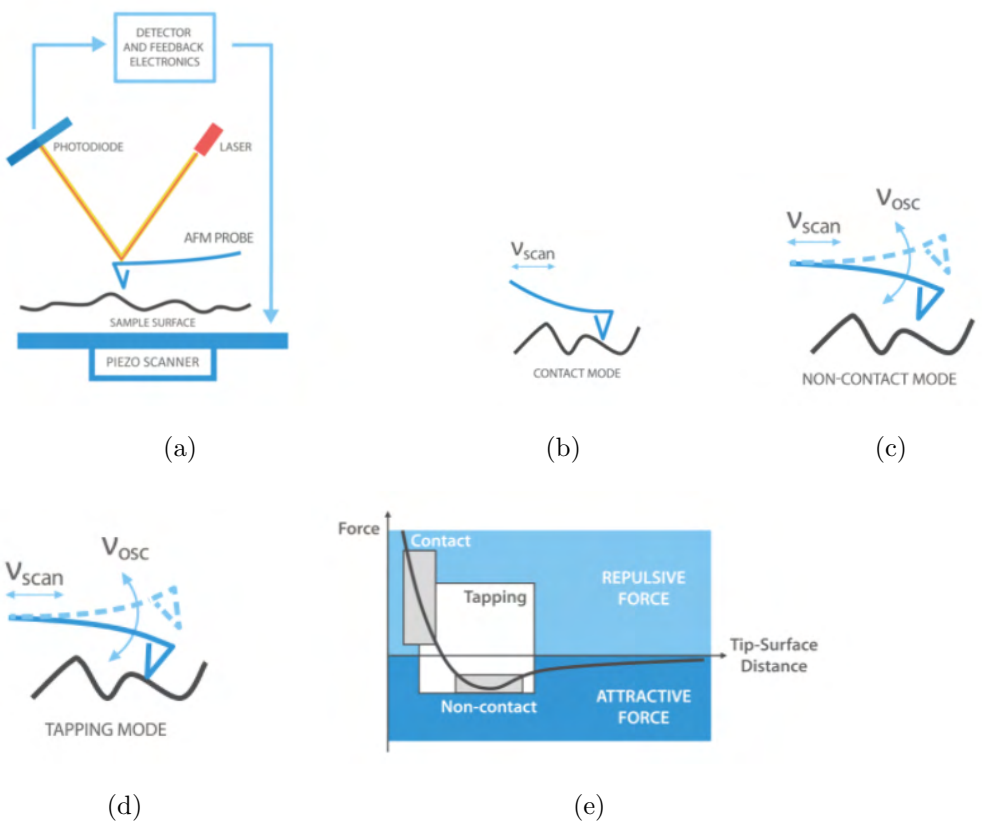

FIGURE 4.3: a)AFM Measurement setup,b)Contact mode measurement,c)Non-contact mode measurement,d)Tapping mode measurement and e)Force-Tip/Surface distance plot [153]

4.3 Uv-Vis Spectroscopy

Knowledge of the absorption properties of each component used in PSCs is very important. The absorption of perovskite components is in the visible range of 400-800nm and should be as strong as possible to optimize the charge generation

process. On the other hand, charge transport layers such as the ETL or HTL should have minimal absorption and strong transmittance in the visible range, to minimize optical losses. The absorption properties of materials can be studied by obtaining their spectra in solution or as thin films. In this thesis, all absorption spectra are obtained from thin films. A Uv-Vis measurement setup is shown in figure 4.4(a) [154].Usually, Tungsten or Deuterium, or both bulbs are used, which produce continuous spectra. The light beam contains a large number of wavelengths (white color). These colors are separated through a monochromator, which is used for wavelength splitting. The splitting is achieved through a diffraction grating. For different rotation angles of the grating, different wavelengths transmit. The beam is then focused through a slit. This scan occurs for wavelengths ranging from 200-800nm. Then, the beam passes through the sample and the light intensity is monitored through Oftentimes, the beam splits into two separate beams. The first is for a reference sample and the second for the measured sample. In the case of measuring thin films, the reference could be a substrate without the coated film and the second the substrate with the deposited film. Absorption measurements can be described using the Beer-Lambert law. According to figure 4.4(b), the initial intensity of the beam is I_0, and the intensity after passing through the sample is I.These two intensities are related through the formula

$$I = I_0 \cdot \exp\left(-\alpha \cdot d\right) \tag{4.3}$$

where α is the absorption coefficient in cm^{-1} units and d is the thickness of the thin film. The spectrophotometer returns as an output result in the absorbance A, which is defined as

$$A = \ln \frac{I_0}{I} \tag{4.4}$$

Inserting equation 4.4 into 4.3, we get an expression for the absorption coefficient:

$$\alpha = \frac{1}{d} \cdot A \tag{4.5}$$

Reflectance and Transmittance measurements can also be performed through a Uv-Vis setup by measuring the intensity of the light reflected or transmitted from the sample. Transmittance (T) and absorbance (A) are related to the formula

$$A = 2 - log_{10}(\%T) \tag{4.6}$$

Regarding Uv-vis measurements in semiconducting materials, the bandgap can

be estimated using tauc's plot. The quantity $(\alpha hv)^{\frac{1}{n}}$ is plotted as a function of hv. The semiconductor can be either direct or indirect bandgap, yielding two possible outcomes [155, 156]:

- If n=$\frac{1}{2}$, The semiconductor has a direct bandgap
- If n= 2, the semiconductor has an indirect bandgap

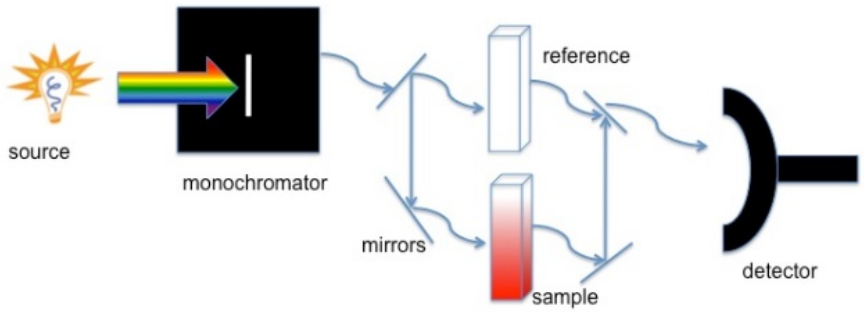

(a)

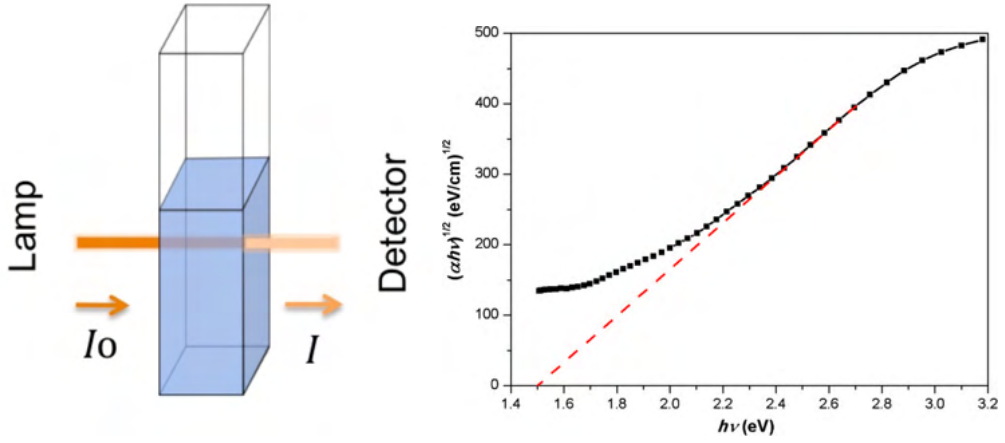

(b) (c) .

FIGURE 4.4: a)Uv-Vis measurement setup,b)Schematic illustration of the Beer-Lambert Law and c) Tauc plot for calculating the bandgap of the indirect Si semiconductor.[154, 157, 158]

An example of the tauc plot is shown in figure 4.4(c), where the bandgap of amorphous Si, which is an indirect bandgap semiconductor, is calculated by fitting a straight line to the linear part of the plot. The y axis is the $(\alpha hv)^{\frac{1}{2}}$, as we are in the case n=2 for the indirect bandgap semiconductor. A similar approach is applied for the calculation of the bandgap of the perovskite, which is a direct bandgap.

4.4 Cyclic Voltammetry

Cyclic Voltammetry (CV) is an electrochemical technique that measures the current response of a solution that is redox-active under the application of a linearly varying cycled voltage sweep. This technique is useful for studying the thermodynamics of the redox process, estimating the HOMO or LUMO of the material, and studying the kinetics of reactions where electron transfer occurs. In general, Voltammetry is any technique where the current is measured between two electrodes where their potential varies. The measured current originates from electron transfer between the redox compound and the electrodes. The current transfers through the solution by diffusion or migration of ions. While in theory a two-electrode system is considered voltammetry, in practice it is very difficult to be stable since redox events at the working electrode resist the potential from remaining constant while passing a current. As a consequence, a three-electrode system is used to separate the role of having a reference applied potential to balance the produced current. One electrode is used as a reference, one is the working electrode and the last is the counter electrode. As pictured in figure 4.5(a), a circuit is formed that consists of the solution with the material of interest (analyte), the two electrodes (plus the reference not shown here), and the potentiostat which controls the voltage of each electrode. If the voltage sweep (changing the electrode potential) was in one direction and stopped there, the experiment would be called a linear sweep voltammogram. However, if we reverse the voltage sweep direction, we have now performed a cyclic voltammogram. As illustrated in figure 4.5(b), the analyte or material of interest in the electrolyte solution, will undergo reduction if the potential energy of the electrode is higher than that of the analyte, therefore it is energetically favorable for the analyte to gain an electron. In the opposite case, if the potential of the analyte is higher than the potential of the electrode, it is preferable in terms of energy for the analyte to lose an electron and oxidize. In both cases, the main target is the minimization of the potential energy of the system. The potentiostat alters the applied potential and then we observe where the current is flowing to learn the electron transfer dynamics of the analyte. The voltage is applied between the working and the reference electrode, and the current is measured between the working electrode and the counter electrode. The potential is affected by the electrolyte, the solvent, and the nature of the working electrode.

The CV curve is shown in figure 4.6(a),4.6(b). In most cases, Ferrocene (Fc/Fc^{+}) is used as a reference. The CV curve has a "duck shape". The upper part (facing upwards) of the curve corresponds to oxidation, while the symmetric part facing

downwards is the reduction process. In these regions, there are two peaks due to oxidation and reduction. So, how does the duck shape of the CV curve occurs?

The peaks on the voltammogram appear due to redox species-our material of interest. To measure the electron transfer properties of the analyte, reference material is used. The most common is Ferrocene (Fc). The equilibrium state is described through the Nernst equation, which relates the potential of an electrochemical cell E with the standard potential of a species E^0 and the relative activities of the oxidized and the reduced analyte in equilibrium. Hence,E^0 is obtained through the reference material, which is Fc.The Nernst equation is described by equation 4.8

$$E = E^0 + \frac{RT}{nF} \cdot \ln\left(\frac{\alpha_{Ox}}{\alpha_{Red}}\right) \tag{4.7}$$

,where R is the universal gas constant, T is the temperature, F is Faraday's constant, and n is the number of electrons and α_{Ox}, α_{Red} are the activities of the oxidation and reduction process. Activity is defined as the effective concentration of a species in non-ideal conditions. It corresponds to the effective chemical potential of a solution rather than an ideal one. If the formal potential E^0 is measured under ideal conditions (activity of all species=1,temperature=298K and pressure=1bar), then the standard potential is replaced by the formal potential $E^{0'}$.In addition, the activities are replaced by the respective concentrations of Fc and Fc^+. If the number of electrons is set to 1, the Nernst equation is converted into

$$E = E^{0'} + \frac{RT}{F} \cdot \ln\left(\frac{[Fc]}{[Fc^+]}\right) \tag{4.8}$$

the concentrations are preferred because they are directly linked with the experiment. The formal potential is specific to the experimental conditions and is often estimated by the experimental $E_{1/2}$ value called half potential. In a conclusion, the Nernst equation provides knowledge about the response of the system when the concentration of its species or the electrode potential is changing. When a potential $E^0 = E^{0'} = E_{1/2}$ is applied,the Nernst equation predicts that for the case of Fc the system will be reduced to Fc until $[Fc] = [Fc^+]$.When the Fc^+ solution is scanned to negative potentials,Fc^+ reduces to Fc near the electrode which leads to a measured current and depletion of the Fc^+ ions at the surface of the electrode.The concentration versus distance is plotted in the figure 4.6(a) ,where Fc^+ (blue line) and Fc (green line) and correspond to different points of the voltammogram. The concentrations of Fc^+ vs Fc as a function of distance from the surface of the electrode are dependent on the applied potential and how species

are moving between the surface of the electrode and the bulk of the solution. All these factors contribute to the "duck" shape voltammogram.

Returning to figure 4.6(a), when the potential is scanned negatively (cathodic) from A to D,Fc^+ depletes near the electrode as it converts to Fc. At point C, where the peak cathodic current (i_{pc}) is observed, the current is governed by providing additional Fc^+ ions from the bulk solution. The volume of the solution at the surface of the electrode containing the reduced Fc (called diffusion layer) increases through the scan. This slows down the mass transport of Fc^+ to the electrode. When the scan progresses to more negative potentials, the diffusion rate of Fc^+ from the bulk to the electrode surface slows down further and the current increases as moving from C to D. When the switching potential D is reached, the direction of the scan is reversed and the scan now continues to the positive potential (anodic) direction. As the concentration of the Fc^+ ions from the electrode surface is depleted, the concentration of Fc at the electrode surface increases, and the Nernst equation is satisfied. Then, the Fc present at the electrode surface oxidizes back to Fc^+ as the positive potential further increases. At the points B and E the concentrations of Fc and Fc^+ at the electrode are equal. The Nernst equation then yields E=$E_{1/2}$. This is the halfway potential between the observed peaks C and F which can lead to a straightforward calculation of $E^{0'}$. The peaks are separated due to the diffusion of the analyte to and from the electrode. Then, the halfway potential is calculated by the average of the anodic cathodic peak potentials (E_{pc}) and (E_{ap})

$$E_{1/2} = \frac{E_{pc} + E_{ap}}{2} \tag{4.9}$$

Another parameter that affects the obtained voltammogram is the scan rate of the applied potential. Fast scan rates can lead to a decrease in the size of the diffusion layer, which leads to higher observed currents. Electron transfer processes involving redox species free to diffuse are described by the Randles-Sevcik equation:

$$i_p = 0.446nFAC^0 \left(\frac{nFvD_0}{RT}\right)^{1/2} \tag{4.10}$$

,where i_p is the cathodic peak current,n is the number of electrons transferred in the redox event,A is the area of the electrode (cm^2),$D_0(cm^2\ s^{-1})$ is the diffusion coefficient of the oxidized analyte and C^0 (mol cm^{-3}) is the Bulk concentration of the analyte.It then follows from equation 4.10 that the cathodic peak current depends on the square of the voltage scan rate. The HOMO level can be then

calculated from the empirical equation [159]

$$E_{HOMO}(eV) = -e[E_{ox} + 4.4] \tag{4.11}$$

,where E_{ox} is the onset oxidation potential which is calculated from the CV curve as illustrated in 4.6(b).

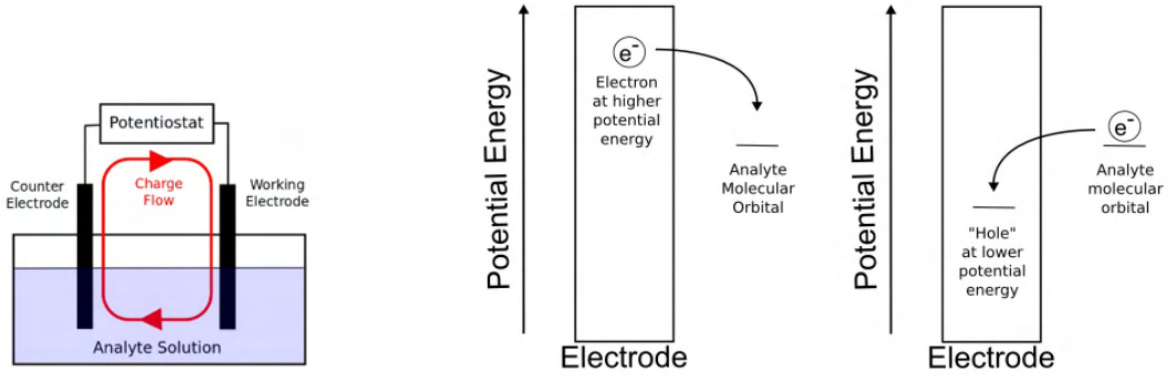

(a) (b)

FIGURE 4.5: a) Circuit diagram and charge flow in CV,b) Interaction between the electrodes and the analyte. [160]

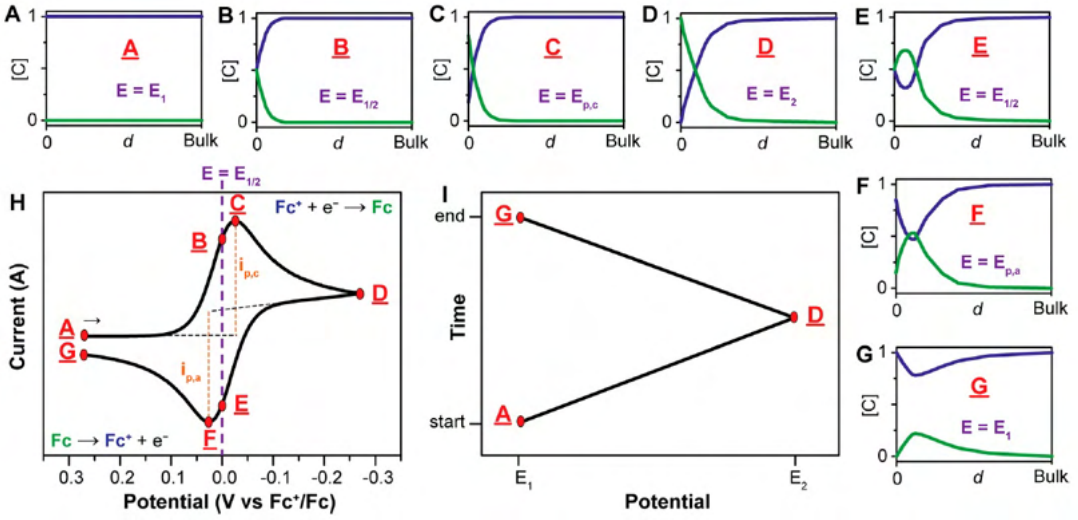

(a)

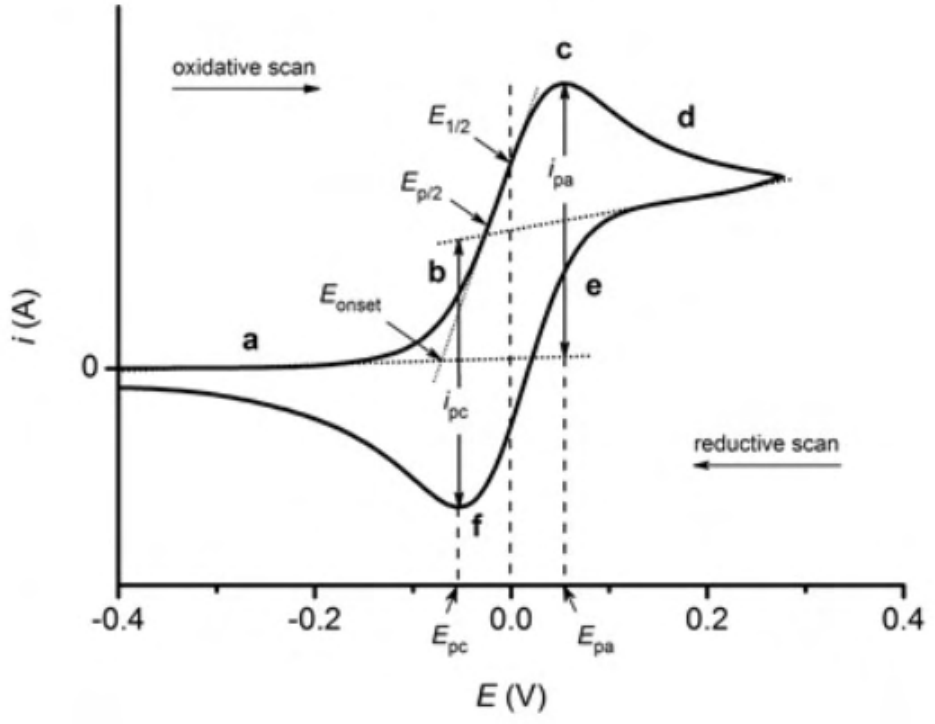

(b)

FIGURE 4.6: a) Step-by-step Breakdown of a CV Voltammogram, b) Typical CV curve with denoted quantities to calculate the halfway potential and the HOMO energy level [161, 162]

4.5 Steady-State and Time-Resolved Photoluminescence Spectroscopy

4.5.1 Steady State Photoluminescence

PL is a non-destructive technique that measures the light emission of any material after excitation (absorption) from a light source. To gain a better understanding of the PL process, it is best to start from a Jablonski diagram as shown in figure 4.7(a),4.7(b).This is an energy diagram with the vertical axis representing energy. Every column represents a specific spin multiplicity. The bold lines represent energy eigenvalues of the electronic states, while the lines underneath represent the various vibrational energy levels for each electronic state. Each vibrational energy level can be further divided into rotational energy levels. After the absorption of a photon of a single energy, the system relaxes by many different possible processes. The absorption process is rapid and leads to the excitation of an electron in a higher energy state (purple arrow). The first possible relaxation process is vibrational relaxation, a non-radiative process (blue arrow). If the electron is excited in a state higher than the first excited state, the vibrational energy levels have a stronger overlap with the electronic levels. This can lead to a transition from a vibrational energy level of an excited state to a lower vibrational level of another excited state (green arrow). This process is called Internal Conversion. Another relaxation mechanism is the Fluorescence (or PL) process (red arrow) (figure 4.7(b), in which the electron falls back to the ground state emitting a photon. This transition occurs commonly between the ground state and the first excited state because in higher energy states the relaxation occurs through vibrational relaxation or internal conversion. This transition is radiative and the energy of the emitted photon is always less than the energy of the photon that excites the electrons due to energy dissipation through vibrational relaxation or internal conversion. Another relaxation mechanism is intersystem crossing. In this case, the electron changes spin multiplicity from singlet (S) to triplet (T). This transition is usually slow and forbidden but if vibrational coupling factors are introduced into the selection rules, the transition becomes weakly allowed. The electron then relaxes with a process called Phosphorescence, where the electron falls back to the ground singlet state by emitting a photon. The timescale of each phenomenon and an indication whether is radiative or not is shown in Table 5.1.

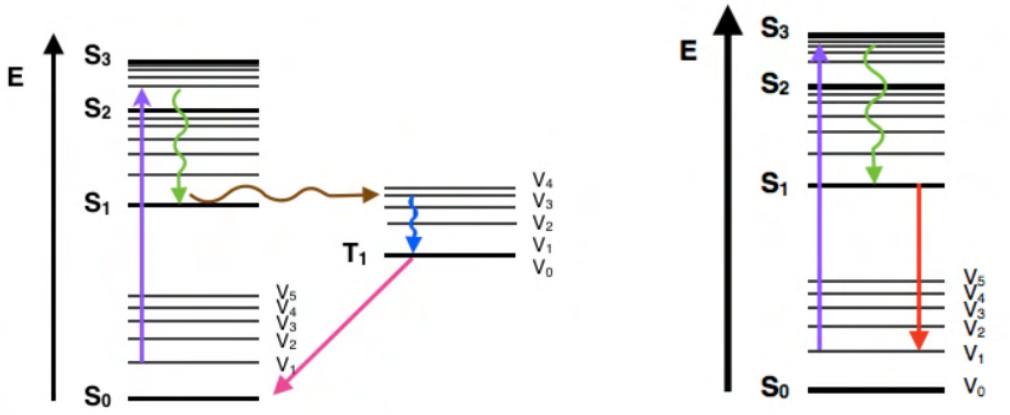

(a) (b)

FIGURE 4.7: a)Jablonski diagram with absorption (purple),internal conversion(green),Intersystem crossing (brown),vibrational relaxation (blue) and fluorescence (pink),b) Jablonski diagram with the processes of absorption (purple),internal conversion and vibrational relaxation (green) and Fluorescence (red). [163]

TABLE 4.1: Jablonski Diagram processes,Time scale and which of them are radiative [163]

Transition	**Time Scale (s)**	**Radiative Process?**
Absorption	10^{-15}	Yes
Vibrational Relaxation	$10^{-14} - 10^{-11}$	No
Internal Conversion	$10^{-14} - 10^{-11}$	No
Fluorescence	$10^{-9} - 10^{-7}$	Yes
Intersystem Crossing	$10^{-8} - 10^{-3}$	No
Phosphorescence	$10^{-4} - 10^{-1}$	Yes

Let's now study the PL process in semiconductors. Semiconductors can either be direct on indirect bandgap. In both cases, for PL to occur, the energy of E the photons used for the excitation must be greater than the bandgap of the semiconductor E_g.In other words, the condition $E > E_g$ must be satisfied. In the case of direct semiconductors, the incoming light excites an electron from the VB to CB, leaving behind a hole. The electron relaxes then into the bottom of the CB by emitting phonons. When the electron reaches the bottom of the CB and the hole at the top of the VB, they recombine radiatively or non-radiatively. The momentum of the photon is negligible compared to the electron, so the recombination occurs in the same value of the crystal momentum k=0.Direct transitions are showed in figure 4.8(a).

The situation is completely different for the case of indirect gap materials shown in figure 4.8(b). In this case, the top of the VB and the bottom of the CB are not in the same k in the Brillouin zone, therefore phonon absorption or emission is required to conserve the momentum. This requirement makes this process a second-order, hence the transition probability decreases. The radiative recombination lifetime is consequently much longer than for direct transitions. This makes the PL process not very efficient, hence indirect semiconductors such as Silicon or Germanium are not preferred for light-emitting applications.

A typical PL setup is presented in figure 4.9(a). This consists of a laser or a bulb that produces a beam of a single wavelength or a variety of wavelengths, the sample of interest where the beam strikes, several lenses or other optical elements to collect the emitted light, and a spectrometer with a diffraction grating to measure the response for each wavelength. The sample oftentimes is placed in a cryostat to obtain a strong enough PL signal to overcome the noise. This is due to the exciton binding energy in some materials. When the exciton binding energy is smaller than the thermal energy $K_BT \approx 25$meV, then no excitons are observed at room temperature.

Perovskite materials exhibit strong PL at room temperature. PL measurements are used to observe how the charge transfer process is affected after different types of device modifications to enhance the PCE such as defect passivation or use a different charge transport layer. The effect of PL quenching is studied. PL quenching is the process of the reduction of the PL intensity. This can be due to charge transfer, energy transfer, or the presence of defect states. For example, a pristine n and p-type semiconductor have an intense emission peak. If these materials are brought together, the PL emission intensity drops due to charge transfer between the electron donor and acceptor [164]. In perovskite compounds, PL quenching (figure 4.9(b) [165]) is an indicator of efficient charge transport and extraction. At V_{OC}, perovskite compounds should ideally be strong light emitters, which shows no severe recombination effects. Furthermore,PL peak shifts can provide information about the increase/decrease of non-radiative recombination.

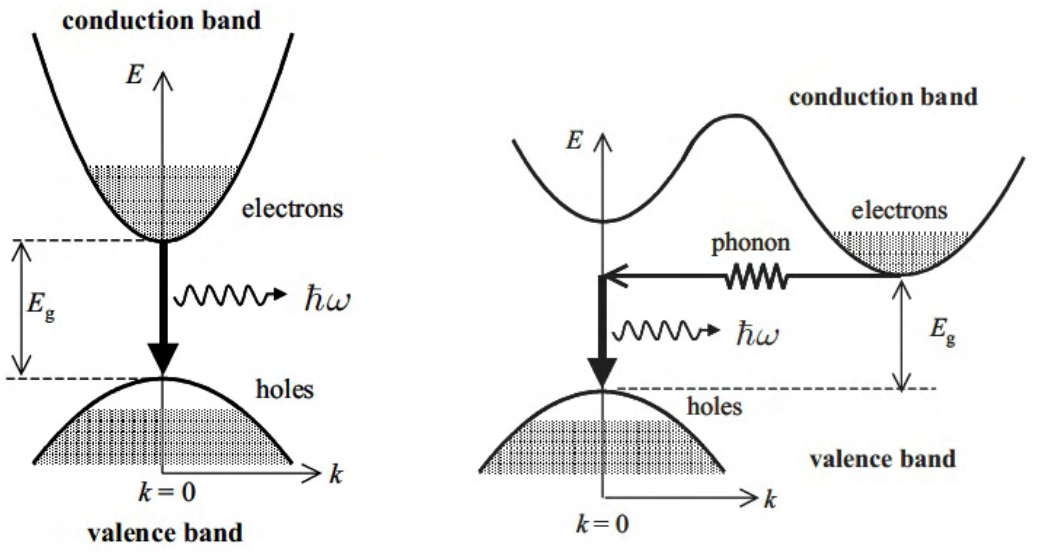

(a) (b)

FIGURE 4.8: a)PL in direct semiconductors, b)PL in Indirect semiconductors [166]

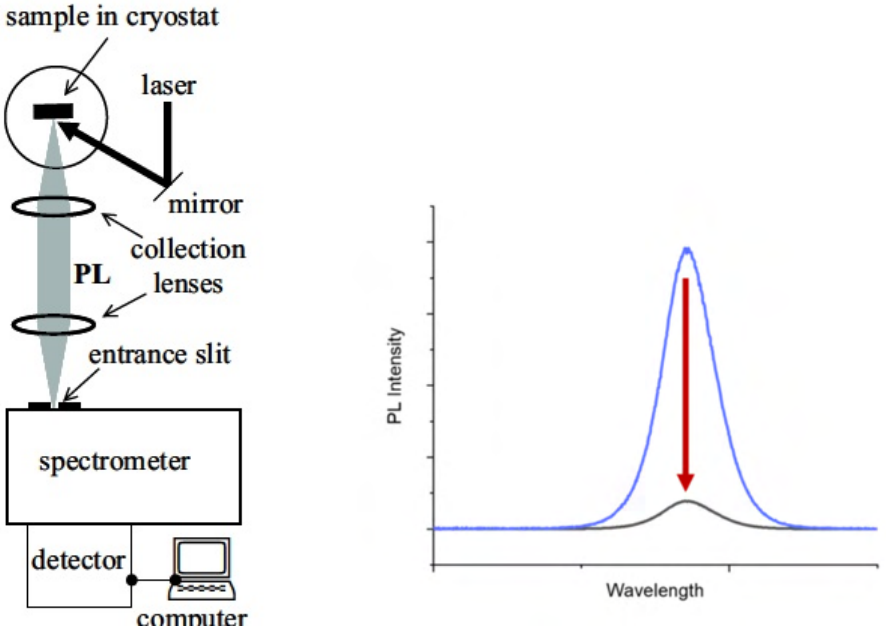

(a) (b)

FIGURE 4.9: a)Typical Experimental setup of a PL measurement,b)Illustration of PL quenching [165, 166]

4.5.2 Time Resolved Photoluminescence

The TRPL is a technique that can study the time evolution of the fluorescence in a sample. It is a non-destructive method that provides information about the exciting species of a sample. The timescale of fluorescence and its nature have been analyzed in the previous section. TRPL relies on the Time Correlated Single Photon Counting (TCSPC) technique. The experimental setup of TRPL is presented in 4.10(a). This method detects single photons and measures their arrival times on the detector concerning a reference signal, typically the light source. TCSPC is a statistical method that requires a light source with a high repetition rate. A sufficient number of photon events are required to obtain statistical data precision. The light source is typically a monochromatic pulsed laser with a high repetition rate, on the order of MHz.The wavelength of the laser should be sufficient to excite the sample. A light pulse by the laser is emitted as a reference signal which is considered as the START pulse. The detection of the reference signal enables the time recording in the system. Afterward, another pulse is emitted from the laser through the sample, which re-emits light (Photoluminescence). The signal from the sample reaches then the detector after a time interval t which acts as a STOP signal and the system stops recording time. The time interval between the START and the STOP signal is a single photon event which is stored as a memory value in a histogram that displays photon events as a function of time. Due to the high repetition rate of the laser, millions of START-STOP signals can be measured in a short period. The photodetectors that analyze the signal are typically photomultiplier tubes Photomultiplier Tubes (PMT). Photomultipliers convert an incoming photon to an electron by interacting with a photocathode. The electron is then accelerated by another electrode(s) to multiple dynodes(metal plates). After striking each dynode, multiple electrons are also released, leading to signal amplification. However, PMTs are not that suitable for fast detection. Instead, micro channel photomultipliers or photon Avalanche photodiodes are also employed. It is crucial to ensure that no more than 1 photon is detected per light pulse. Multi-photon signals can affect the histogram statistics and yield erroneous measurement results. This issue is known as the "Pulse pile-up problem".This originates from the fact that the detector and the electronics have a "dead time" after a photon is detected and then they cannot respond for some time (figure 4.10(b)). For this reason, the STOP pulse rate must be kept low, typically below 5% of the START rate [167].

An example of a TRPL decay is presented in figure 4.10(c). It is crucial for every recorded decay to also record the Instrument Response Function (IRF). This function contains all the contribution from detector electronics and the contribution from the laser pulse that affects the obtained signal histogram. Hence, the excitation laser source sets the lowest limit of detection. If however, the TRPL decay is close to the IRF, it means that the data are convoluted and we cannot be confident about the measured decay. From TRPL measurements we can obtain the lifetime of the excited species. If n(t) is the population of the excited species, this population can be effected either by radiative or non-radiative recombination. Furthermore, the recombination rate depends on the number of charge carriers. This means that the number of exciting species varies as shown in the equation 4.12:

$$\frac{dn(t)}{dt} = -(k_{rad} + k_{non-rad}) \cdot n(t) \tag{4.12}$$

,where k_{rad},$k_{non-rad}$ are the rates of radiative and non-radiative recombination respectively.The solution leads to the expression

$$n(t) = n_0 \cdot \exp(-t/\tau) \tag{4.13}$$

, where τ is the lifetime. The intensity of the measured signal is proportional to the number of the excited species, $n(t) \propto I(t)$. If the decay is mono-exponential, then $I(t) = I_0 \cdot \exp(-t/\tau)$. However, if more than one component are contributing to the decay, then for i-contributions it follows that

$$I(t) = \sum_{i=1}^{N} A_i \cdot \exp(-t/\tau_i) \tag{4.14}$$

,where A_i are the pre-exponential factors and τ_i is the lifetime of each process. The fractional contribution of each decay component can be estimated as:

$$\phi_i = \frac{A_i \cdot \tau_i}{\sum_{i=1}^{N} A_i \cdot \tau_i} \cdot 100\% \tag{4.15}$$

and the average lifetime can be calculated through the equation

$$\tau_{avg} = \frac{\sum_{i=1}^{N} A_i \tau_i^2}{\sum_{i=1}^{N} A_i \tau_i} \tag{4.16}$$

The exponential fitting function has the form

$$R(t) = B + A_1 \cdot \exp(-t/\tau_1) + A_2 \cdot \exp(-t/\tau_2) + ... \tag{4.17}$$

,where B is introduced to take into account noise correlated to the electronics of the measurement. An important parameter that governs the quality of the fitting is the χ^2 factor, defined as:

$$\chi^2 = \sum_k w_k^2 \frac{(F_k - S_k)^2}{n} \tag{4.18}$$

,where w_k is a weighting factor for individual data points,F_k are the data points of the fitted curve,S_k are the measured data points and n is the number of free parameters which is approximately equal to the number of fitted data points subtracted by the number of lifetime parameters used in the fit. The χ^2 does not depend on the number of data points or fitting parameters. For data following a Poisson distribution, the limit for a good fit is χ^2=1. However, values of 1.1-1.3 can still be acceptable under certain conditions. If the fitting has been inappropriately chosen, then χ^2 is less than 1.

For perovskite compounds, TRPL decays can be recorded in a variety of stacks as shown in figure 4.10(d). The complexity of the measurement increases as we move to the right and adding layers. The charge carrier dynamics that are affected by generation-recombination, diffusion and drift are governed by the continuity equation:

$$\frac{dn}{dt} = G_{ext}(x,t) + G_{int}(x,t,n,p) - R(x,t,n,p) + D_n \frac{d^2n(x,t)}{dx^2} + E\mu_n \frac{dn(x,t)}{dx} \tag{4.19}$$

where x is the coordinate normal to the layer surface,t is the time, G_{ext} is the generation rate of e-h pairs due to external illumination (light),G_{int} is the generation rate due to the absorption of photons generated by radiative recombination within the device, a phenomenon known as photon recycling, that takes place in perovskites. R is the recombination rate, $D_n = \mu_n \cdot \frac{K_B T}{q}$ is the diffusion coefficient for electrons or holes with,$\frac{K_B T}{q}$ is the thermal voltage,E is the electric field and μ_n is the electron mobility.Depending on the studied mechanism, whether it is perovskite passivation or modifications in charge transport layers, the used fitting function has two components. The first component τ_1 or fast component is related to interface recombination or charge transport, and the second with non-radiative recombination originating either from the bulk or from the interface [168–171].

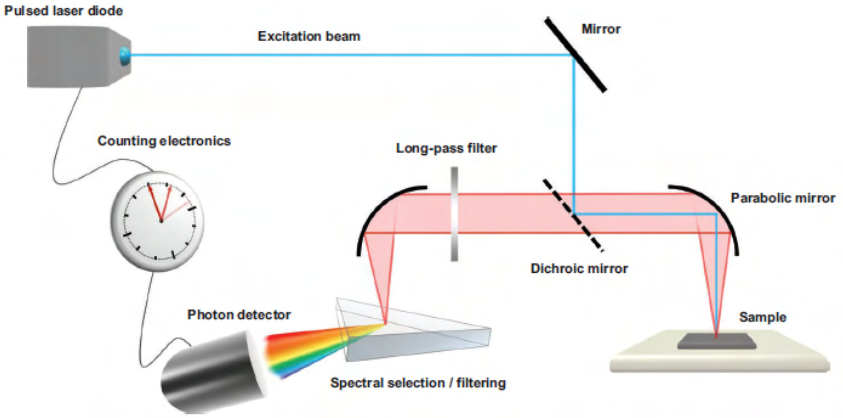

(a)

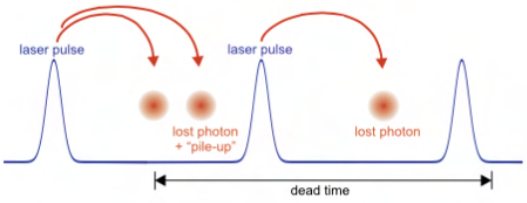

(b)

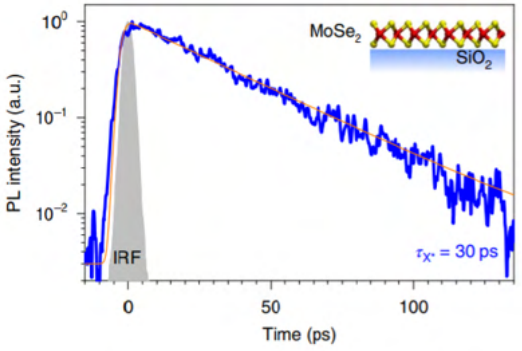

(c)

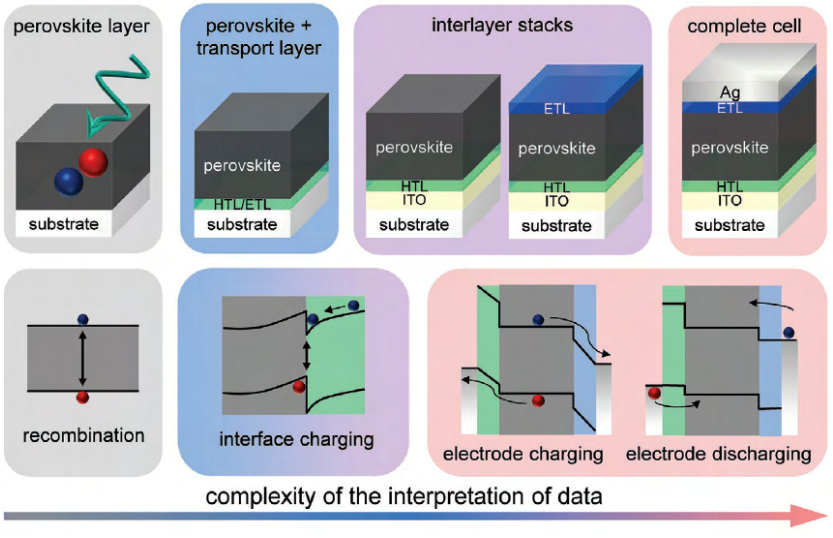

(d)

FIGURE 4.10: a)Typical setup for TCSPC measurements,b)The "pulse pile-up" effect in TCSPC measurement and c)A typical TRPL decay with the indicated IRF for a 2D material in SiO_2 substrate and d)Complexity of interpreting data in TRPL by adding various layers [172–175]

4.6 IV Characterization of solar cells

The IV curve of a solar cell diode is the fundamental characterization method of solar devices. The first and the absolute parameter that shows how efficient a device is is the PCE.The PCE is extracted by three parameters: 1) The V_{OC}, the 2) Short Circuit Current Density (J_{SC}), and the 3) FF. In addition to these parameters, the IV curve is also affected by resistive effects. A typical IV curve is presented in figure 4.11. The current increases exponentially with increasing voltage as predicted from the diode equation. The V_{OC} and the J_{SC} represent the maximum theoretical voltage and current for a solar cell for zero current and voltage respectively, or open circuit and short circuit. In practice, every solar cell has an optimum operation point in the IV curve, which produces the highest output power, the Maximum Power Point (MPP). The MPP curve exhibits this single maximum point. The FF is the ratio between the output power in the MPP and the maximum theoretical power by the cell,

$$FF = \frac{V_{MP} \cdot I_{MP}}{V_{OC} \cdot J_{SC}} \tag{4.20}$$

Geometrically, this can be expressed as the ratio of the area A and area B under the IV curve as shown in figure 4.11. In a laboratory environment, the photovoltaic parameters are extracted by using a solar simulator. The PCE can be defined as the ratio of the maximum power produced by the cell (P_{MAX}) divided by the power of the radiation incident on the device (P_{INC}):

$$PCE = \frac{P_{MAX}}{P_{INC}} \tag{4.21}$$

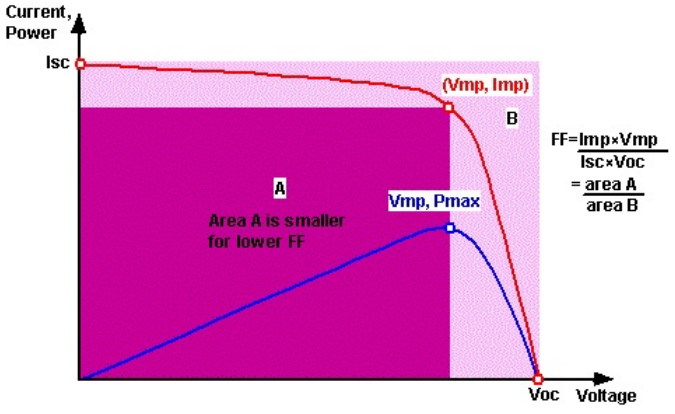

FIGURE 4.11: Characteristic JV and power curve with graphical illustration of the Fill Factor [176]

In laboratory conditions, the PCE measurement is performed by using a solar simulator setup,which is shown in figure 4.12(a). It consists of a power supply source that will apply a voltage on the device, which is connected by two terminals or a board system. The current response of the device is then measured by coupling the simulator with a computer, where the IV curve is obtained by using the software. A lamp is used to produce a steady power output. The spectrum of the lamp is filtered by using an Air Mass Global (AM1.5G) filter and a collimated lens to produce a diffuse and homogeneous light beam for the solar cell. The measuring protocol of solar cells involves the use of the AM1.5G spectrum. The typical incident power where the JV curves are obtained is at 100 mW/cm^2 one sun illumination. As illustrated in figure 4.12(b), the Air Mass is defined as the path length of the solar radiation at an angle θ through the atmosphere, divided by the shortest path length. The shortest path length is when sunlight is overhead. When the sun is at an angle θ, the air mass is defined as

$$AM = \frac{1}{cos\theta} \tag{4.22}$$

The PCE of a solar cell is sensitive to changes in the power or spectrum of the incident radiation.To have comparable results when efficiencies are measured in different locations and times, a standard spectrum is defined for the Earth's surface and outside the Earth's atmosphere: The standard spectrum at the Earth's surface is the so-called AM1.5G spectrum, which corresponds at an angle from the vertical sunlight position of 48.2°, while the standard spectrum outside the Earth is the AM0 spectrum. The AM1.5G spectrum is pictured in figure 4.12(c).

Among the 4 main photovoltaic parameters, it is useful to study a solar cell in a circuit model to account for resistive effects. The circuit representation is shown in figure 4.12(d). Solar cells are modeled by two different resistors, the Series Resistance (R_S) and the Shunt Resistance (R_{SH}). The series resistance is graphically calculated close to the open circuit Voltage region (figure 4.12(e)) as

$$R_S = \frac{\partial J}{\partial V}\bigg|_{V=V_{OC}} \tag{4.23}$$

As the slope increases, the JV curve "bends" as depicted in figure 4.12(e) . The Shunt resistance can be graphically estimated near the short circuit current point as

$$R_{SH} = \frac{\partial J}{\partial V}\bigg|_{V=0} \tag{4.24}$$

The series resistance is a resistor to model all losses that arise from each layer that makes up a solar cell stack, each material contributes to the resistance up to a limit. The shunt resistance is due to alternate current paths on the device, or shunts, that resist charge extraction. These can include GBs or traps in the perovskite etc. Ideally, the series resistance should be zero or as small as possible and the shunt resistance should be infinite or in practice as large as possible. An enhanced R_S or R_{SH} can have a negative impact on the FF.

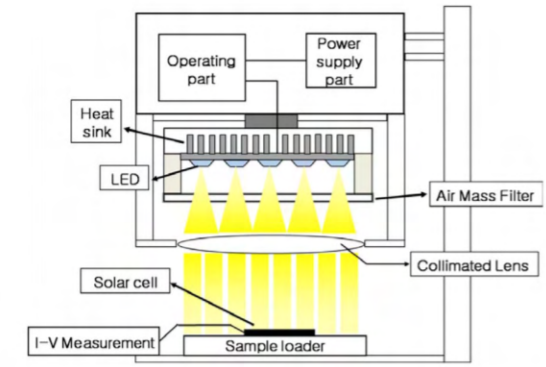

(a)

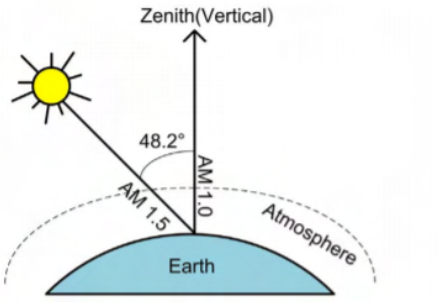

(b)

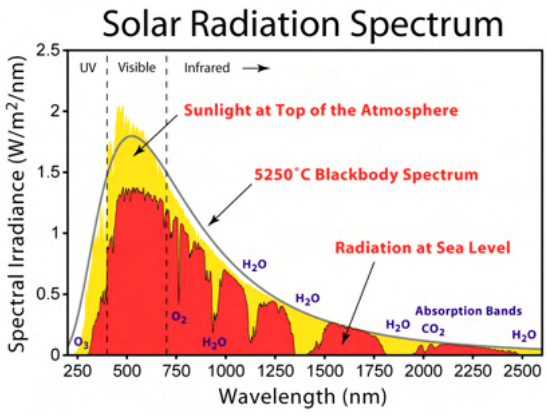

(c)

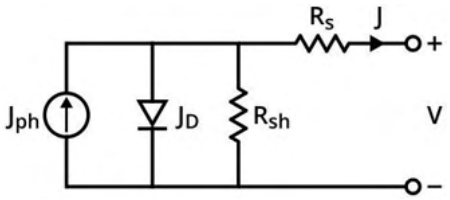

(d)

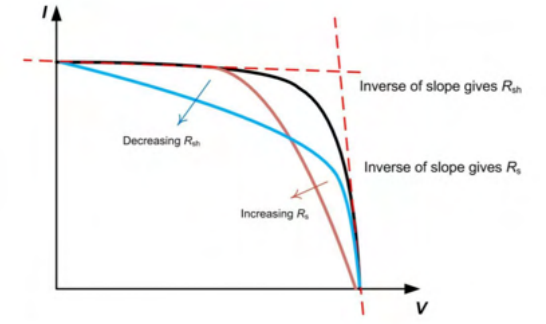

(e)

FIGURE 4.12: a)Solar Simulator setup,b)Illustration of Air Mass,c)The AM1.5G Spectrum,d)Circuit diagram of a solar cell and e)Effect of varying Series or Shunt resistance on the solar cell J-V curve[177–180]

After defining the measurement protocol for devices, we will have a closer look at the photovoltaic parameters by starting from the V_{OC}. The V_{OC} can be calculated from the solar cell diode equation by setting the current equal to 0

$$J = J_0 \cdot \exp\left(\frac{qV}{nKT}\right) - J_{PH} \Longrightarrow V_{OC} = \frac{nkT}{q} \ln\left(\frac{J_{PH}}{J_0} + 1\right) \tag{4.25}$$

Where J_0 is the reverse saturation current, $\frac{kT}{q}$ is the thermal voltage ($\approx$ 25meV),n is the diode ideality factor and J_{PH} is the light-generated current. The above equation shows that the V_{OC} depends on the photocurrent and the saturation current J_0.J_0 is affected by recombination effects in the device as it has a dependence on the diffusion length, hence the V_{OC} is affected by recombination effects in the device. The ideality factor n originates from charge transport and non-radiative recombination losses. Ideality values larger than 2 are associated with severe non-radiative recombination effects. Increasing the diffusion length will lead to a shorter leakage current J_0 and improve the V_{OC}. In PSCs, a variety of strategies can be adopted to improve the V_{OC} such as energy level engineering by for example using an HTL with a deeper HOMO, by using a cathode with a low work function, by using barrier contacts, increasing the Shunt resistance, improving the carrier mobility and lifetime, reducing the energy disorder by improving the crystallinity of the perovskite layer and eliminating non-radiative recombination in the bulk or at the interface, as well as other methods. The V_{OC} originates from the difference between the Quasi-Fermi level ($E_{F,e}$) at the ETL/active layer interface and the hole Quasi-Fermi level at the HTL/active layer interface ($E_{F,h}$). Without taking into account non-radiative recombination, the V_{OC} can be expressed as

$$V_{OC} = \frac{1}{q}(E_{F,e} - E_{F,h}) = E_g - k_B T \ln\left(\frac{n}{N_C}\right) - k_B T \ln\left(\frac{p}{N_V}\right) \tag{4.26}$$

,where n,p are the electron and hole concentration, E_g is the bandgap and N_C,N_V are the effective densities of states for electrons and holes respectively, with values in the range of 10^{18} for perovskites.Therefore, the Quasi-Fermi level splitting (QFLS) (4.13(a)) is determined by the charge density in which the thermal generation rate balances the recombination rate.If interface recombination is considered, the V_{OC} will further reduce compared to taking into account only QFLS. The voltage losses will then be calculated as

$$\begin{aligned}
\Delta E = q\Delta V_{OC} = E_g - qV_{OC} \\
&= (E_g - qV_{OC}^{SQ}) + (qV_{OC}^{SQ} - qV_{OC}^{rad}) + (qV_{OC}^{rad} - qV_{OC}) \\
&= (E_g - qV_{OC}^{SQ}) + q\Delta V_{OC}^{rad,belowgap} + q\Delta V_{OC}^{non-rad} \\
&= \Delta E_1 + \Delta E_2 + \Delta E_3 \approx \Delta E_1 + \Delta E_3 \\
&= qV_{OC}^{SQ} + k_B T \ln\left(\frac{1}{EQE_{EL}}\right)
\end{aligned} \tag{4.27}$$

where V_{OC}^{SQ},V_{OC}^{rad} , V_{OC} are the maximum voltage under the Shockley-Quisser limit,the maximum voltage under the SQ limit and the actual V_{OC} respectively, and EQE_{EL} is the quantum efficiency of Electroluminescence.The term $\Delta E_1 = (E_g - qV_{OC}^{SQ})$ corresponds to the unavoidable energy loss of radiative recombination for absorbing in energies larger than E_g.The term $\Delta E_2 = q\Delta V_{OC}^{rad,belowgap}$ corresponds to losses for absorbing in energies less than the bandgap and the third term $\Delta E_3 = qV_{OC}^{non-rad}$ originates from non-radiative recombination. EQE_{EL} will be high for low non-radiative recombination.The built-in potential V_{bi} can have various definitions such as difference in the work function of the electrons, QFLS,or work function difference between the charge selective contacts,which is represented by the difference between the HOMO($E_{ETL,HOMO}$) of the HTL and the LUMO ($E_{ETL,LUMO}$) of the ETL.The V_{bi} is correlated to V_{OC} through the formula:

$$\begin{aligned} V_{bi} &= (E_{ETL,LUMO} - E_{ETL,HOMO})/q \\ &= (E_{ETL,LUMO} - E_{F,e})/q + \Delta E_F/q + (E_{F,h} - E_{HTL,HOMO})/q \\ &= \phi_e/q + V_{OC} + \phi_n/q \end{aligned} \tag{4.28}$$

where ϕ_e,ϕ_h is the work function of the ETL and HTL respectively and ΔE_F is the QFLS.The presence of the V_{bi} affects carrier dynamics, charge dissociation and transport. Despite that V_{bi} explains the origins of the V_{OC},it can overstimate it.An alternate expression for the V_{OC} is the following:

$$V_{OC} = \frac{nk_BT}{q} \ln\left(\frac{J_{SC}N_D\tau_{eff}}{qn_i^2 d}\right) \tag{4.29}$$

where, n is the ideality factor $\frac{k_BT}{q}$ is the thermal voltage, N_D is the doping density, τ_{eff} is the effective carrier lifetime, n_i is the intrinsic semiconductor concentration and d is the thickness of the active layer. It is evident from this equation that a larger absorption coefficient leads to a higher carrier lifetime and V_{OC}. Strategies related to optimizing the perovskite layer or charge selective contacts can impact the V_{OC}.

The J_{SC} is affected by the area of the solar cell which is the reason that current density is preferred (typically in mA/cm^2), the intensity (or power) of the incoming light, the spectrum of the incident light, optical properties like absorption and reflection and collection probability that depends on the carrier lifetime. The circuit picture is the same as in figure 4.12(d), despite that perovskites are commonly depicted as capacitors in circuit diagrams. In the ideal case, $J_{SC} = J_{PH}$ if we

neglect shunt resistance. The ideal current not affected by Space charge limited effects can be expressed as

$$J_{SC} = J_{PH} = qG(L_e + L_h + W) \propto \eta_{int} = \eta_{drift} + \eta_{dif} \tag{4.30}$$

,where G is the average generation rate in the active layer,L_e,L_h is the electron-hole diffusion length,W is the width of the depletion region,η_{int} is the Internal Quantum Efficiency (IQE) which has contributions from drift and diffusion.These are affected by the absorption coefficient, recombination rates at the front and rear surface of the active layer, the built-in potential, mobility, and diffusion length. The total generation rate is

$$G = G_{PH} + G_{THERM} \tag{4.31}$$

, where G_{PH} and G_{THERM} are the optical and thermal generation rates. The leakage current depends on the thermal generation rate as

$$J_0 = qLG_{therm} \tag{4.32}$$

,while the optical generation rate affects the J_{SC}:

$$J_{SC} = J_{PH} = qLG_{PH} \tag{4.33}$$

The J_{SC} depends strongly on the generation rate and the diffusion length. These parameters are governed by charge generation, transport, and extraction. From thermodynamics, the optical and thermal generation rates can be calculated as:

$$G_{PH}(x, \hbar\omega) = -\eta_{int}(\hbar\omega) \cdot \frac{dI(x, \hbar\omega)}{dx} \cdot \frac{q}{\hbar\omega} \tag{4.34}$$

where, η_{int} is the IQE,$\hbar$ is planck's constant, I is the light intensity,x is a length along the active layer and ω is the frequency of the incoming light.The thermal generation rate is determined by

$$G_{therm} = \beta N_h N_e \exp\left(\frac{-E_g}{k_B T}\right) \tag{4.35}$$

,where $\beta = \frac{q(\mu_e + \mu_h)}{\epsilon_0}$ is the Langevin recombination rate coefficient with electron and hole mobility μ_e,μ_h and vacuum permittivity ϵ_0, N_h,N_e are the total densities

of states for electrons and holes and E_g is the bandgap.The IQE is expressed as :

$$\eta_{int} = 1 + \frac{\exp(-\alpha W)}{1 + \alpha L_e} \tag{4.36}$$

where α is the absorption coefficient,W is the depletion region width and L_e is the electron diffusion length.The depletion width is given by

$$w = \sqrt{\frac{2\epsilon\epsilon_0(qV_{bi} - qV)}{q^2(N_A - N_D)}} \tag{4.37}$$

where ϵ,ϵ_0 are the perovskite and vacuum permittivity,V_{bi}, V are the built-in and the applied potentials and N_A N_D are the acceptor and donor concentrations respectively. The diffusion length that determines the J_{SC} is given by

$$L_e = \sqrt{D_e \cdot \tau_e} = \sqrt{\frac{k_B T}{q} \cdot \mu_e \cdot \tau_e} = \sqrt{\frac{k_B T}{q} \cdot \mu_e \cdot \frac{1}{v_{th} \cdot \sigma_e \cdot N_t}} \tag{4.38}$$

where $\frac{k_B T}{q}$ is the thermal voltage, μ_e is the electron mobility, and $\tau_e = \frac{1}{v_{th} \cdot \sigma_e \cdot N_t}$ is the Shockley Read Hall (SRH) recombination lifetime with v_{th} being the thermal velocity,σ_e is the trap capture cross-section of the electron and N_t is the SRH trap density.The SRH recombination is a monomolecular first-order process and occurs at deep trap states which act as non-radiative recombination centers in the bulk. An enhancement in the J_{SC} can be achieved by three parameters: 1) The perovskite active layer should have a high absorption coefficient and as few defects as possible, which makes crystallinity a very important aspect,2) Use of a transport layer with high charge extraction and aligned energy levels and 3) Surface architecture by employing surface passivation or anti-reflection coatings to reduce optical losses.

The FF losses are illustrated graphically in figure 4.13(b).There are 3 differently colored areas.The yellow area corresponds to radiative losses in a Shockley-Queisser (SQ) manner.The purple zone is related to non-radiative losses and charges transport losses.The FF can be affected both by the V_{OC} and the J_{SC}.FF losses are the result of charge carrier dynamics such as charge generation, transport, recombination, and extraction. Effective charge generation, rapid and balanced charge transport, reduced non-radiative recombination, and charge extraction free of charge losses can enhance the FF. This is because the charge generation in the active layer is inversely proportional to its thickness. This increases the built-in electric field and therefore charge dissociation and extraction by increasing FF and simultaneously reducing the V_{OC}.Reducing the thickness of the charge selective contact can also

reduce the FF due to low carrier mobility that leads to charge accumulation (formation of space charges), leading to low charge dissociation. After charge generation, carriers must be extracted immediately as unbalanced mobilities in the active layer or selective contacts can lead to the formation of space charge limited currents which leads to bimolecular recombination and inefficient charge transport and extraction.Recombination losses can be either SRH or bimolecular, i.e Langevin-type recombination between CB electron and VB hole due to charge accumulation.Suppressing higher-order recombination from the perovskite GBs and increasing charge extraction efficacy at the interfaces improves the FF. Other factors that limit the FF include unbalanced diffusion lengths,large energy-injection barriers,bad contacts,and defective interfaces. The maximum FF by considering the SQ limit is :

$$FF_{MAX} = \frac{\Theta - \ln(\Theta + 0.75)}{\Theta + 1} \tag{4.39}$$

,where $\Theta = \frac{qV_{OC}}{nk_BT}$ The above equation shows that the maximum FF can occur if no further charge transport losses occur.If series and shunt resistance are considered according to the equivalent circuit model, the FF can be obtained by:

$$FF = FF_{SERIES}\left(1 - \frac{\Theta + 0.7}{\Theta} \cdot \frac{FF_{series}}{r_{parallel}}\right) \tag{4.40}$$

,where

$$FF_{SERIES} = FF_{MAX}(1 - 1.1r_{series}) + \frac{r_{series}^2}{5.4} \tag{4.41}$$

and

$$r_{series} = \frac{J_{SC}R_S}{V_{OC}} \tag{4.42}$$

,

$$r_{parallel} = \frac{J_{SC}R_{SH}}{V_{OC}} \tag{4.43}$$

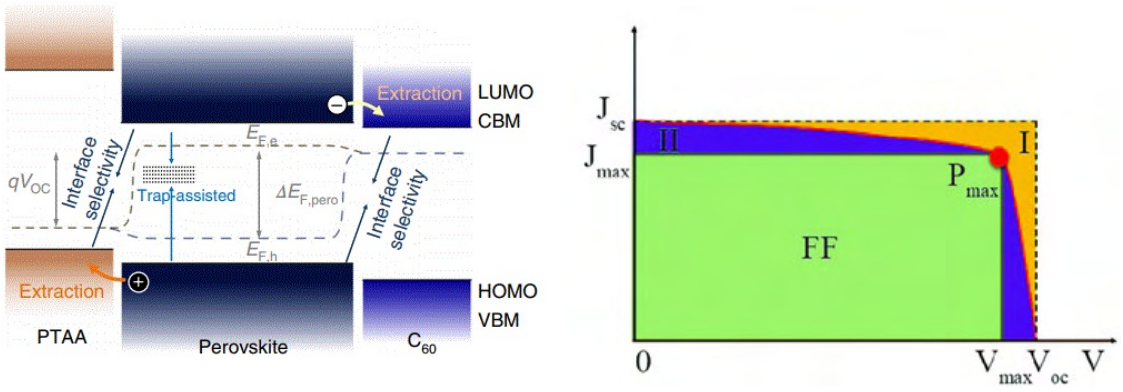

(a) (b)

FIGURE 4.13: a)QFLS illustration in p-i-n PSCs,b)Graphical presentation of FF losses (purple,yellow) [181, 182]

It is evident from equations 4.40,4.41 that a high FF can be obtained by small R_S and a large R_{SH}.Under realistic operating conditions, the resistances are a function of bulk and interfacial charge transport. Optimizing the FF relies on managing carriers by a variety of tactics. The main target is to minimize recombination effects including non-radiative crystallization induced recombination, passivation of GBs, defect passivation or use of different A-site cations, rapid charge transport by balancing mobility and diffusion length.Radiative SQ recombination is unavoidable. We finally have to keep in mind that in physical processes there are trade-offs, as in the case of FF for example we have seen that strategies to enhance FF can reduce the V_{OC}.

4.7 External Quantum Efficiency (EQE) Measurement

From the previous section, the measuring protocol of devices requires the use of a solar simulator with a bulb that simulates a 1sun illumination in the AM1.5G spectrum. However, the photon flux of the simulator does not match the sunlight photon flux, which leads to a spectral mismatch. Hence, the obtained J_{SC} from the solar simulator is not correct. An accurate calculation of the J_{SC} is performed from External Quantum Efficiency (EQE) measurements. The EQE is defined as the ratio of collected charge carriers divided by the number of incident photons in

the solar cell:

$$EQE = \frac{electrons.collected/s}{incident.photons/s} = \frac{I_{PH}(\lambda)}{q} \cdot \frac{1}{\phi(\lambda)} \tag{4.44}$$

, where $I_{PH}(\lambda)/q$ is the photocurrent per charge unit or charge carrier flux and $\phi(\lambda)$ is the photon flux. As an example, if 10 photons are incident on the solar cell and 7 are collected, the EQE is 70%. If we are interested in the number of photons absorbed by the active layer, then we can use the IQE which is defined as the ratio of the number of charge carriers collected by the solar cell to the number of photons of given energy that shine on the solar cell from outside and are absorbed by the cell:

$$IQE = \frac{carriers.collected/s}{absorbed.photons/s} = \frac{EQE}{1 - R - T} \tag{4.45}$$

where R and T are the Transmission and Reflectivity. The IQE can provide information about wavelengths lost due to parasitic absorption or where there are issues regarding the charge extraction process.A typical EQE measurement setup is shown in figure 4.14(a).It consists of a light source, typically a Xenon lamp, which produces a continuous spectrum. The light then passes through a chopper wheel which has an on-off frequency on the order of 120Hz. The chopped light will then pass through a monochromator that selects a very narrow band of wavelengths with the aid of a diffraction grating. Then, the monochromatic, low frequency chopped light is focused on the solar cell by passing through a lens system. The solar cell will then produce a weak alternate current signal with a small amplitude. This signal is converted to Voltage bypassing the current through a resistor and measuring the Voltage drop. The signal then is retrieved by an amplifier. The device is operating at one sun to simulate realistic operation and to keep the QFLS at the real value to monitor recombination effects. In addition, a solar cell is a very light-sensitive device and is hard to block ambient light. The amplifier can filter the response of the solar cell from ambient noise. A computer controls the monochromator, the chopper wheel, and the amplifier. To have a precise knowledge of the photon flux, a reference Si diode is placed to calibrate the system before measuring the device of interest.

The amplifier can filter out the response of the solar cell to the chopped light. This is achieved by comparing the signal's frequency with the frequency of the chopper wheel. The frequency of the chopper wheel is such that it blocks frequencies that produce noise. The amplifier uses the signal from the chopped light as a reference. The amplifier converts this signal to a wave with a specific frequency

and phase. The signal from the solar cell has also a frequency and a phase. An algorithm named Phase-sensitive detection is used to retrieve the measurement signal from the noisy signal. The result is a DC signal that is proportional to the measurement signal that we are interested. This is the main scope of the chopper, to produce a signal with a known frequency.

A typical EQE response spectrum is presented in figure 4.14(b). The ideal response would be the 100% brown square, however, the realistic response is the black curve. We observe that at low wavelengths the EQE response becomes zero. This is due to no photons can be absorbed for energies below the bandgap. The gap between the black curve and the brown square corresponds to losses, whether they are optical (reflection for example) or recombination, which is material related. In perovskites, the material absorbs in the range 400-800nm as we have seen. If the EQE is measured between a start wavelength λ_1 and an end wavelength λ_2, then the area under the EQE curve gives the J_{SC}:

$$J_{SC} = q \int_{\lambda_1}^{\lambda_2} EQE(\lambda) \cdot \Phi_{AM1.5G}(\lambda)\, d\lambda \tag{4.46}$$

,where $\Phi_{AM1.5G}$ is the photon flux in $s^{-1}\ cm^{-2}$ for the AM1.5G spectrum.The calculated J_{SC} from EQE and from the solar simulator should not differ more than 3-5% for a valid measurement.

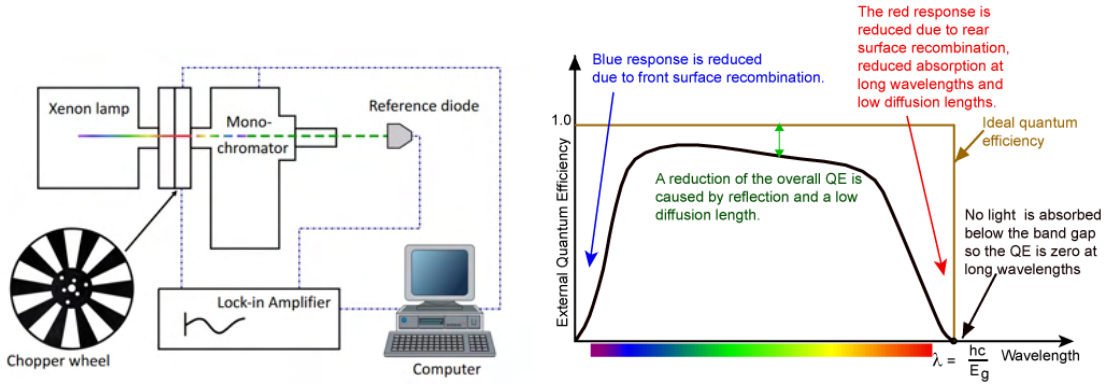

(a) EQE Experimental setup (b) An example of an EQE spectrum

FIGURE 4.14: a)EQE Experimental setup b)An example of an EQE spectrum [183, 184]

4.8 Dark IV Characteristics

The Space Charge Limited Current (SCLC) method is a very commonly used and simple technique if having the proper equipment. It is a steady-state method to estimate the electron or hole mobility in a variety of device architectures by applying a bias in non-illumination conditions. From the theory regarding the circuit model analyzed previously, we know that the dark IV curve is separated in various regions, as shown in figure 4.15(a) . At low biases, the current is dominated by shunt currents. The dark current can be described by the expression

$$J = J_{01} \exp\left(\frac{V - IR_S}{2(k_B T/q)}\right) + J_{02} \exp\left(\frac{V - IR_S}{(k_B T/q)}\right) + \frac{V - IR_S}{R_{SH}} \tag{4.47}$$

The first term is related to recombination in the depletion region with I_{01} being associated with the minority carrier lifetime which corresponds to ideality factor n=2, the second term is current related to diffusion and recombination in the neutral region, which corresponds to an ideality factor n=1. Finally, the third term is the shunt current. At low bias, the shunt current (third term) dominates. Increasing the bias leads to an exponential current described by the first 2 terms and at high bias, the current saturates and is governed by series resistance. Hence, from a dark IV curve, we can calculate both the series and shunt resistance and the ideality factor from the slope as

$$n = \frac{q}{k_B T}\left(\frac{\partial J}{\partial V}\right) \tag{4.48}$$

However, the main problem with this analysis is that at low bias or reverse bias, the shunt current does not exhibit a linear behavior with voltage and a SCLC mechanism has been proposed to explain the shunt behavior.

The formation of space charge is determined by the Debye Screening length, the length in which mobile carriers surrounding another charge with opposite polarity can remain bound without the thermal energy disordering the position of charges. Another factor is the dielectric relaxation time that determines the time it takes for a material to compensate for space charges created across the material. SCLC measurements are relied upon forming a Metal-Semiconductor contact that can be either Shottky (metal work function larger than the semiconductor's) or Ohmic (semiconductor work function is larger than the metal's). In both cases, electrons are injected from the material that possesses the lower work function, or the Fermi level at the highest position. In the case of Shottky contact, the barrier

is reduced when applying a forward bias, favoring the carrier injection. For hole transportation, it is favorable to choose a deep work function metal like Gold. On the opposite, a small work function metal like Al is preferred to help extraction or injection of electrons. To be able to measure the mobility of one charge carrier, charge blocking contacts are introduced to fabricate single-carrier devices. For example, for the case of the perovskite, the layer is sandwiched by 2 HTL materials to measure hole transport/injection and efficiently block electrons. If the mobility of a selective contact is to be measured, then the material is sandwiched between 2 ohmic contacts. The SCLC model is valid by the following assumptions: 1) The intrinsic carrier concentration is negligible when current is flowing, 2) Both contacts for injection/extraction are ohmic and 3) The material is defect-free and current is dominated by drift [185]. The Mott Gurney law has the following expression:

$$J_{SCLC} = \frac{9}{8}\mu\epsilon\frac{V^2}{d^3} \tag{4.49}$$

, where μ is the drift mobility, V is the applied voltage,ϵ is the dielectric of the material, and d is the thickness of the film. The derivation of this formula can be found in Appendix A. The form of the dark JV curve can be modified if traps are considered. In this case, a trap filling model is introduced, where the traps are filled depending on the voltage. This modification is due to the change in the electric field distribution due to the presence of traps.The current will rise abruptly at some point with voltage and will reach a point where the traps are filled. When the traps are filled, the IV characteristics are governed by the Mott-Gurney law [186, 187]. A typical Dark JV curve is shown in figure 4.15(b). The curve is divided into three regions: 1) The first region where current increases linearly with applied voltage, this is often called "Ohmic" region but is not ohmic in reality. 2) The second region where current increases abruptly with voltage, the trap filling region.3)The SCLC region, where current is not limited by traps. The transition from the linear to the trap filling region occurs at a voltage that is called Trap filling Voltage V_{TFL}, which gives the defect density N_d [188, 189]

$$N_d = \frac{2\epsilon\epsilon_0 V_{TFL}}{ed^2} \tag{4.50}$$

where V_{TFL} is the trap filling voltage, N_d is the defect density,ϵ_0 is the vacuum permittivity,ϵ is the material permittivity,d is the thickness of the material and e

is the elementary charge [190].In general, the current scales with voltage as

$$J \propto V^m \tag{4.51}$$

where m is an exponent that is calculated from the slope of the dark JV by plotting both current and voltage in a log-log plot:

$$m = \frac{dlogJ}{dlogV} \tag{4.52}$$

Hence, at m=1 we are at the linear region, at a value $m > 3$ we are at the trap filling region and at m=2 we are in the SCLC regime. Let's assume a_1,b_1 are the slope and the intercept of the linear region and a_2,b_2 are the slope and intercept of the trap filling region. If the current scales with voltage as

$$J = V^a \cdot 10^b \tag{4.53}$$

then, the trap filling voltage is given by:

$$V_{TFL} = 10^{\frac{b_2 - b_1}{a_1 - a2}} \tag{4.54}$$

For measuring the mobility of a HTL, a device configuration Contact/HTL/Contact is convinient. For measuring the defect density or the mobility of the perovskite film, a device architecture Contact/Charge Selective Contact/Perovskite/Charge Selective Contact/Contact is needed, to block one type of charge carrier. For hole-only devices, a Contact/HTL/Perovskite/HTL/Contact should be employed. The measurement is then performed by connecting those two device geometries with 2 probes or in a board and scanning at a voltage range, for instance from -0.2 to 2 volt or even more.For perovskites, typical mobilities are in the range of tenths up to hundrends of $cm^2V^{-1}s^{-1}$.The trap densities are on the order of $10^{15} - 10^{16}$ cm^{-3} for films and 10^{10} for single crystals.

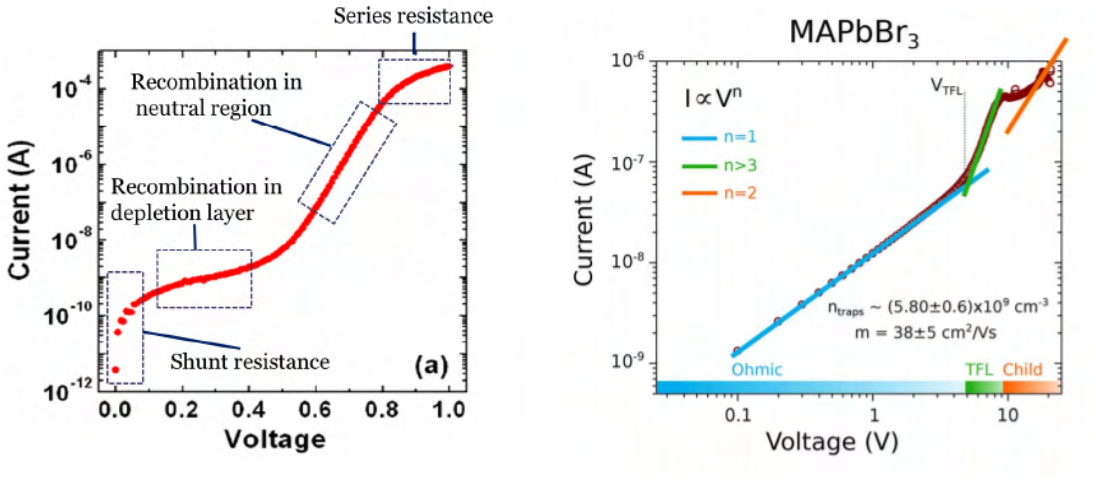

(a) (b)

FIGURE 4.15: a)Dark JV curve analysis using the equivalent solar cell circuit,b)Dark JV analysis using the SCLC model for $MAPbI_3$ single crystal [191, 192]

4.9 Transient Photovoltage-Photocurrent

The dynamics of charge generation and transfer are located in a timescale as shown in figure 4.16. Charge generation and transfer are on the order of fs to ns, carrier transport falls between ns and μs. Charge carrier recombination is mainly in the μs range and ion transport is the slowest process, on the order of s. A variety of techniques is used to study each process. Transient Absorption Spectroscopy (TAS) is used to study charge generation and transfer dynamics.Here, we will employ the transient optoelectronic techniques of Transient Photovoltage (TPV) and Transient Photocurrent (TPC) to study the charge recombination and extraction processes and investigate the interface dynamics of the interface that we are interested (e.g the HTL/Perovskite interface).

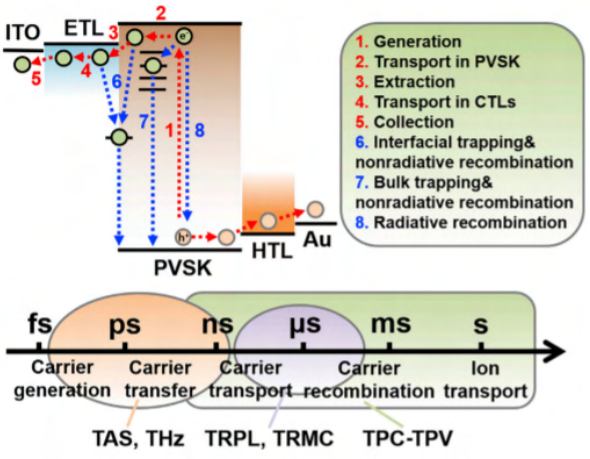

FIGURE 4.16: Timescale of charge carrier dynamics in PSCs [193]

4.9.1 Transient Photovoltage

TPV is an optoelectronic method to study charge carrier recombination.It has been employed in DSSCs, in OPV's and in PSCs.The device is held in an open circuit under a certain voltage under continuous illumination. The open circuit is achieved by connecting the device with a large resistor, typically 1MΩ. This results in no current flow in the device.The setup is shown in figure 4.17(a) [194]. The device is connected to an oscilloscope to record Voltage changes over time. When the V_{OC} of the device is stabilized, an extra laser pulse excites the device, which creates a small perturbation of the fermi level and hence of the V_{OC}. The voltage variation is proportional to the amount of extra-photogenerated carriers.

$$\frac{d\Delta V}{dt} \propto \frac{dn(t)}{dt} = -\delta R = \frac{-\delta n}{\tau_B} \tag{4.55}$$

where $n(t) = n_0 + \delta n$ is the charge density,n_0 is the steady state photogenerated carrier density and δn is the density of the extra photogenerated carriers produced by the laser pulse, and τ_B is the pseudo first order bulk recombination lifetime. The voltage then decays as

$$\Delta V(t) = \Delta V_0 \cdot \exp\left(\frac{-t}{\tau_B}\right) \tag{4.56}$$

As the device is in open circuit, the extra photogenerated charge carriers will eventually recombine, leading to an exponential decay of the voltage over time. In TPV, these decays can be measured for increasing pulse intensity.As the intensity increases, the V_{OC} increases and this leads to faster decays.TPV measurements

lead to mono-exponential decays.Because the V_{OC} depends on the steady state photogenerated carrier density,the recombination lifetime has also a depence on the V_{OC} as

$$\tau_B = \tau_0 \cdot \exp\left(\frac{-qV_{OC}}{vKT}\right) \tag{4.57}$$

,where τ_0 is a voltage independent pre-factor,and v is the slope parameter that depends on the order of steady state recombination dynamics. A typical TPV decay is presented in figure 4.17(b). By measuring the decays for various light intensities, a graph of the lifetime in log scale versus the voltage can be obtained.As the voltage increases, the lifetime drops linearly (figure 4.17(c) [194]).This graph can provide information about recombination dynamics. In instance, a steeper slope can lead to the unwanted situation of faster recombination dynamics. It is also interesting that for low voltages, the curve changes in shape and has a linear dependence with a different slope. The reason for this change is capacitive effects, which affect the interpretation of the measurements. It has been proposed that the total recombination time is the sum of the real recombination lifetime from the decay, plus a contribution from capacitance [195]:

$$\tau_{tot} = \tau_B + \frac{nkTC}{qJ_0} \cdot \exp\left(\frac{-qV_{OC}}{nKT}\right) \tag{4.58}$$

, where J_0 is the dark saturation current, n is the ideality factor and C is the capacitance of the active layer. Therefore, a more accurate value of the bulk lifetime can be obtained at high intensities, because carrier distributions in the active layer are homogeneous compared at low Voltages. This argument has been used to explain recombination orders higher than 2, including the presence of trap-assisted recombination.

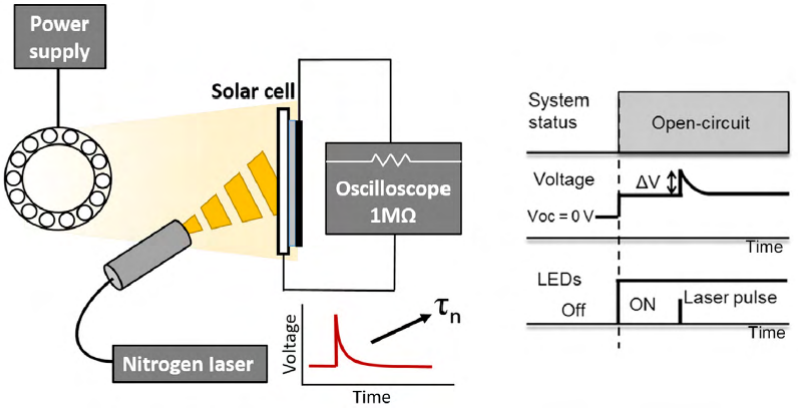

(a)

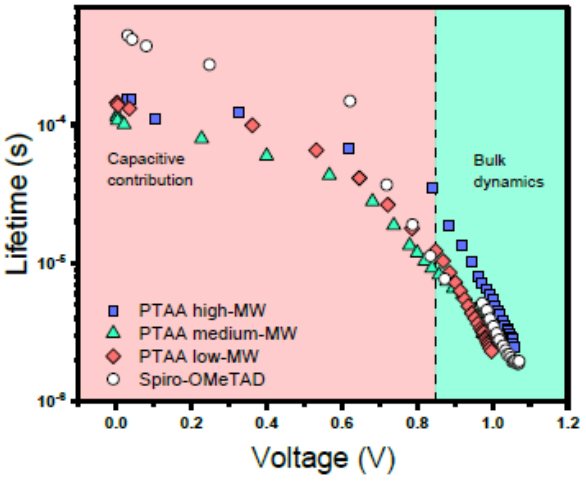

(b)

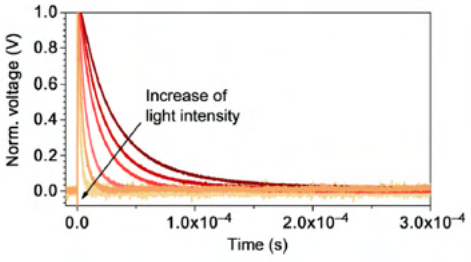

(c)

FIGURE 4.17: a)TPV experimental setup,b)TPV lifetime as a function of Voltage and c)TPV decays for various light intensities [194, 196]

4.9.2 Transient Photocurrent

The TPV method yields the lifetime by monitoring voltage as a function of time. However, the recombination dynamics depend on the charge carriers as well, hence

the lifetime has a dependence on charge carrier concentration. The TPC technique gives the charge carrier lifetime, this is why typically TPV and TPC are both employed to provide a uniform picture of the recombination dynamics. TPC also provides information for the charge extraction capabilities of the device.The experimental setup of TPC is shown in figure 4.18(a). It is almost the same setup with TPV, with the difference now being that the device must be kept under short circuit conditions, therefore the device is connected to a small resistor, typically 50 Ω. The device is constantly illuminated with a light source, usually a laser, and then a laser pulse excites the device. The oscilloscope monitors again the voltage decay, which can be easily converted to current by using Ohm's law. The only limitation in this method is that carrier losses at a short circuit must be negligible, hence charge collection and charge recombination should not be comparable. In TPC measurements, as the light intensity increases, the current increases, and the extracted charge also increases linearly. Again, the decay of the current to time is a mono-exponential process. By integrating the area under the Current-Time graph, we can obtain the amount of photo-generated charges induced by the pulse that was generated and extracted. We can convert charge to charge density through the formula

$$n = \frac{Q}{e \cdot d} = \frac{\int_0^t J(t)\, dt}{e \cdot d} \tag{4.59}$$

,where $Q = \int_0^t J(t)\, dt$ is the extracted charge, d is the active layer thickness and e is the elementary charge.The TPC method can provide information about charge densities and charge accumulation in the large perturbation regime, meaning we use a large duty cycle. Increasing the duty cycle increases the period where the laser pulse illuminates and creates the photo-generated carriers (duty cycle of 0.1-0.9). At small perturbation, we can get an estimation of the diffusion coefficient (duty cycle < 0.1).By plotting the extracted charge as a function of current (figure 4.18(b)), we can obtain information for charge extraction. A higher amount of extracted charges corresponds to improved charge transport and collection. This is useful when comparing different charge selective contacts. The whole puzzle about charge carrier dynamics is obtained by plotting the carrier lifetime from TPV as a function of the charge density from TPC at the same voltage, as shown in figure 4.18(c). We should also keep in mind that as in the case of TPV, there is also a capacitive contribution at low intensities/Voltages(Current densities).

Furthermore,the extracted charge density under open-circuit varies with V_{OC} as

$$n = n_0 \cdot \exp\left(\frac{qV_{OC}}{mkT}\right) \tag{4.60}$$

, where n_0 is a prefactor and m is the recombination order.

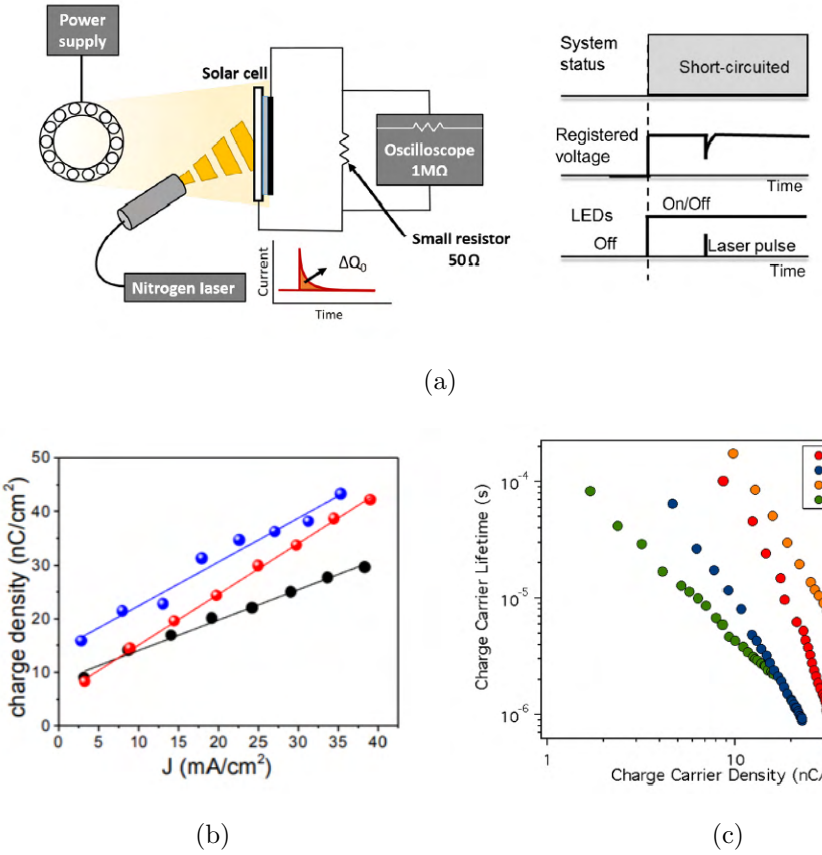

(a)

(b)

(c)

FIGURE 4.18: a)TPC experimental setup,b)TPC Extracted charge as a function of Current Density,c) Carrier lifetime from TPV as a function of carrier density from TPC. [194, 197, 198]

4.10 Spin coating

Spin coating is an experimental technique for the formation of thin films with thicknesses ranging from few nm to few μm that is spread uniformly throughout the sample. The film is formed by casting an ink or a solution in a substrate before starting the spinning (static spin coating) or while the substrate is spinning (dynamic spin coating). The high rotational speed ensures a large enough centripetal force, which in combination with the surface tension of the solution ensures an even covering of the substrate (figure 4.19(a)). Initially, the solution is cast on the

substrate by using a pipette. The spin coater might have an acceleration time, where it reaches the maximum desired rpm. At this stage, most of the solution is expelled from the substrate. The fluid will become level when the drag is canceled out by rotational accelerations. Now the fluid begins to turning thin because it is dominated by viscous forces. At this stage, the color of the film might change due to interference effects. When the color change stops, the film is dry. The formation of the thin film depends on the evaporation rate of the solvent used. Parameters such as solvent volatility, vapor pressure, and ambient conditions such as relative humidity. The thickness d of the obtained film depends on the rpm chosen and depends inversely on the square root of the rotational speed as

$$d \propto \frac{1}{\sqrt{\omega}} \tag{4.61}$$

For most solvents, a 30 seconds spin coating is enough to evaporate the solvent. The thickness of the thin film also depends on the concentration used and the spinning time. As large concentrations are used, the obtained film thickness will be larger as well. The coverage of the substrate depends on the wetting properties of the solution and the ink. A material with a high surface tension wants to "ball-up", to not spread, compared to materials with low surface tension. Other problems that might arise in the resulted thin film are the formation of cracks, pinholes, comet streaks or aggregates, (figure 4.19(b)) that prevent the formation of a uniform film. It is crucial to have as clean substrates as possible. Cleaning protocols along with a UV-Ozone treatment can keep the substrates free of dust, streaks, and organic contaminants. Other possible origins of these problems include insufficient spinning speed (too high or too low), the solution not spread on the middle of the substrate, too high acceleration, liquid waits too long before starting of the spinning, or insufficient dispensed volume or volume that contains bubbles. The spin coating offers the advantage of producing thin films with low cost and oftentimes without further processing like thermal annealing. It can process batches of substrates individually, with high solvent drying rates. The main limitation of spin coating is the size of the substrate used, meaning that it cannot be employed for industrial applications but mostly in academic/research environments. Furthermore, spin coating is often applied in complex environments such as gloveboxes, where the conditions must be carefully controlled to ensure reproducible results.

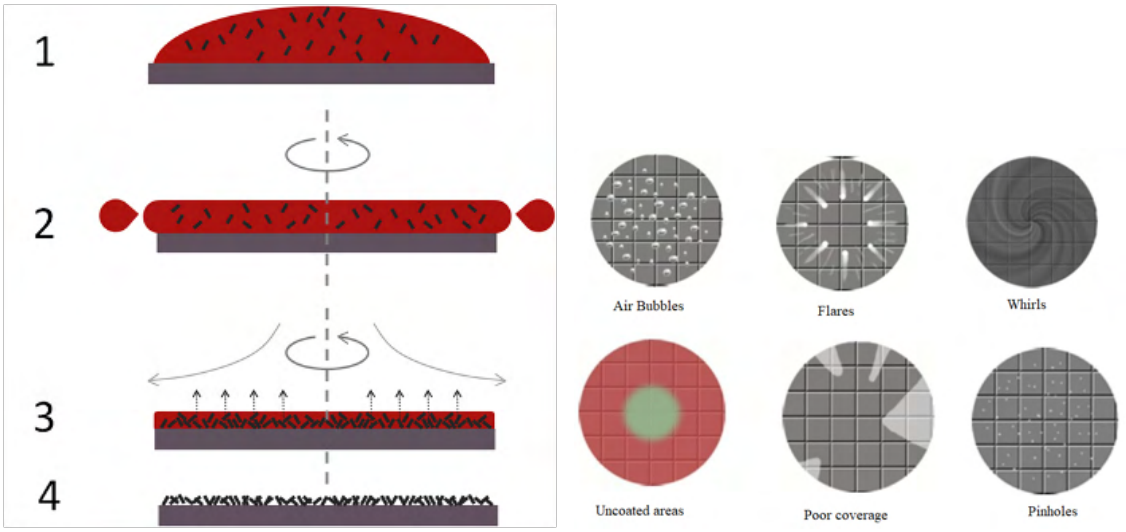

(a) (b)

FIGURE 4.19: a) Spin coating and thin film formation,b)Common issues with spin coated thin films [199, 200]

4.11 Thermal Evaporation

Thermal evaporation is a thin film deposition method. In this method, the thickness of the film can be controlled with high precision. The setup of a thermal evaporator is shown in figure 4.20. The evaporator is connected with a high vacuum pump (typically, a turbine pump). The high vacuum ensures that the evaporated molecules of the substance of interest have a long mean free path and will deposit on the desired substrate without interacting with any other type of vapors as the atmosphere is pumped. The element/substance that will be evaporated is placed in a resistive boat. The boat is connected with a filament that is heated in high temperatures after the application of high potential. The boat is in turn heated and the desired material evaporates, gets deposited on the substrate, and eventually condenses. The desired film thickness is achieved by monitoring the process with a coupled electronic monitor. The monitor is connected with a crystal quartz sensor placed in the proper position inside the chamber. The sensor has a finite lifetime and must be replaced in sufficient periods. The damage to the sensor can be realized through the thickness monitor system. The substrate-boat and sensor distance are also important to optimize and control the deposition. The tooling factor and z factor are also considered to obtain a precise thickness value. Z-factor is used to match the acoustic properties of the material being deposited to the acoustic properties of the base quartz material of the sensor crystal. The Z

factor can be obtained empirically. The tooling factor is the ratio between the film thickness, measured by the profilometer on the substrate to the thickness measured by the crystal monitor. If you used an initial value for the tooling factor then you need to multiply that ratio by the initial tooling factor.

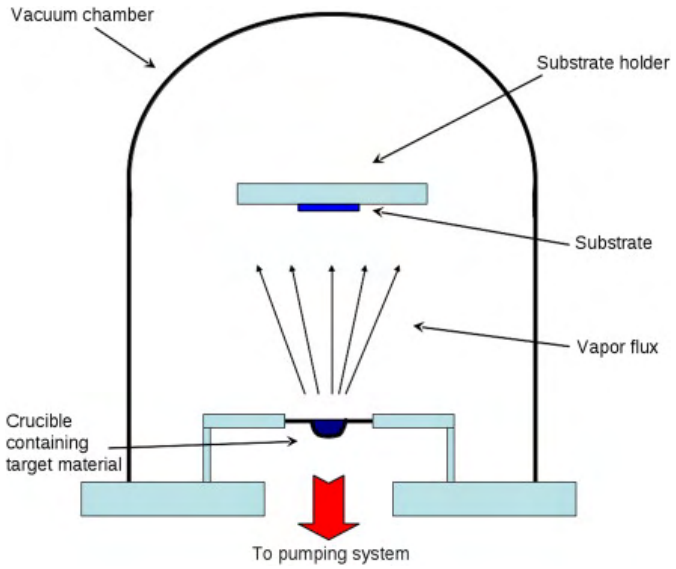

FIGURE 4.20: Setup of a Thermal Evaporator system [201]

Chapter 5

Experimental Methods and Results

5.1 Motivation

Among parameters that have been analyzed previously, the main advantages of inverted PSCs are are the easy, low-temperature fabrication [202] that is preferable for fabricating large-area modules, negligible hysteresis [203] and their applications in tandem devices [130]. Among the many device parameters [39],PCE improvement largely relies on the optimization of the hole transport layer HTL-perovskite interface. This is achieved through energy level alignment and efficient charge extraction and transport [204], where a preferable band alignment is associated with higher open-circuit voltage [205]. Moreover, the perovskite film growth and crystallinity largely depend on the bottom layers [110].The most common HTLs in Inverted PSCs include (PEDOT:PSS),PTAA, Nickel Oxide and copper-based inorganic materials [206].PEDOT:PSS is a widely used HTL in inverted devices [114],because it possesses many benefits such as low-cost production, mechanical flexibility for large substrates and transparency in visible wavelengths [207]. Nevertheless, PEDOT-based devices suffer from open-circuit voltagesV_{OC}<1V due to its low work function (WF) and energy level mismatch [66].In addition, the insulating PSS^{-1} ionomer stands as a limiting factor for film conductivity [208], while its acidic and hygroscopic nature induces rapid attenuation in device stability [209]. Despite its wide use, pristine PEDOT:PSS is not a very efficient HTL, therefore various methods are being applied in order to enhance its PCE, such as incorporation of inorganic salts [210–212] ,pH [213] & and solvent treatment [214],that lead to remarkable efficiency enhancements.On the other hand, inverted devices with

PTAA as HTL are obtaining efficiencies of more than 20%, which is comparable to normal devices with Spiro-MeOTAD as HTL [78].The major drawback of using PTAA is the high cost and inadequacy for use in large-area devices. Recently, Al-Ashouri et al. have introduced two novels, low-cost, self-assembled monolayers as hole selective contacts to achieve high PCEs with the ability to use in large-area devices and replace PTAA [215]. Many efforts are focused on the synthesis of novel materials, to replace PEDOT:PSS. Cao et al. have synthesized an organic conjugated molecule that improved the PCE of PEDOT: PSS devices by 1% [216]. Likewise, Liu et al. synthesized 2 conjugated polyelectrolytes that enhanced the PCE up to 17.71%, compared to PEDOT:PSS [44]. Improving the operational stability of PSCs is a major step in establishing their commercial use. To surpass the international standards for operational stability [217], all the parameters affecting the PSCs device stability such as moisture, oxygen, heat, light exposure, and intrinsic instability must be tackled [218]. The chemical interaction between the hole selective contact and the perovskite film has a direct impact on the stability of p-i-n devices [147]. The sulfonic acid groups in PEDOT:PSS are corroding the ITO electrode, which has detrimental consequences on the device stability [219, 220] , while the hydrophilic nature of PEDOT:PSS can cause humidity accumulation in the perovskite film, resulting in rapid device degradation. Ma et. al have incorporated hydrophobic Nafion into PEDOT:PSS, leading to improved film conductivity,V_{OC} and stability [221]. Singh Mann et. al also enhanced the PCE to 16% and stability of p-i-n devices by spin coating a Sulfonic acid-functionalized Graphene Oxide (SrGO) buffer layer between PEDOT:PSS and the perovskite film [222] . In this thesis, we present a novel, hydrophobic, low synthetic complexity and low temperature-solution processable D-A conjugated polymer consisting of an indacenodithiophene derivative as the electron-donating and a thiadiazolequinoxaline derivative as the electron-withdrawing unit PIDTTDQ which is employed in inverted device architecture, replacing PEDOT:PSS as the HTL. We demonstrate that PIDTTDQ, when spin coated on ITO substrates, it provides a transparent film at visible wavelengths, and shows hydrophobic behavior.

5.2 Materials and Solvents used

Lead Iodide (PbI_2) (99.99%) was purchased from TCI. Lead Bromide ($PbBr_2$) (98+%), Cesium Iodide (CsI) (99.999%) and Rubidium Iodide (RbI) (99.8%) were purchased from Alfa Aesar. Formamidinium Iodide (FAI) was purchased from

GreatCell. Methylammonium Bromide (MABr) was purchased from Dyesol. PTAA was purchased from Solaris.$PC_{60}BM$ (99.9%) was purchased from Solenne. 2,9-Dimethyl-4,7-diphenyl-1,10-phenanthroline-Bathocuproine (BCP),Toluene (99.8%, Anhydrous),DMF (99.8%, Anhydrous), DMSO (>99.9%, Anhydrous),Chlorobenzene (99.8%,Anhydrous) and Tetrabutylammonium Hexafluorophosphate (NBu_4NPF_6) were purchased from Sigma Aldrich. 2-Propanol (IPA) (99.5%, extra dry) and Acetonitrile (99.9+%, Extra Dry) were purchased from Acros Organics. PEDOT:PSS (aqueous dispersion) was purchased from Clevios.

5.3 Synthesis of PIDTTDQ

All reactions are air and light-sensitive and, therefore, were performed under argon and in the dark. All glassware was washed using detergent (Teepol), rinsed with excess water, acetone, and methylene dichloride, and dried in an oven at 120 °. All solvents and reagents were purchased from Sigma Aldrich. Toluene was distilled using calcium hydride (CaH_2) and benzophenone before polymerization. The thiadiazoloquinoxaline derivative was purchased from Sunatech Inc. The syntheses of the indacenodithiophene were performed according to the already published procedure.[223] The experimental condition for the polymerization is analytically described below: Distannyl substituted indacenodithiophene (0.5 mmol) and dibromo thiadiazoloquinoxaline derivative (0.5 mmol) were dissolved in dry toluene (0.025 M). Then, tris(dibenzylideneacetone)dipalladium(0) (Pd_2dba_3) (0.02 equiv) and tri(o-tolyl)phosphine ($P(o-tol)_3$) (0.04 equiv) were added and the reaction mixture was stirred at 120°C under argon atmosphere for 48 h.The polymer was purified by precipitation in methanol, filtered, and washed using a Soxhlet apparatus with methanol, acetone, hexane, and chloroform. The chloroform fraction was evaporated under reduced pressure and the polymer was precipitated in methanol, filtered through a 0.45 mm PTFE filter, and finally dried under a high vacuum, rendering a dark greenish solid. The yield of PIDTTDQ was 86%. The chemical structure of the synthesized PIDTTDQ is shown in figure 5.1.

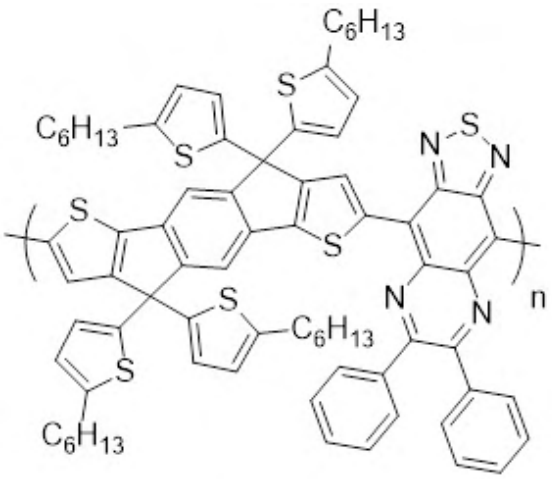

FIGURE 5.1: Chemical structure of the PIDTTDQ molecule.

5.4 Device Fabrication

All device fabrication was performed under a N_2 filled Glovebox by MBRAUN. The only exception was the deposition of PEDOT:PSS films that was conducted in an ambient air spin coater. The glovebox is constantly filled with high purity N_2 gas (purity 99.99999 %).The atmosphere is kept with a low O_2 and H_2O,with contents lower than 100 and 0.1 Parts Per Million (ppm).

5.4.1 Substrate preparation and Anode

As seen in section 4.10, the substrates should be as clean as possible to produce uniform films and avoid short circuits in the final device. In this thesis, the glass/ITO anode 8-pixel (can measure up to 8 cells) substrates from Ossila have been used. The substrates were cleaned by Ultrasonication in a HellmaneX sonicator. The substrates were placed in a substrate rack provided by Osilla in a 1000ml beaker. Then substrates were cleaned by sequential ultrasonication in soap, deionized water, Acetone, and IPA, each step for 10 minutes. Then, the substrates were dried in an oven for 30 minutes, following a UV-Ozone treatment for 15 minutes to remove contaminants and improve surface wetting.

5.4.2 Hole Transport Layer

The PEDOT:PSS aqueous dispersion from Clevios was filtered with a 0.45 μm filter before deposition. $\approx$ 70 μl were dispensed on the substrates, following a spin

coating at 7000rpm for 45s. The samples were then annealed in a hotplate at 120 ° for 20 minutes. The as-prepared films were immediately transferred to the glovebox for further processing. The obtained thickness of PEDOT:PSS is ≈ 50nm.

Regarding PIDTTDQ, a stock solution with a concentration of 0.5 mg ml^{-1} in Chlorobenzene was prepared.We noticed that higher concentrations are too high and produce films with reduced transparency. This stock solution was used to prepare films tested for the thickness optimization of the PIDTTDQ thin-film devices. For PIDTTDQ thin film deposition,60μl were statically dispensed, following a spin coating at 4000 rpm for 45s, without any further annealing. We observed that thermal annealing does not improve the PCE as we will see.

For devices using PTAA for stability test, a 2 mg ml^{-1} solution in Toluene was prepared. 60 μl of the solution were statically spin coated at 6000rpm for 30s, following annealing at 100° for 10 minutes. The obtained thickness of PTAA was ≈ 5-10nm.

5.4.3 Perovskite Deposition

For the perovskite solution a 4-cation perovskite was employed, involving the Cs,Rb,FA and MA cations.For the preparation of the solution,a 1.5M solution was prepared by mixing in stoichiometric ratios PbI_2,$PbBr_2$,FAI,MABr,CsI and RbI.The solution preparation was similar to the recipe described by Saliba et. al [84]. According to this protocol, stoichiometric amounts of PbI_2,$PbBr_2$,FAI,MABr precursors are weighted in a vial, following the addition of a proper amount of DMF:DMSO 4:1 to obtain an 1.5M concentration of the MAFA solution.More specifically,1.24M PbI_2 (9% excess),1.14M FAI, 0.2M $PbBr_2$ and 0.2M MABr were weighted.In addition, 1.5M of CsI and RbI stock solutions were prepared by weighting the proper amounts and adding DMF and DMF:DMSO 4:1,respectively.The solutions are then heated at 150° to assist dissolving.The solutions are heated prior to each use.After the dissolution of the MAFA perovskite,5vol% CsI and 4 vol% RbI are added to the MAFA perovskite, yielding the RbCsMAFA perovskite.The solution is then left stirring continuously in a vortex in the glovebox.The obtained perovskite has the stoichiometric formula $Rb_{0.04}Cs_{0.05}(FA_{0.85}MA_{0.15})_{0.91}Pb(I_{0.85}Br_{0.15})_3$.For perovskite deposition, 45μl of the solution were spin coated at 6000rpm for 45s. 200μl Chlorobenzene anti-solvent were dropped 20s before the end of the spinning process. The samples were then annealed at 100°C for 45minutes.The obtained thickness is ≈ 450-500nm.

5.4.4 Electron Transport Layer

For the ETL,a 20 mg ml^{-1} $PC_{60}BM$ solution in Chlorobenzene was prepared.The solution is left stirring magnetically at mild heating (70 °C) continuously. For film deposition,45 μl of the solution was spin coated statically at 2000rpm for 60s, leading to a thickness of ≈ 30-40nm. The samples are then left in a petri dish to dry for 30 minutes

5.4.5 BCP Interlayer

For the deposition of the BCP interlayer,a stock solution with a concentration of 0.5 mg ml^{-1} in IPA was prepared. For film deposition, 45 μl of the solution were dynamically spin coated at 4000rpm for 45s. The samples are then etched with a scalpel to expose the ITO and complete the circuit.

5.4.6 Cathode Deposition

Ag was used as a cathode.The deposition was performed in an MBRAUN system. The turbine vacuum pumps the chamber until it reaches a pressure of $4{\cdot}10^{-6}$ mbar.A silver pellet (from Kurt J.Lesker) was added to the boat before the evacuation of the chamber.Then,100nm were deposited in an evaporation rate of 1.2-1.4 $\AA\ s^{-1}$

5.5 Characterization of PIDTTDQ

Instrumentation: Gel permeation Chromatography (GPC):Average molecular weights per number and polydispersity indices were determined with GPC at 80°C on a Shimadzu liquid Chromatograph (LC-20AD) system consisting of a DGU-20A5R degassing unit,a SIL-20AC HT autosampler, a CTO-20AC column oven,a SPD-20AV UV-Vis detector connected in series.The system contains a PL-GEL 10μm guard column, two PL-GEL 10μm Mixed-B columns, and Chlorobenzene as the eluent. The instrument was calibrated with narrow polystyrene standards with M_p ranging from 4730 g/mol to 3187000 g/mol.

Nuclear Magnetic Resonance (NMR): 1H-NMR measurements were carried out in solutions (1% w/v) of the copolymers using $CDCl_3$ (Acros 99.6%) as the solvent and tetramethylsilane (TMS) as the integral standard on a Varian 600 MHz NMR spectrometer at ambient temperature.

UV-Vis absorption of the polymer solutions (concentration 10^{-5} M) and the fabricated films was recorded with a Shimadzu 1900 spectrometer.The **UV-Vis**

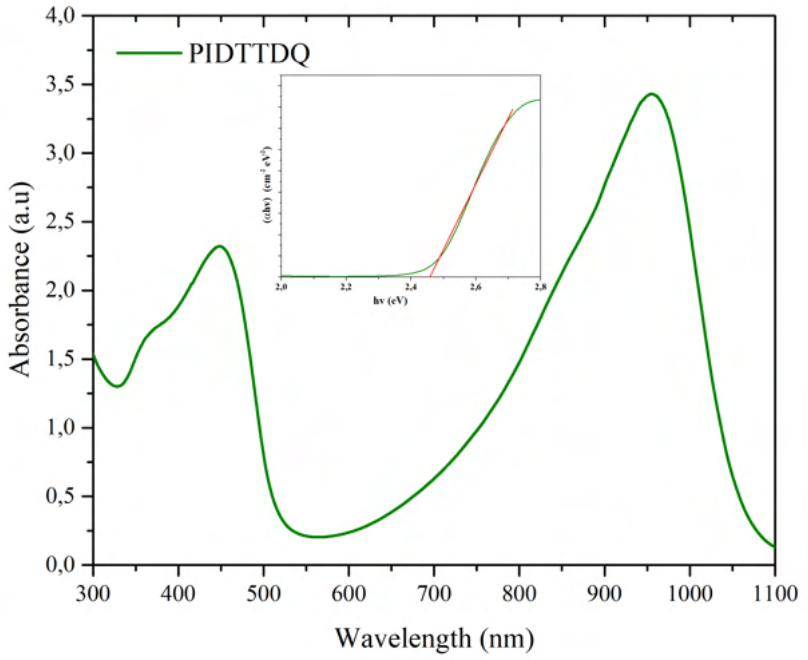

FIGURE 5.2: UV-Vis spectrum with tauc plot

spectrum of PIDTTDQ is shown in figure 5.2. PIDTTDQ shows two absorption peaks, one in the visible and one in the IR range. A tauc plot is also shown by the same graph, for a film thickness of ≈ 50nm. The PIDTTDQ conjugated polymer is a direct semiconductor, and the calculated bandgap is estimated at 2.46 eV.

. The NMR spectrum is shown in figure X. From the graph, the following peaks are observed: In addition to Absorbance measurements, Transmittance measurements were also carried out in PIDTTDQ and PEDOT:PSS thin films. The thickness of both films was fixed at ≈ 50nm. The measurements were performed in glass/ITO substrates.A thickness of 50nm corresponds to a PIDTTDQ concentration of 4 mg ml^{-1}.The transmittance spectra of both materials are shown in figure 5.3. It is evident from the graph that PIDTTDQ is more transparent in visible wavelengths. This is an important result, as it has the potential to reduce optical losses in the device.In Inverted PSCs, light enters from the HTL side,therefore the HTL should be as transparent as possible.

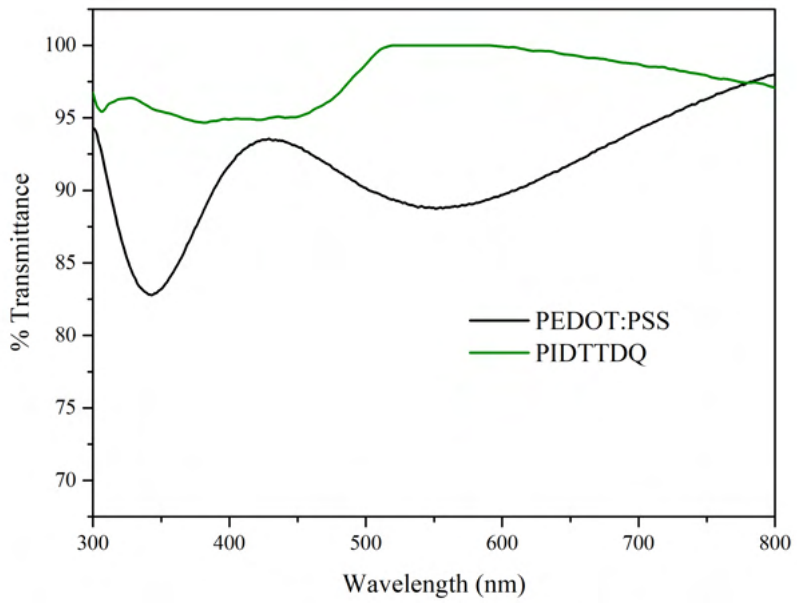

FIGURE 5.3: UV-Vis spectrum with tauc plot

CV curves were obtained with a Potentiostat from Ossila in a three-electrode system. Non-aqueous Ag/Ag^+ was used as the reference electrode. A platinum wire was used for the counter electrode. The working electrode used was a platinum disk. Ferrocene/ferrocenium (Fc/Fc^+) was used as reference. The electrolyte solution was composed of sufficient amounts of acetonitrile and 0.1M of NBu_4NPF_6. The CV curves were obtained by scanning at a scan rate of 100 mV s^{-1}. A small amount of PIDTTDQ was evaporated on the working electrode in order to be measured.The CV curve of PIDTTDQ is presented in figure 5.4. There is an oxidation peak on the right side of the graph. As seen previously, in order to calculate the onset oxidation potential E_{OX}, equation 4.11 is used. The equations of the 2 straight lines, the one on the left and the second at the oxidation peak are the following:

$$I_1 = (7.76633 \cdot V - 2.94996) \cdot 10^{-7}, I_2 = (4.44235 \cdot V - 3.02711) \cdot 10^{-6} \quad (5.1)$$

by finding the point of intersection between these two lines, we obtain the onset oxidation potential.This yields a value of E_{OX}=0.74V.If we plug this result into equation 4.11,we get a HOMO value of -5.14eV for the case of PIDTTDQ.Furthermore,by the Uv-Vis absorption measurement, we have found an optical bandgap value of

E_g=2.46 eV.By using the equation

$$E_{LUMO} = E_{HOMO} + E_g \tag{5.2}$$

We obtain a E_{LUMO} of -2.68eV.The energy levels of the PIDTTDQ are summarized in Table 5.1.

TABLE 5.1: Values of energy levels of PIDTTDQ obtained from CV and UV-Vis measurements

Parameter	**Value (eV)**
E_{HOMO}	-5.14
E_{LUMO}	-2.68
E_g	2.46

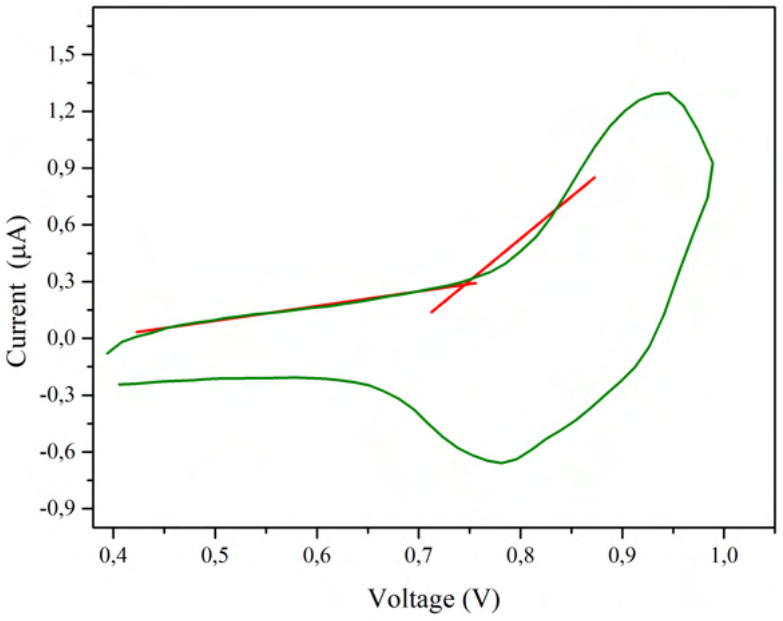

FIGURE 5.4: CV Voltammogram of PIDTTDQ with Onset Oxidation Potential calculation

5.6 Mobility of PIDTTDQ and PEDOT:PSS films

The mobility of PIDTTDQ was calculated by fabricating hole-only devices.The devices had the structure ITO/PIDTTDQ/PTAA/Au.The thickness of PIDTTDQ was fixed at ≈ 50nm in a 4mg ml^{-1} concentration to ensure a proper measurement.The thickness of PTAA was also ≈ 80-100nm by spin coating a 10mg ml^{-1}

solution in Toluene at 4000rpm for 30s.100nm thick Au was evaporated as the back contact.The deeper work function of Au is used to enhance hole injection/extraction.The dark JV characteristics of the hole-only devices were measured in a commercial apparatus (Cicci Research), by scanning from -0.2 to 2V, with a scan rate of 300mV s^{-1}.For PEDOT:PSS, hole-only devices were fabricated with the structure ITO/PEDOT:PSS/PTAA/Au.The thickness of PEDOT:PSS was fixed at 50nm. The dark JV characteristics for both device geometries are shown in figure 5.5. The graph is $J^{1/2}$ as a function of Voltage. According to the Mott-Gurney law,this yields a straight line as it is evident from the graph. By using the Mott-Gurney law, the slope a of the graph will be equal to:

$$a = \frac{9\mu\epsilon}{8d^3} \Longrightarrow \mu = \frac{8ad^3}{9\epsilon} \tag{5.3}$$

,where d=50nm is the thickness of either PIDTTDQ or PEDOT:PSS, and $\epsilon \approx 3$ is the dielectric constant for a typical organic semiconductor [224].We expect that higher slope seen in the graph will yield a higher mobility for PIDTTDQ.This is confirmed, as the obtained mobilities of PIDTTDQ and PEDOT:PSS were $3.03 \cdot 10^{-4}$ and $1.42 \cdot 10^{-4}$ $cm^2V^{-1}s^{-1}$,respectively (values summarized in 5.2).We conclude that the mobility of PIDTTDQ is higher than that of PEDOT:PSS,hence we expect improved hole transport for the case of PIDTTDQ [225].

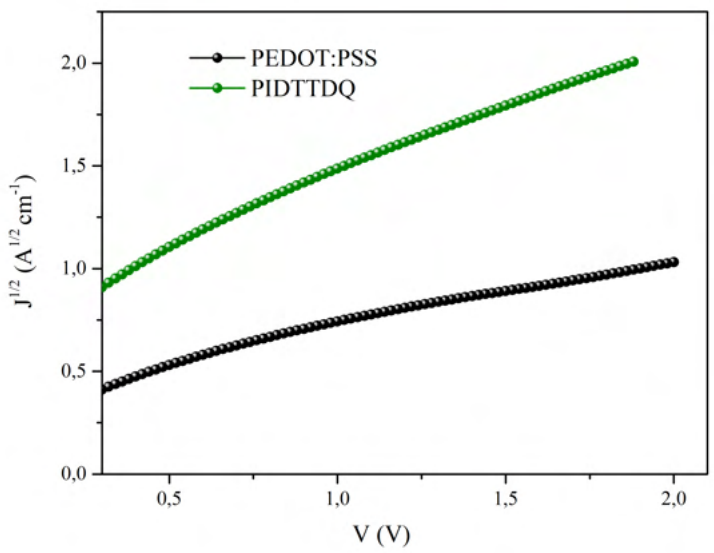

FIGURE 5.5: Square root of Current as a function of voltage according to the Mott-Gurney Law.

TABLE 5.2: Table with mobility values of PEDOT:PSS and PIDTTDQ

Material	**Mobility** $(cm^2V^{-1}s^{-1})$
PEDOT:PSS	$1.42 \cdot 10^{-4}$
PIDTTDQ	$3.03 \cdot 10^{-4}$

5.7 Morphological Properties

The morphological properties of PIDTTDQ and PEDOT:PSS were investigated by AFM measurements.AFM images were captured using an XE7 microscope (Park Systems) by operating in tapping mode.The obtained AFM images of 5x5μm resolution of PIDTTDQ and PEDOT:PSS films on Glass/ITO with a thickness of 50nm are shown in figure 5.6. No obvious differences were observed between the two films. The Root Mean Square (RMS) roughness of the PIDTTDQ and PEDOT:PSS films was 2.3 and 1.6nm, respectively.This indicates that both materials produce uniform films with small height deviations.

The morphological properties of PIDTTDQ and PEDOT:PSS were also investigate by studying the growth of the perovskite above them, as the bottom substrate plays a vital role and severely affects the growth of the perovskite layer.The AFM images were captured in a Glass/ITO/HTL/Perovskite geometry.The calculated RMS roughness on the perovskite coated in PIDTTDQ and PEDOT:PSS was 14.1 and 16.2nm, respectively.This indicates that PIDTTDQ can produce more uniform perovskite films than PEDOT:PSS, therefore it has the potential to produce films with a smaller number of defects.

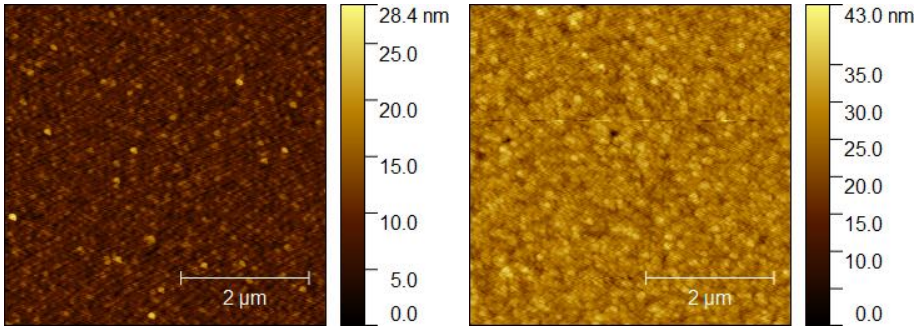

(a) (b)

FIGURE 5.6: a)5x5μm image size of PIDTTDQ film on glass/ITO b)5x5μm image size of PEDOT:PSS film on glass/ITO.

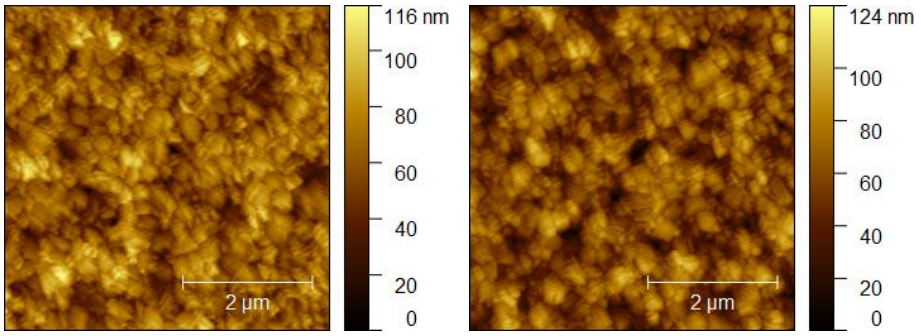

(a) (b)

FIGURE 5.7: a)5x5μm image size of Perovskite film on PIDTTDQ b)5x5μm image size of Perovskite film on PEDOT:PSS.

5.8 Wetting properties of PIDTTDQ

In this section, we will study the wetting properties of PIDTTDQ.PEDOT:PSS is a hydrophilic material, therefore we expect good wetting properties. We will also study the wetting properties of PTAA that will be used for the stability test. The wetting properties of all materials are investigated through water Contact Angle measurements. Water Contact angle measurements were performed on an L2004A1 goniometer from Ossila, by pipetting water droplets on the surface of Glass/ITO/HTL substrates, where HTL is any of the 3 materials.The Contact angle measurements of PEDOT:PSS,PIDTTDQ and PTAA are shown in figure 5.8(a),5.8(b) and 5.8(c) respectively. The contact angle of PEDOT:PSS was 26.2°,while the one of PIDTTDQ was 96.0° and 83.7 ° for the case of PTAA.The concentrations of both PIDTTDQ and PTAA were kept at 2 mg ml^{-1} in order to have a common measure of comparison. The highest contact angle of PIDTTDQ indicates the potential for the material to have a strong humidity tolerance and prevent the penetration of humidity in the device, resulting in improved operational stability. This contact angle is even higher than that of PTAA, which is also a hydrophobic material.

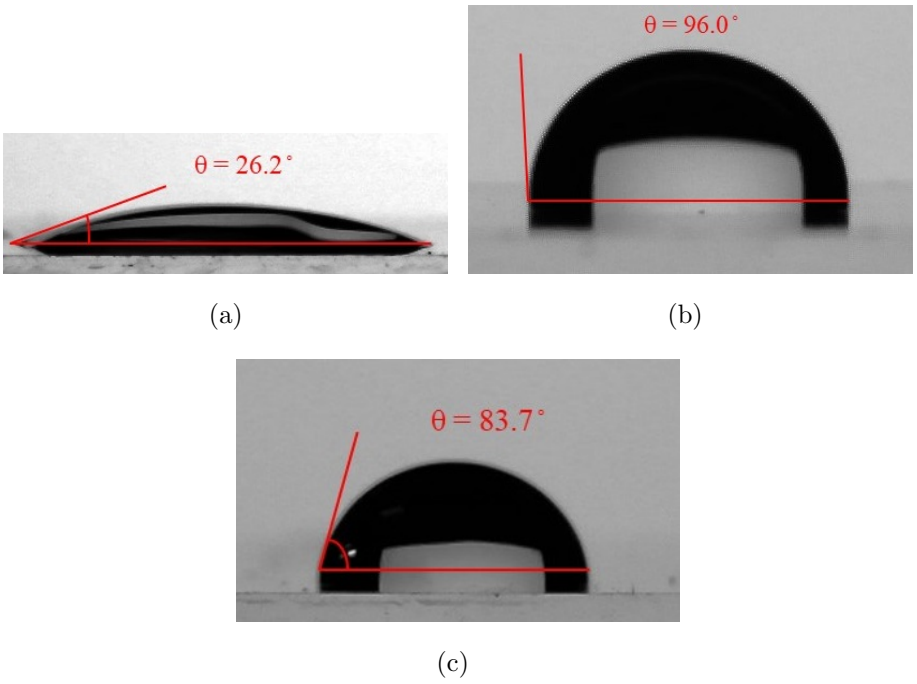

(a) (b)

(c)

FIGURE 5.8: a)Contact angle measurement of PEDOT:PSS.b)Contact angle measurement of PIDTTDQ and c)Contact angle measurement of PTAA

5.9 Optimization of PIDTTDQ

After completing characterizations regarding the PIDTTDQ material, we studied the growth of the perovskite layer on PIDTTDQ by fabricating complete devices. We noticed from absorbance/transmittance measurements that high concentrations led to very thick films with reduced transmittance, which could limit the device performance due to large optical losses.Transmittance measurements for the concentrations of 0.5,1,2 and 4 mg ml^{-1} are shown in figure 5.9.It is evident that the Transmittance reduces as the concentration increases and so does the film thickness. We started the optimization of PIDTTDQ from a reference concentration of 4 mg ml^{-1}, as this concentration led to $\approx$ 50nm thick thin films. However, due to the hydrophobic nature of the material, the perovskite deposition on top of PIDTTDQ was not possible due to the non-wetting properties and the high surface tension. Further reducing the concentration to 2 and 1 mg ml^{-1} did not resolve the issue either. Further reducing the tested concentrations, we have found that a concentration of 0.75 mg ml^{-1} is the threshold concentration where a black dense perovskite film with a good surface coverage can be obtained. Another attempt to address the hydrophobicity issue was to decrease the surface tension of the film, by treating the surface with DMF. Hence, we spin coated 100μl prior to

perovskite deposition. This attempt did not solve the problem, producing films with poor coverage at high concentrations. Another attempt to resolve the wetting problem was to treat the PIDTTDQ film with UV-Ozone for a short period of time ≈ 3-5minutes.The treatment allowed the formation of the perovskite film but degraded the material, resulting in PCEs of 2-3%. The device statistics for UV and no UV treated PIDTTDQ films are provided in figure 5.10. These devices correspond to a non-optimized 0.2mg ml^{-1} concentration.

Thermal annealing is another parameter that was studied for the optimization of the PIDTTDQ devices. Annealing temperatures of 60°,100° and 150° and without annealing were tested. The tests were performed for a concentration of 0.2 mg ml^{-1}. The photovoltaic parameters for each case are shown in the box plots in figure 5.11. We have also observed that annealing temperatures up to 200° can produce functional devices but with inferior PCEs. We observe from figure 5.11 that the average values of all 4 parameters for 11 devices are higher for the case of no annealing. This leads to the conclusion that the PIDTTDQ film can be processed in ambient temperatures, making PIDTTDQ more suitable for large-area devices and commercial use.

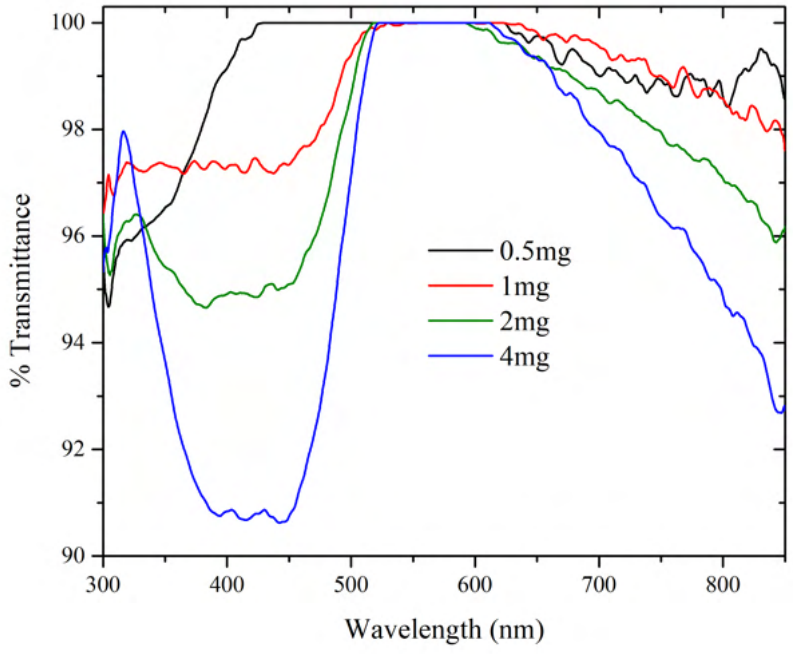

FIGURE 5.9: Transmittance spectra of various concentrations of PIDTTDQ.

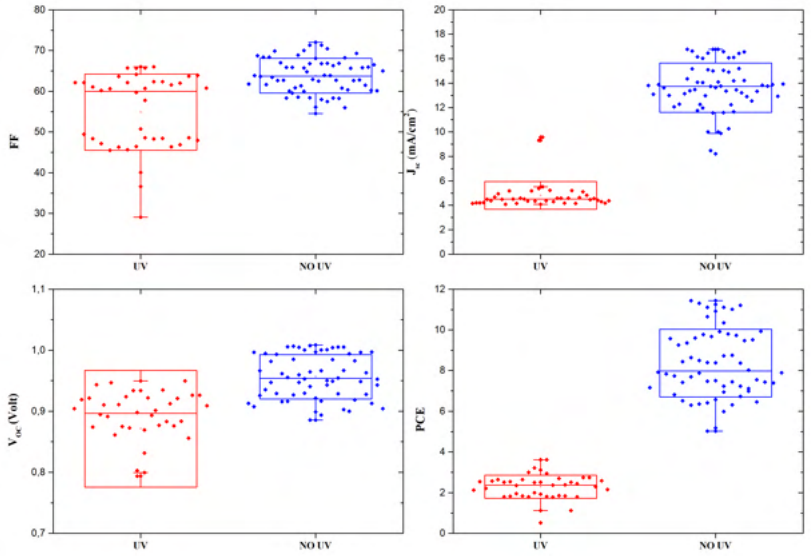

FIGURE 5.10: Comparison of photovoltaic parameters for pristine and UV-treated PIDTTDQ devices.

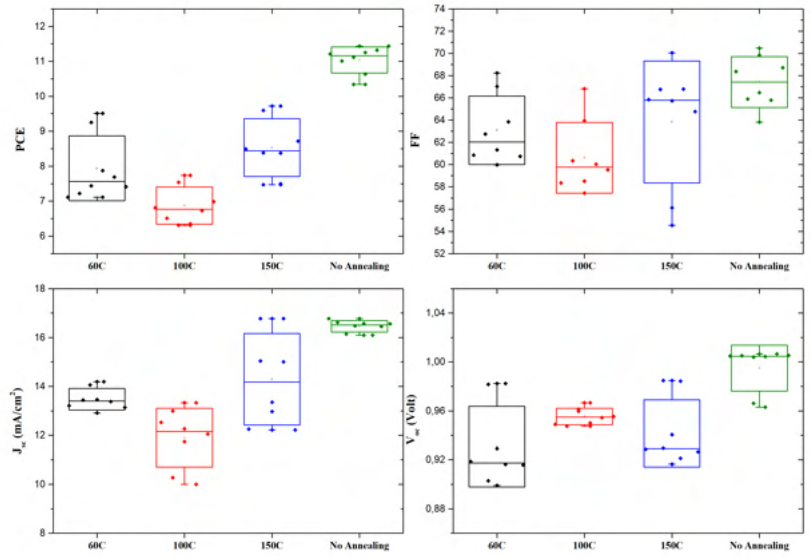

FIGURE 5.11: Comparison of photovoltaic parameters for various temperatures and non-annealed PIDTTDQ devices.

After realizing that the threshold concentration for perovskite deposition is 0.75 mg ml^{-1}, the PIDTTDQ film thickness was reduced until we reach an optimized

concentration.We observed inferior PCEs at intermediate concentrations.The best PCEs were obtained for concentrations of 0.2mg ml^{-1} or less. More specifically,the concentrations of 0.01,0.05,0.1 and 0.2 mg ml^{-1} were tested.20 devices were fabricated for each case, in order to find the best thickness with a good statistical sample.The box plots of each photovoltaic parameter are shown in figure 5.12. The champion and average photovoltaic parameters are shown in table 5.3 and 5.4, respectively.The devices with PIDTTDQ concentrations of 0.01,0.05,0.1 and 0.2 mg ml^{-1} showed a champion PCE of 13.77%, 14.70%, 13.97%, and 12.60% , a FF of 75.32%,77.51%,77.01%,73.25%. a V_{OC} of 1.03,1.06,1.05 and 0.96V,and finally a J_{SC} of 17.12,16.97,16.48 and 17.52 mA cm^{-2},respectively.For the average performance, the PIDTTDQ concentrations of 0.01,0.05,0.1 and 0.2 mg ml^{-1} showed a PCE of 10.81%,13.07%,12.15% and 11.22 %, a FF of 68.12%,74.96%,71.59% and 68.93%, a J_{SC} of 15.01,15.88,16.86 and 16.68 mA cm^{-2} and a V_{OC} of 1.01,1.04,0.97 and 0.95V, respectively. We conclude that the optimul thickness of PIDTTDQ corresponds to a concentration of 0.05 mg ml^{-1}.The thickness of the resulting PIDTTDQ film is 5nm or less, as it is on the detection limit of the AFM,as we measured it.Thickness optimization also involves the optimization of the trade-off between transparency and conductivity.While the higher PIDTTDQ concentrations yield higher J_{SC} values, they produce lower FF as a result of the reduced transparency and limited hole transport.We have seen that charge generation has an inverse thickness dependence,therefore optimizing the thickness can maximize the charge generation,transport and extraction processes.**We lead to the conclusion that the optimum conditions for the deposition of the PIDTTDQ film is using a 0.05 mg ml^{-1} solution,static spin coating at 4000rpm for 45s without post-treatment (thermal annealing).This leads to a thickness of $\approx$ 5nm.From now on,we will refer to these optimized conditions as PIDTTDQ devices.**

TABLE 5.3: Champion photovoltaic parameters for various concentrations for optimization of PIDTTDQ thickness

Concentration (mg ml^{-1})	PCE %	FF%	J_{SC} (mA cm^{-2})	V_{OC} (V)
0.01	13.77	75.32	17.12	1.03
0.05	14.70	77.51	16.97	1.06
0.1	13.97	77.01	16.48	1.05
0.2	12.60	73.25	17.52	0.96

TABLE 5.4: Average photovoltaic parameters for various concentrations for optimization of PIDTTDQ thickness

Concentration (mg ml^{-1})	PCE %	FF%	J_{SC} (mA cm^{-2})	V_{OC} (V)
0.01	10.81	68.12	15.01	1.01
0.05	13.07	74.96	15.880	1.04
0.1	12.15	71.59	16.86	0.97
0.2	11.22	68.93	16.68	0.95

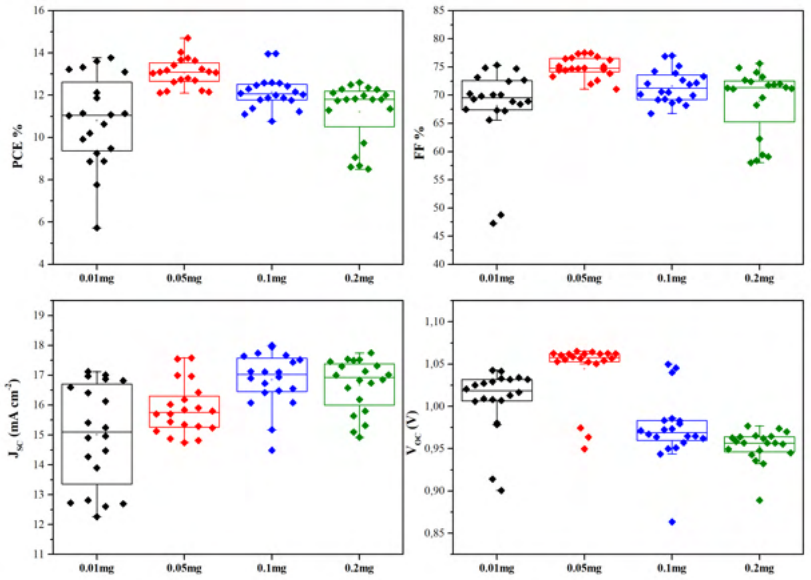

FIGURE 5.12: Box plots of various tested PIDTTDQ concentration for thickness optimization.

5.10 Device Performance of PIDTTDQ and PEDOT:PSS

After completing the optimization of the PIDTTDQ based devices, we compared its performance with the reference device. The HTL of the reference device is PEDOT:PSS, with a film thickness of ≈50nm. We have seen that the PIDTTDQ films are transparent for the same thickness. For the devices, a ≈ 5nm thickness of PIDTTDQ and a 50nm thickness for PEDOT:PSS are employed.We fabricated 20 devices both for PIDTTDQ and for PEDOT:PSS to compare their performance.The J-V characteristics of completed devices were measured in the N_2 filled glovebox using a solar simulator (Oriel) with a 450W Xenon Lamp. The intensity of the lamp

was calibrated at 100 mW cm^{-2} one sun AM1.5G illumination using a Keithley 2700 Data acquisition system equipped with a KG-5 Si diode. J-V curves of devices were measured with a multiplexor test board system (Ossila) by scanning from -0.1V to 1.2V, with a scan rate of 10mV s^{-1} and a voltage step of 10 mV. A metal mask was used to define the active area of the solar cells (0.0256 cm^2).

Table 5.6 summarized the champion photovoltaic parameters for both cases.For PIDTTDQ, the champion device showed a PCE of 14.70%,a FF of 77.51%,a J_{SC} of 16.97 mA cm^{-2} and a V_{OC} of 1.06V.The reference device with PEDOT:PSS showed a maximum PCE of 12.16%,a FF of 75.32%,a J_{SC} of 16.08 mA cm^{-2} and a V_{OC} of 0.95V.It is evident that PIDTTDQ exceeds the maximum PCE of the reference device, and shows an 110mV enhancement in the V_{OC}.A possible reason for the improvement of the V_{OC} in PIDTTDQ devices could be attributed to the deeper HOMO level of PIDTTDQ compared to PEDOT:PSS,as shown in the device energy diagram in figure 5.13.However, the origins of the V_{OC} enhancement will be further investigated.The champion JV curves obtained for both devices are shown in figure 5.14.

A statistical analysis of the device performance for 20 PSCs for each case will confirm the superior performance of PIDTTDQ compared to PEDOT:PSS.The average and best photovoltaic parameter values of 20 fabricated reference and PIDTTDQ devices are provided in Table 5.5 and 5.6 respectively,while the photovoltaic parameters for each device for both materials are shown in Table 5.7 and 5.8.A PCE histogram along with box plots for each photovoltaic parameter is shown in figure 5.15 and 5.16, respectively.On average, the PIDTTDQ devices showed a PCE of 13.07%,a FF of 74.96%,a J_{SC} of 15.88 mA cm^{-2} and a V_{OC} of 1.04V,while the Reference device with PEDOT:PSS showed on average a PCE of 11.82%,a FF of 76.56%,a J_{SC} of 15.82 mA cm^{-2} and a V_{OC} of 0.93V.It is now clear from all the statistical analysis that the performance of the inverted PSCs is enhanced by employing the PIDTTDQ as the HTL.

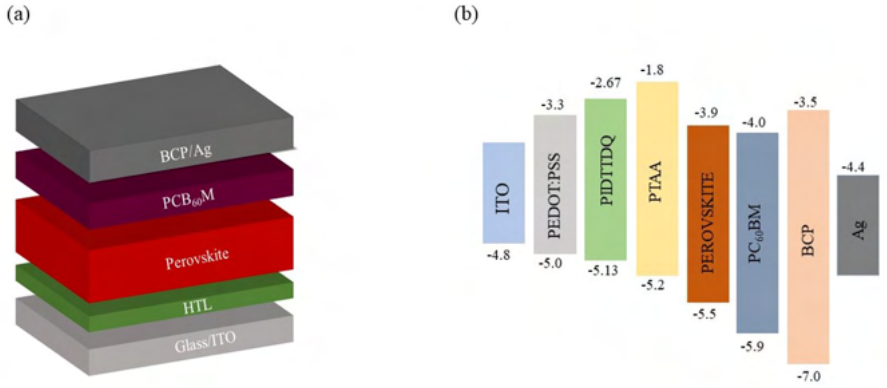

FIGURE 5.13: a)Inverted PSC architecture b) Energy level diagram for the inverted PSCs.

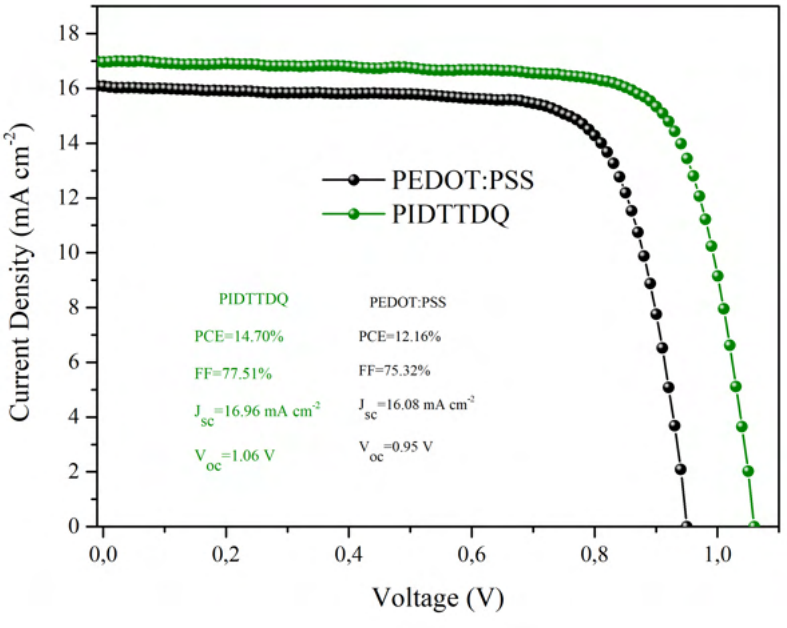

FIGURE 5.14: Champion JV curves for PIDTTDQ and PEDOT:PSS

TABLE 5.5: Average photovoltaic parameters for 20 fabricated devices with PIDTTDQ and PEDOT:PSS

Device	PCE %	FF%	J_{SC}(mAcm^{-2})	V_{OC}(V)	R_{SH}(kΩcm^{-2})	$R_S(\Omega cm^{-2})$
PIDTTDQ	13.07	74.96	15.88	1.04	3.08	5.81
PEDOT:PSS	11.82	76.56	15.82	0.93	3.15	5.28

TABLE 5.6: Champion photovoltaic parameters for 20 fabricated devices with PIDTTDQ and PEDOT:PSS

Device	PCE %	FF%	J_{SC}(mAcm^{-2})	V_{OC}(V)	R_{SH}(kΩcm^{-2})	$R_S(\Omega cm^{-2})$
PIDTTDQ	14.70	77.51	16.97	1.06	2.03	5.34
PEDOT:PSS	12.16	75.32	16.08	0.95	0.55	5.64

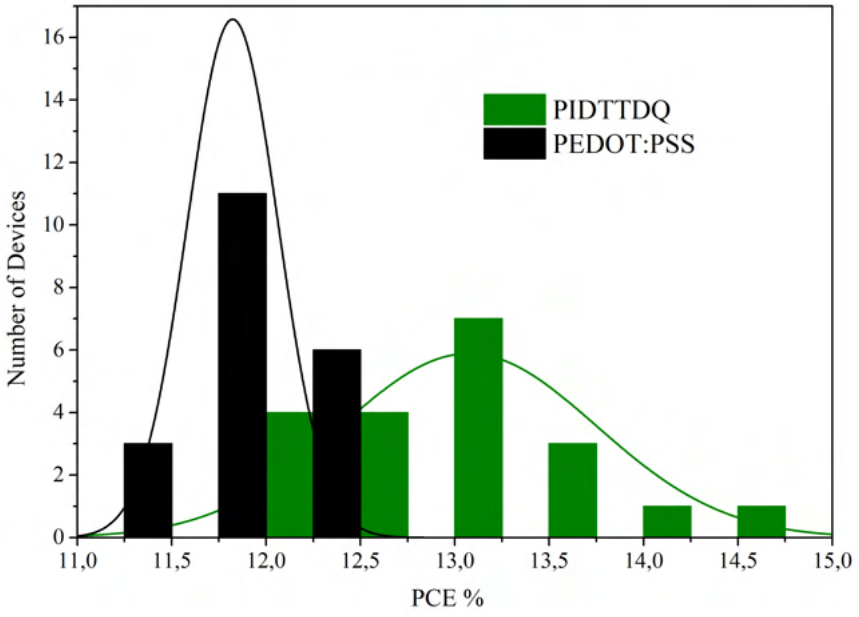

FIGURE 5.15: PCE histogram with Gaussian distribution for PEDOT:PSS and PIDTTDQ devices

TABLE 5.7: Photovoltaic parameters of the 20 Reference devices with PEDOT:PSS

Device	PCE %	FF%	J_{SC}(mAcm^{-2})	V_{OC}(V)	$R_S(\Omega cm^{-2})$	R_{SH}(kΩcm^{-2})
1	12.16	75.32	16.08	0.95	5.64	0.55
2	12.14	77.49	15.95	0.93	5.34	1.67
3	12.11	76.40	16.14	0.93	5.24	1.82
4	12.08	77.62	15.73	0.94	5.24	0.52
5	12.08	75.76	15.83	0.96	5.23	0.84
6	12.04	77.83	15.70	0.94	5.21	0.69
7	11.96	77.79	15.54	0.94	5.43	0.83
8	11.93	76.37	15.59	0.95	5.25	3.33
9	11.91	77.33	15.65	0.93	5.73	0.80
10	11.86	75.82	15.69	0.95	5.11	0.70
11	11.85	76.86	15.60	0.94	5.41	0.68
12	11.80	77.29	15.65	0.95	5.41	15.50
13	11.74	78.29	15.32	0.93	5.11	0.81
14	11.63	72.75	16.41	0.93	5.63	0.34
15	11.61	75.79	16.73	0.90	4.74	0.79
16	11.60	75.96	16.44	0.91	4.89	20.43
17	11.57	77.31	15.60	0.91	5.19	6.21
18	11.50	74.91	15.38	0.95	5.51	0.33
19	11.45	77.26	15.34	0.92	5.43	2.95
20	11.45	77.03	15.96	0.91	4.82	3.23
AVERAGE	**11.82**	**76.56**	**15.82**	**0.93**	**5.28**	**3.15**

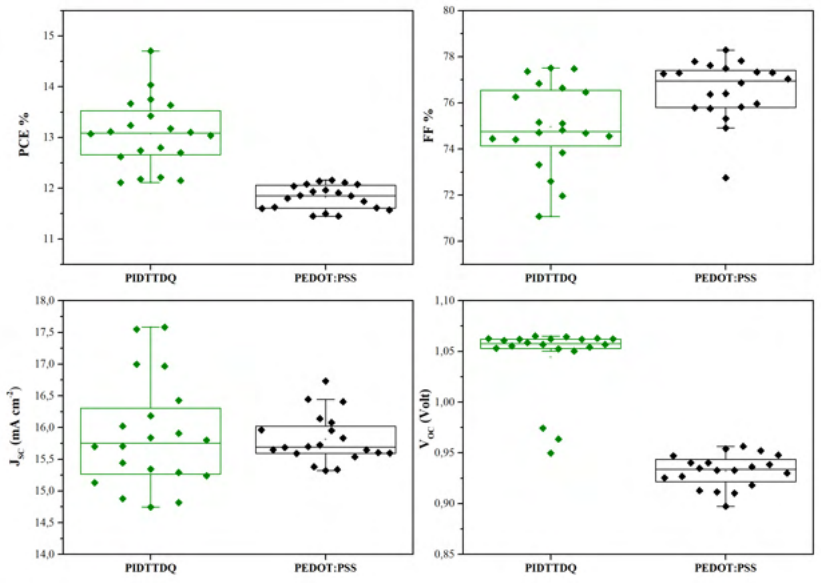

FIGURE 5.16: Box plots with photovoltaic parameters of 20 fabricated devices with PEDOT:PSS and PIDTTDQ

TABLE 5.8: Photovoltaic parameters of the 20 devices with PIDTTDQ

Device	PCE %	FF%	J_{SC}(mAcm^{-2})	V_{OC}(V)	$R_S(\Omega cm^{-2})$	R_{SH}(kΩcm^{-2})
1	14.70	77.51	16.97	1.06	5.34	2.03
2	14.04	77.36	16.18	1.07	5.83	3.91
3	13.75	77.48	16.02	1.05	5.79	0.6
4	13.67	76.64	17.58	0.96	3.71	0.79
5	13.64	76.84	15.84	1.06	5.66	6.1
6	13.42	76.46	15.71	1.06	6.22	0.86
7	13.24	74.82	15.91	1.06	5.54	0.78
8	13.18	75.11	17.55	0.95	3.95	1.71
9	13.11	74.71	15.70	1.06	5.60	0.90
10	13.10	75.15	17.00	0.97	3.92	2.1
11	13.07	71.97	16.43	1.05	5.89	0.81
12	13.04	76.26	15.34	1.06	5.97	0.74
13	12.80	74.69	15.44	1.05	6.20	0.71
14	12.74	72.60	15.80	1.06	5.91	0.62
15	12.70	74.41	15.29	1.06	6.56	1.62
16	12.62	74.56	15.13	1.06	6.06	32.71
17	12.21	74.45	14.75	1.06	6.42	0.97
18	12.18	73.84	14.88	1.05	6.91	1.57
19	12.15	73.32	14.82	1.06	6.58	1.66
20	12.11	71.08	15.24	1.06	8.14	0.44
AVERAGE	**13.07**	**74.96**	**15.88**	**1.04**	**5.81**	**3.08**

5.11 Current density from EQE

All current densities seen previously are from the solar simulator.These values must be compared to the ones obtained from EQE measurements.EQE measurements were performed on a commercial system from Enlitech (QE-R2) with a chopping frequency of 65Hz.The EQE spectra for both PIDTTDQ and PEDOT:PSS complete champion devices are shown in figure 5.17. It is clear that the current response of PIDTTDQ devices is more steady at visible wavelengths than PEDOT:PSS,as the improved transparency reduces the optical losses.The calculated J_{SC} for PIDTTDQ and PEDOT:PSS was 16.34 and 15.93 mAcm^{-2},respectively .These values are almost in agreement with the ones obtained from the solar simulator.The current from the simulator and from EQE are presented in Table 5.9.

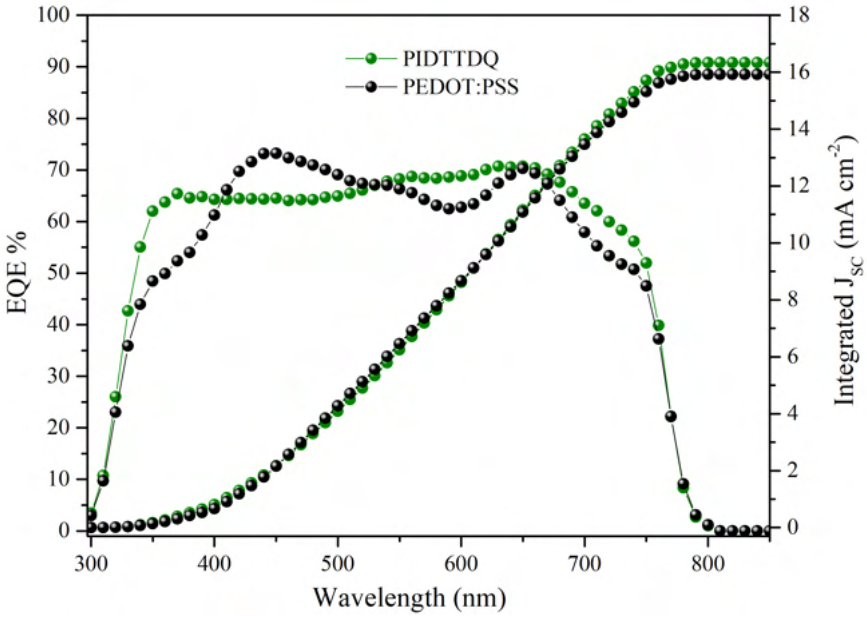

FIGURE 5.17: EQE spectral response of PIDTTDQ and PEDOT:PSS devices.

TABLE 5.9: Current Density obtained from the solar simulator and EQE measurements.

Device	J_{SC}(mAcm^{-2})	J_{SC}(EQE)(mAcm^{-2})
PIDTTDQ	16.97	16.34
PEDOT:PSS	16.08	15.93

5.12 TPV and TPC measurements

To further investigate the improved V_{OC} for the case of PIDTTDQ,we performed TPV and TPC measurements.Transient photovoltage and Transient Photocurrent measurements were performed with a commercial apparatus (Arkeo, Cicci Research s.r.l.) based on a high-speed Waveform Generator that drives a high-speed LED (5000 Kelvin). The device is connected to a trans-impedance amplifier and a differential voltage amplifier to monitor short circuit current or open-circuit voltage. The light intensity from the pulse is varied between 0.001-2 sun equivalent. For Transient Photovoltage, the perturbation produced by the LED is less than 10% the background applied light bias. Transient photocurrent measurements were performed under large perturbations (Duty cycle 0.3) for a time duration of 400μs.

Devices are connected to a 50Ω and 1MΩ resistor for TPC and TPV measurements, respectively.

The TPV measurements were initially investigated.The TPV transients for various light intensities for both PIDTTDQ and PEDOT:PSS are shown in figure 5.18 and 5.19,respectively. The recombination dynamics for both materials can be illustrated by plotting the obtained mono-exponential lifetime τ as a function of bias, as shown in figure 5.20. It is clear that for the case of the reference device with PEDOT:PSS, the line has a steeper slope than PIDTTDQ, meaning that the carrier lifetime of the reference device is less than PIDTTDQ. Hence we conclude that the PIDTTDQ has slower recombination dynamics than the PEDOT:PSS reference device. Another convenient way to illustrate the difference in the carrier lifetime is by plotting 2 TPV decays, as shown in figure 5.21. The PIDTTDQ device has a slower voltage decay than for the case of PEDOT:PSS.The obtained carrier lifetimes that correspond to this decay are 1.78 μs for PIDTTDQ and 0.8 μs for PEDOT:PSS as shown in Table 5.10.

TABLE 5.10: Carrier lifetimes obtained from the TPV decays of figure 5.21.

Device	Carrier Lifetime (μs)
PEDOT:PSS	1.78
PIDTTDQ	0.80

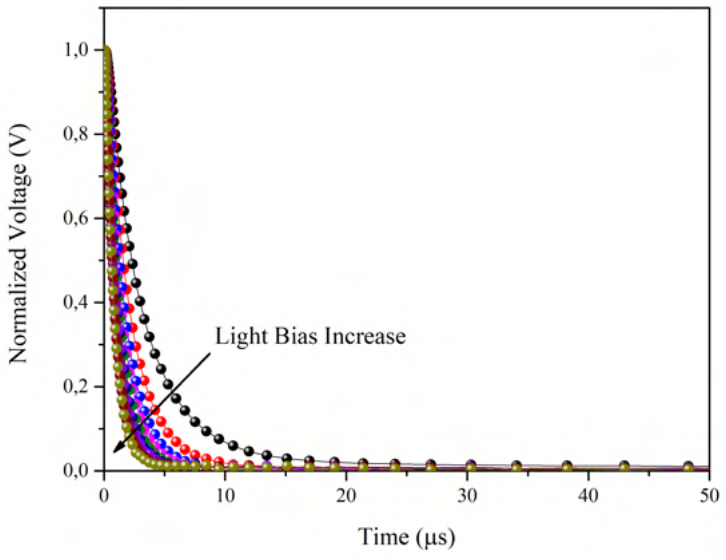

FIGURE 5.18: TPV decays for increasing light intensity up to 2sun for PIDTTDQ.

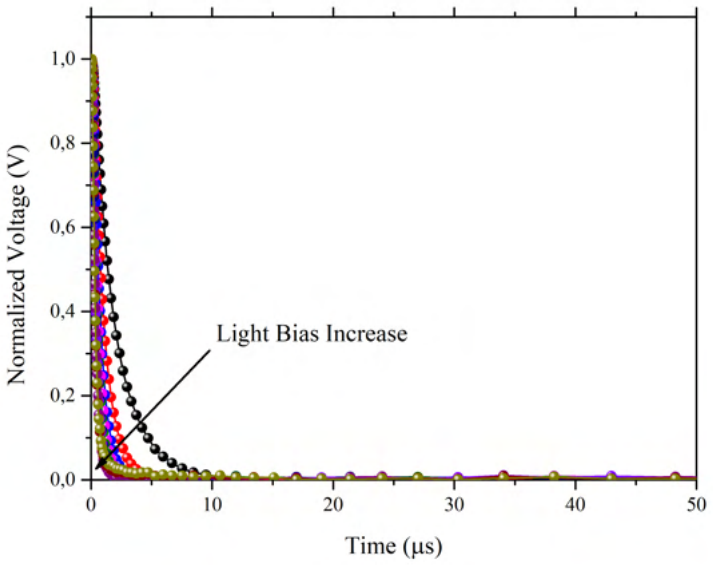

FIGURE 5.19: TPV decays for increasing light intensity up to 2sun for PEDOT:PSS.

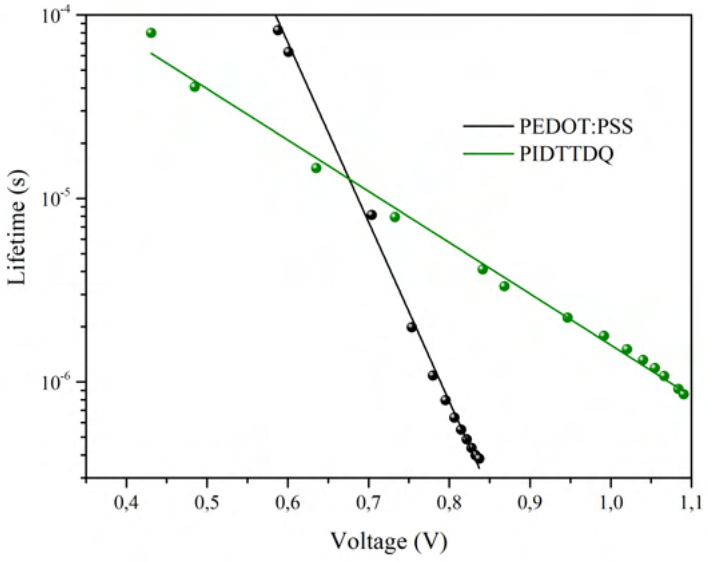

FIGURE 5.20: Lifetime from TPV as a function of Voltage.

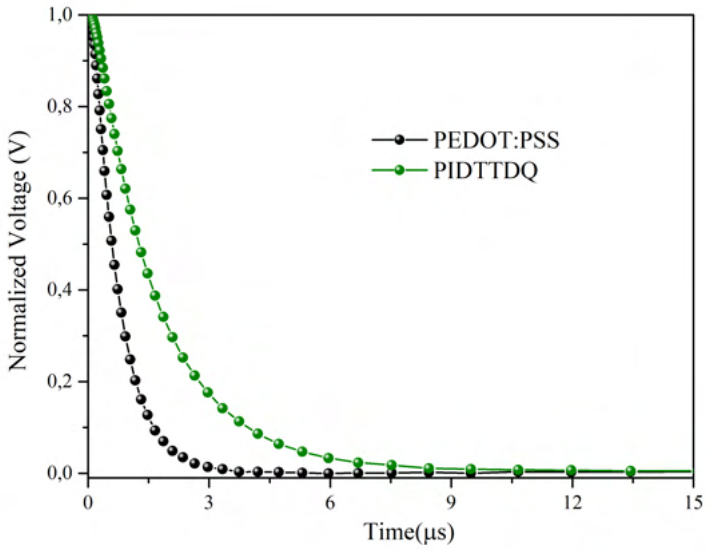

FIGURE 5.21: TPV decays for PIDTTDQ and PEDOT:PSS devices under the same illumination.

Complementary to TPV,we performed TPC measurements under large perturbations (Duty Cycle of 0.3), to investigate charge transport and extraction.The TPC transients for various light intensities are presented in figure 5.22 and 5.23 for PIDTTDQ and PEDOT:PSS,respectively. To gain more insights about charge transport and extraction, we plotted the extracted charge, which can be obtained by integrating each TPC decay, as a function of the current density. This is shown in figure 5.24. Notice that as the current density increases, more charges are generated by the LED pulses, and the amount of extracted charge increases linearly with current density. We also observe for the case of PIDTTDQ that the amount of extracted charge is higher than PEDOT:PSS as the current density increases.We conclude that the PIDTTDQ HTL provides improved charge extraction compared to PEDOT:PSS.This was expected as we have seen from TPV measurements that the carrier lifetimes for the case of PEDOT:PSS were less than PIDTTDQ. It is possible that charges are lost at the PEDOT:PSS/perovskite interface. A defective interface can contribute to non-radiative interfacial recombination, along with non-radiative recombination in the bulk which is attributed to defects or the GBs of the perovskite film.

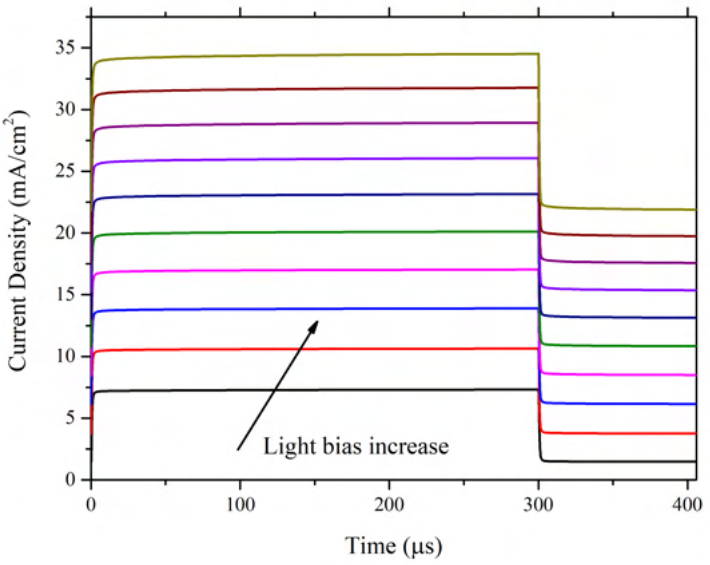

FIGURE 5.22: TPC transients for various light intensities up to 2 sun for PIDTTDQ devices.

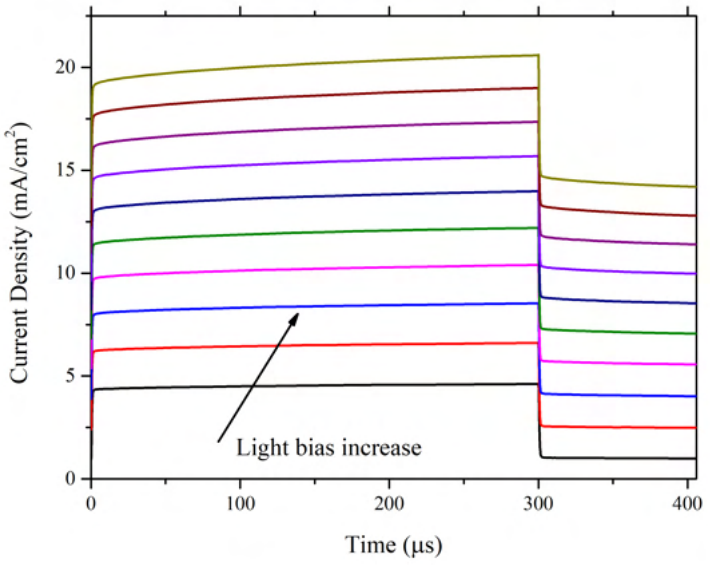

FIGURE 5.23: TPC transients for various light intensities up to 2 sun for PEDOT:PSS reference devices.

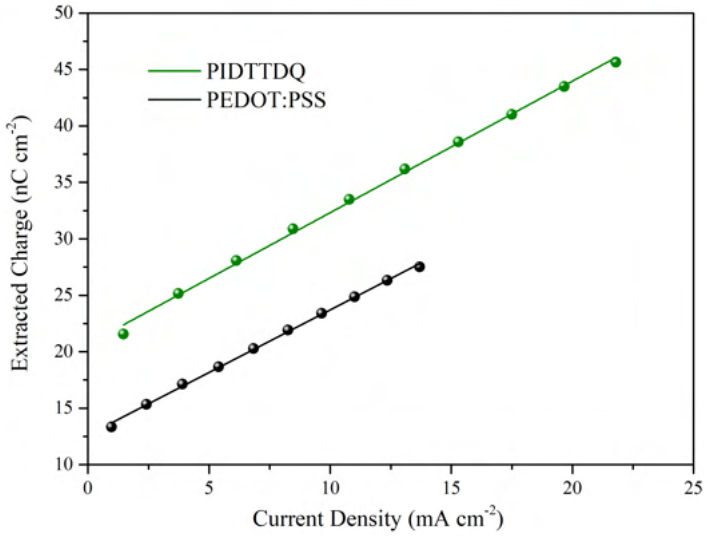

FIGURE 5.24: Extracted charge obtained from TPC as a function of Current density for PIDTTDQ and PEDOT:PSS devices.

5.13 Steady state and Time-Resolved Photoluminescence

5.13.1 Steady State PL

To investigate the hole extracting ability of both HTLs,we performed steady-state and TRPL PL measurements.Steady-state PL measurements were performed with a commercial platform (ARKEO - Cicci Research): the substrate is illuminated with a diode-pumped solid-state (DPSS) Nd:YVO_4+KTP Laser (Peak wavelength 532 nm ± 1 nm, Optical power 1 mW on a circular spot of 2 mm of diameter: 31 mW cm^{-2}) at an inclination of 45°.The fluorescence on the opposite side of the substrate is focused on a bundle of fibers (10 mm in diameter) with an aspheric lens close to the substrate in order to maximize the PL. The bundle sends the signal to a CCD-based spectrometer. Integration time and the number of averaging is maintained the same in order to better compare the results. Time-Resolved Photoluminescence TRPL was measured with an FS5 Spectrofluorometer from Edinburgh Instruments. A 478.4nm laser was used as an excitation source.

The steady-state PL measurements were performed on the Glass side of the Glass/ITO substrates to study charge transfer only.Films with the optimized 0.05 mg ml^{-1} PIDTTDQ and PEDOT:PSS films on Glass/Perovskite and for bare

perovskite film were prepared.The resultant PL spectra for all three cases are shown in 5.25. We see that all PL emission peaks appear at the same peak of ≈ 770nm, as expected [226]. This peak is due to radiative band-to-band recombination. The PL intensity for the case of using a HTL is quenched compared to the intensity of the bare perovskite film, which indicates the hole extracting ability of both materials. We also observe that the PL intensity of both HTL is almost identical with a small difference in intensity, indicating the similar how to transfer abilities of both HTL.A large PL quenching is associated with improved charge transfer at the HTL-Perovskite interface [227–230].

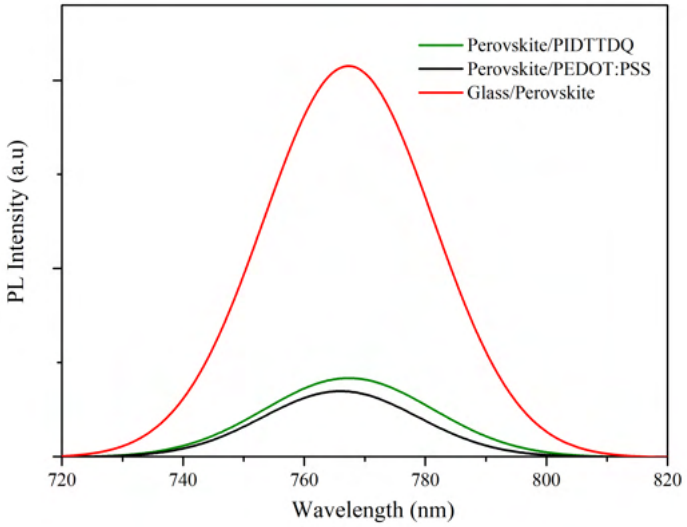

FIGURE 5.25: PL spectra for bare perovskite film and perovskite on PIDTTDQ and PEDOT:PSS.

5.13.2 TRPL

To further investigate the charge carrier dynamics at the HTL-Perovskite interface and in the bulk, TRPL measurements were performed on HTL/Perovskite films to investigate the charge carrier dynamics in both PIDTTDQ and PEDOT:PSS on perovskite. For comparison, a bare perovskite film was also prepared. The resultant lifetimes from fitting a function of the form

$$R(t) = B + A_1 \cdot \exp\left(-t/\tau_1\right) + A_2 \cdot \exp\left(-t/\tau_2\right) \tag{5.4}$$

are presented in Table 5.11.The average lifetime is also shown.The average lifetime is calculated by the formula

$$\tau_{avg} = \frac{A_1\tau_1^2 + A_2\tau_2^2}{A_1\tau_1 + A_2\tau_2} \tag{5.5}$$

wherein both equations A_1 and A_2 are exponential pre-factors of the decay, τ_1 time constant is called the "fast" component of the decay and is associated with interface recombination or mainly charge transport, and the τ_2 lifetime is referred to the "slow" component and is associated with non-radiative recombination in the bulk.The Normalized TRPL decays for the bare perovskite and for PIDTTDQ and PEDOT:PSS are shown in figure 5.26.The obtained τ_1 is 10.54 for the bare perovskite,2.67ns for PEDOT:PSS and 5.02ns for PIDTTDQ.The τ_1 component becomes faster for both HTL,which indicates efficient hole transport for both materials.The fitting also revealed a τ_2 component of 162ns for the bare perovskite, 46.1ns for PEDOT:PSS and 132.5ns for PIDTTDQ.This is an indication that the PIDTTDQ suppresses the non-radiative recombination. It is possible that the suppression of the non-radiative recombination involves the bulk of the perovskite and not just the HTL-Perovskite interface. The mechanism behind the higher τ_2 for the case of PIDTTDQ might be the reduced number of defects [216].

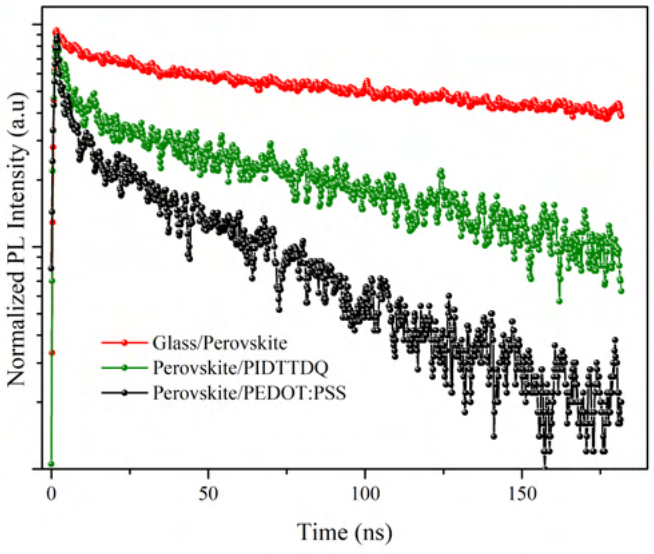

FIGURE 5.26: Time Resolved Photoluminescene for bare perovskite and perovskite on PIDTTDQ and PEDOT:PSS

TABLE 5.11: All calculated lifetime components from exponential tail fit of TRPL measurements.

HTL	τ_1(ns)	τ_2(ns)	τ_{avg}(ns)
Perovskite	10.54	162	158.1
PIDTTDQ	5.02	132.5	128.7
PEDOT:PSS	2.67	49.2	46.1

5.14 Defect Population from Dark IV Characteristics

The much slower τ_2 component from TRPL measurement might be an indicator for a reduced number of defects in the perovskite film for the case of PIDTTDQ. This assumption must be quantitatively confirmed. This is achieved by studying the JV characteristics of hole-only devices with the perovskite film sandwiched between 2 HTLs and 2 contact electrodes. The dark JV characteristics of the hole-only devices were studied by using the same commercial platform (ARKEO - Cicci Research) as in TPV and TPC measurements. The hole-only devices are connected to 2 probes on the 2 contact electrodes,and the dark JV curves are obtained by scanning from -0.1 up to 2V, with a voltage step of 10mV and a scan rate of 300 mV s^{-1}.The device geometries employed in these measurements are ITO/PEDOT:PSS/Perovskite/PTAA/Au and ITO/PIDTTDQ/Perovskite/PTAA/Au.Similarly, with hole-only devices for the HTL mobility measurements, a PTAA solution with a high concentration of 10 mg ml^{-1} was used, which forms a film with a thickness of ≈100nm. 100nm of Au were thermally evaporated as a back contact due to the deeper work function that helps the extraction and the injection of holes in the perovskite film.For a sufficient HTL thickness, a higher PIDTTDQ concentration of 0.5 mg ml^{-1} was used.The obtained dark JV characteristics of both devices are shown in figure 5.27. A first observation is that the values of the reverse saturation current density J_0 are larger by three orders of magnitude. A larger J_0 means the existence of shunts that block the photocurrent. A large J_0 leads to reduced V_{OC}.PIDTTDQ devices showed a 110mV improvement on average compared to PEDOT:PSS,which is consistent with the higher observed J_0 values.Using the SCLC model for traps, the graph can be divided into three regions: In the first region the current increases linearly with voltage (Linear region), in the second region the current increases abruptly with a slope larger than 3, which is the trap filling region (TFL) and in the third region the slope is equal to 2 (Child region).In this graph, the third region is not shown.

The transition from the linear to the Trap filling region occurs at the trap filling voltage V_{TFL}, and the perovskite defect density is obtained by equation 4.50:

$$N_d = \frac{2\epsilon\epsilon_0 V_{TFL}}{ed^2} \tag{5.6}$$

where V_{TFL} is the trap filling voltage that we will obtain by the intercept of the fitting lines in the linear and the trap filling region (equation 4.54), N_d is the perovskite defect density,ϵ_0=8.85· 10^{-14} F cm^{-1} is the vacuum permittivity,ϵ=46.9 and d=450nm is the perovskite permittivity and thickness,respectively.The intercept point that corresponds to V_{TFL} for both PIDTTDQ and PEDOT:PSS was calculated at 0.70V and 0.83V,respectively. The calculated defect densities for PIDTTDQ and PEDOT:PSS are $1.79 \cdot 10^{16}$ cm^{-3} and $2.12 \cdot 10^{16}$ cm^{-3}.These results are summarized in Table 5.12.The higher defect density calculated for PEDOT:PSS confirms the obtained results from TRPL

TABLE 5.12: Current Density obtained from the solar simulator and EQE measurements.

HTL	$V_{TFL}(V)$	Defect density $N_D(10^{16}$ $cm^{-3})$
PEDOT:PSS	0.70	1.79
PIDTTDQ	0.83	2.12

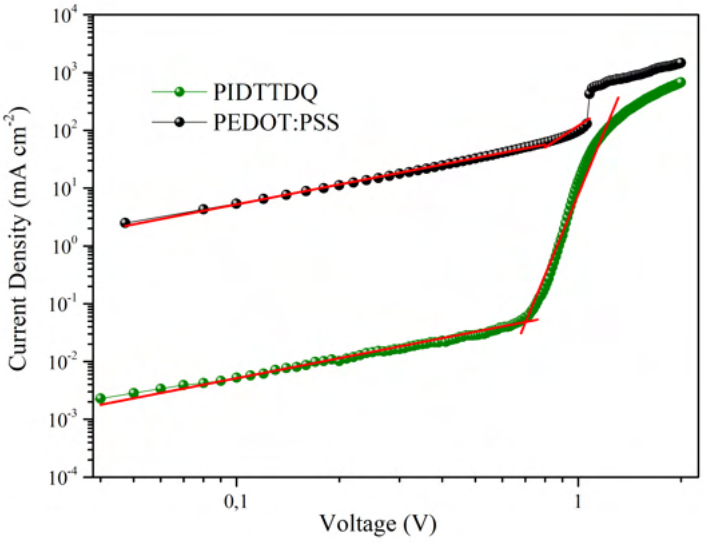

FIGURE 5.27: Dark JV characteristics of hole-only devices with Perovskite layer.

5.15 Stability Measurements

Stability is another crucial aspect that we have to examine solar cell devices, which also determines the commercialization of the technology. For this purpose, we tested the stability of the fabricated devices in ambient air under a humidity ranging between 50-65%, without any encapsulation or exposure to ambient light. For each measurement, the devices were transferred to the glovebox for measurement. The results are shown in figure 5.28, where the PCE evolution is plotted as a function of time. It is obvious that the PEDOT:PSS reference devices degrade at a very fast rate, and last for less than 300h. The reasons for the poor stability of PEDOT:PSS were discussed in section 5.1 and therefore we expect this rapid degradation. On the other hand, the PIDTTDQ device maintained more than 75% of their initial PCE for almost 900h, which demonstrates the hydrophobic nature of the material and the increased humidity tolerance.The stability of PIDTTDQ is improved even when compared to PTAA, the most efficient HTL in inverted PSCs.The devices with PTAA showed a worse degradation rate that was evident from the passage of 500h. The devices degraded at 60% of their initial PCE. Therefore, we confirmed our expectations for the increased humidity tolerance of PIDTTDQ from contact angle measurements. The Conjugated polymer shows an improved ability to prevent humidity penetration in the device, resulting in an enhanced device lifetime.The comparison of PIDTTDQ with the also hydrophobic PTAA shows the potential of the material as a potential HTL rival for inverted PSCs.

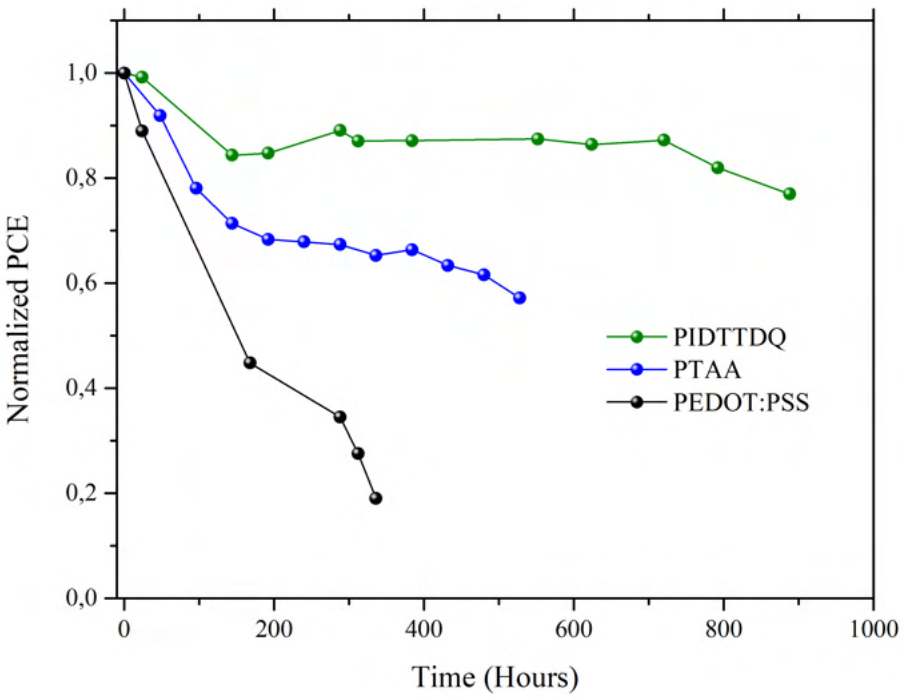

FIGURE 5.28: PCE evolution as a function of exposure time in ambient air for PEDOT:PSS,PIDTTDQ and PTAA devices.

5.16 Synthetic Complexity

We have studied and compared the performance and the stability of PIDTTDQ to PEDOT:PSS and PTAA. We will study now PIDTTDQ in terms of cost.The Synthetic Complexity (SC) of an organic semiconductor is an important parameter to quantify the potential of such material to be employed in commercial applications [231], therefore we estimated the SC for PIDTTDQ based on a literature procedure [232].The SC was found to be 55 for the case of PIDTTDQ ,which is considered a relatively low SC,similar to other novel materials that have been employed in PSCs [233]. Minimizing the SC corresponds to minimizing the cost and the number of the synthetic procedures, the purification steps, and the safety of the reagents used.

5.17 Concluding Remarks

To summarize, we investigated the performance of a novel Conjugated polymer PIDTTDQ as the HTL in inverted PSCs. After optimization, the optimal thickness for PIDTTDQ was obtained at a concentration of 0.05 mg ml^{-1} and the best device

for PIDTTDQ showed a PCE of 14.70%, compared to the reference device with PEDOT:PSS which showed an optimal PCE of 12.16%. The device characterization revealed suppression of interface Recombination for PIDTTDQ and higher charge losses for PEDOT:PSS respectively and suppression of non-radiative recombination in the case of PIDTTDQ, which can be attributed to the reduced defect density and the V_{OC} enhancement. Finally, the hydrophobic nature of PIDTTDQ extended the device stability for almost 900h by retaining more than 75% of its initial PCE. The stability of PIDTTDQ was also compared with PTAA, showing a significant improvement in the device stability and extending the lifetime of inverted PSCs. The low synthetic complexity of this promising, novel, hydrophobic material along with further molecular engineering can expand its use in large-area devices.The advantages of using PIDTTDQ are the following:

- Transparency
- Smooth Morphology and good film formation properties
- Improved energy level matching
- Low temperature processing
- Low Synthetic Complexity
- Humidity tolerance
- Compatibility with large area substrates
- Efficient interfacial engineering and elimination of non-radiative recombination

while the drawbacks are the following:

- Poor surface wetting for perovskite film formation.
- Thickness limitations

Potential future modifications of the PIDTTDQ material to improve the PCE could be the following:

- Use as HTL in Planar PSCs
- Ultrathin passivation layer
- Dopants to enhance conductivity

- Resolve the poor wetting issue
- Further Molecular Engineering

The use as HTL in planar PSCs will involve the use of the Li-TFSI and tBP dopants, along with more optimization as the wetting issue is now resolved due to the device geometry. The improved τ_2 lifetime in TRPL decay would indicate an underlying defect passivation mechanism, which could make PIDTTDQ a potential passivant on top of the perovskite film as an ultrathin layer. The advantage here is that the concentration that yields a low thickness is known. The use of dopants in the Inverted geometry can also be a potential solution to enhance conductivity since increasing the thickness has a further limitation due to the poor wetting properties of PIDTTDQ. Finally, further molecular engineering can provide further improvement in the device's performance.This work mainly achieved the cost and stability step, as it is shown in figure 5.29 in comparison with the ideal sweet spot of maximum PCE, cost and stability.

FIGURE 5.29: Illustration of how close this work is on the ideal sweet spot of stability cost and efficiency.

Appendix A

Mott-Gurney Law derivation

Suppose we have a p-type semiconductor with a thickness d, with a hole mobility μ_p. If an electric field E is applied, a drift current flows into the material.The electric field is depend on the position x inside the material through the Poisson's law:

$$\frac{dE}{dx} = \frac{\rho}{\epsilon} = \frac{qp}{\epsilon} \tag{A.1}$$

The drift current for the case of space charge is

$$J_{SCLC} = q\mu_p pE \Longrightarrow p = \frac{J_{SCLC}}{\epsilon\mu_p E} \tag{A.2}$$

If we plug the expression for p from equation A.2 to equation A.1,we get

$$\frac{dE}{dx} = \frac{J_{SCLC}}{\epsilon\mu_p} \tag{A.3}$$

By integrating, we get:

$$\int_0^E E\,dx \;= \frac{J_{SCLC}}{\epsilon\mu_p}\int_0^x dx \;\Longrightarrow \tag{A.4}$$

$$E(x) = \sqrt{\left(\frac{2J_{SCLC}}{\epsilon\mu_p}\right)}\cdot\sqrt{x} \tag{A.5}$$

By changing E with

$$E = -\frac{dV}{dx} \tag{A.6}$$

we get

$$-\int_0^V dV \;= \sqrt{\left(\frac{2J_{SCLC}}{\epsilon\mu_p}\right)}\int_0^d \sqrt{x}\,dx \;\Longrightarrow \tag{A.7}$$

$$J_{SCLC} = \frac{9}{8}\mu\epsilon\frac{V^2}{L^3} \tag{A.8}$$

References

[1] Ritchie, H. and Roser, M. CO_2 emission by region,online image. URL https://ourworldindata.org/co2-emissions.

[2] BP,. Bp statistical review of World Energy. Technical report, 2019. URL https://on.bp.com/36qucwI.

[3] Lamont, L. *History of Photovoltaics*, volume 1, pages 31–45. 12 2012. ISBN 9780080878737. URL https://doi.org/10.1016/B978-0-08-087872-0.00102-5.

[4] Effect of light on Selenium during the passage of an electric current. *Nature*, 7 (173):303–303, Feb 1873. ISSN 1476-4687. URL https://doi.org/10.1038/007303e0.

[5] Wikipedia,. Timeline of solar cells, . URL https://en.wikipedia.org/wiki/Timeline_of_solar_cells.

[6] Hertz, H. Ueber einen Einfluss des ultravioletten Lichtes auf die electrische Entladung, January 1887. URL https://doi.org/10.1002/andp.18872670827.

[7] Einstein, A. Über einen die erzeugung und verwandlung des lichtes betreffenden heuristischen gesichtspunkt. *Annalen der Physik*, 322(6):132–148, 1905. URL https://doi.org/10.1002/andp.19053220607.

[8] Lenardic, D. Photovoltaics-historical development. URL http://www.pvresources.com/en/introduction/history.php.

[9] Wikipedia,. Growth of photovoltaics, . URL https://en.wikipedia.org/wiki/Growth_of_photovoltaics.

[10] Ota, Y. Silicon molecular beam epitaxy. *Thin Solid Films*, 106(1):1 – 136, 1983. ISSN 0040-6090. URL https://doi.org/10.1016/0040-6090(83)90180-3.

[11] Kibria, M., Ahammed, A., Sonyy, S., Sony, F., and Hossain, S.-U.-I. A review: Comparative studies on different generation solar cells technology. 09 2014.

[12] Wikipedia,. Allotropic forms of silicon, . URL https://bit.ly/2TYfASu.

[13] Alajlani, Y., Alaswad, A., Placido, F., Gibson, D., and Diyaf, A. *Inorganic Thin Film Materials for Solar Cell Applications*. 01 2018. ISBN 9780128035818. URL https://doi.org/10.1016/B978-0-12-803581-8.10355-8.

[14] Shirakawa, H., Louis, E. J., MacDiarmid, A. G., Chiang, C. K., and Heeger, A. J. Synthesis of electrically conducting organic polymers: Halogen derivatives of polyacetylene, (ch). *J. Chem. Soc., Chem. Commun.*, pages 578–580, 1977. URL https://doi.org/10.1039/C39770000578.

[15] Sariciftci, N. S., Smilowitz, L., Heeger, A. J., and Wudl, F. Photoinduced Electron Transfer from a Conducting Polymer to Buckminsterfullerene. *Science*, 258(5087):1474–1476, nov 1992. URL https://doi.org/10.1126/science.258.5087.1474.

[16] Leblebici, S. Y., Chen, T. L., Olalde-Velasco, P., Yang, W., and Ma, B. Reducing exciton binding energy by increasing thin film permittivity: An effective approach to enhance exciton separation efficiency in organic solar cells. *ACS Applied Materials & Interfaces*, 5(20):10105–10110, Oct 2013. ISSN 1944-8244. URL https://doi.org/10.1021/am402744k.

[17] Haugeneder, A., Neges, M., Kallinger, C., Spirkl, W., Lemmer, U., Feldmann, J., Scherf, U., Harth, E., Gügel, A., and Müllen, K. Exciton diffusion and dissociation in conjugated polymer/fullerene blends and heterostructures. *Phys. Rev. B*, 59:15346–15351, Jun 1999. URL https://doi.org/10.1103/PhysRevB.59.15346.

[18] Shaw, P. E., Ruseckas, A., and Samuel, I. D. W. Exciton diffusion measurements in Poly(3-hexylthiophene). *Advanced Materials*, 20(18):3516–3520. URL https://doi.org/10.1002/adma.200800982.

[19] Organic and perovskite solar cells: Working principles, materials and interfaces. *Journal of Colloid and Interface Science*, 488:373–389, 2017. ISSN 0021-9797. URL https://doi.org/10.1016/j.jcis.2016.11.021.

[20] Yan, C., Barlow, S., Wang, Z., Yan, H., Jen, A. K.-Y., Marder, S. R., and Zhan, X. Non-fullerene acceptors for organic solar cells. *Nature Reviews Materials*, 3(3):18003, Feb 2018. ISSN 2058-8437. URL https://doi.org/10.1038/natrevmats.2018.3.

[21] Lin, Y., Magomedov, A., Firdaus, Y., Kaltsas, D., El-Labban, A., Faber, H., Naphade, D. R., Yengel, E., Zheng, X., Yarali, E., Chaturvedi, N., Loganathan, K., Gkeka, D., AlShammari, S. H., Bakr, O. M., Laquai, F., Tsetseris, L., Getautis, V., and Anthopoulos, T. D. 18.4% organic solar cells

using a high ionization energy self-assembled monolayer as hole-extraction interlayer. *ChemSusChem*, n/a(n/a). URL https://doi.org/10.1002/cssc.202100707.

[22] Haque, S. M., Ardila-Rey, J. A., Umar, Y., Rahman, H., Mas'ud, A. A., Muhammad-Sukki, F., and Albarracin, R. Polymeric materials for conversion of electromagnetic waves from the sun to electric power. *Polymers*, 10(3), 2018. ISSN 2073-4360.

[23] Wang, H.-J., Chen, C.-P., and Jeng, R.-J. Polythiophenes comprising conjugated pendants for polymer solar cells: A review. *Materials*, 7(4):2411–2439, 2014. ISSN 1996-1944. URL https://doi.org/10.3390/ma7042411.

[24] Scharber, M. and Sariciftci, N. Efficiency of bulk-heterojunction organic solar cells. *Progress in Polymer Science*, 38(12):1929 – 1940, 2013. ISSN 0079-6700. URL https://doi.org/10.1016/j.progpolymsci.2013.05.001. Topical issue on Conductive Polymers.

[25] Meng, L., You, J., and Yang, Y. Addressing the stability issue of perovskite solar cells for commercial applications. *Nature Communications*, 9(1):5265, Dec 2018. ISSN 2041-1723. URL https://doi.org/10.1038/s41467-018-07255-1.

[26] O'Regan, B. and Grätzel, M. A low-cost, high-efficiency solar cell based on dye-sensitized colloidal TiO_2 films. *Nature*, 353(6346):737–740, Oct 1991. ISSN 1476-4687. URL https://doi.org/10.1038/353737a0.

[27] Grätzel, M. Dye-sensitized solar cells. *Journal of Photochemistry and Photobiology C: Photochemistry Reviews*, 4(2):145 – 153, 2003. URL https://doi.org/10.1016/S1389-5567(03)00026-1.

[28] Wikipedia,. Dye-sensitized solar cell, . URL https://en.wikipedia.org/wiki/Dye-sensitized_solar_cell.

[29] James, S. and Contractor, R. Study on Nature-inspired Fractal Design-based Flexible Counter Electrodes for Dye-Sensitized Solar Cells Fabricated using Additive Manufacturing. *Scientific Reports*, 8(1), November 2018. URL https://doi.org/10.1038/s41598-018-35388-2.

[30] Yella, A., Lee, H.-W., Tsao, H. N., Yi, C., Chandiran, A. K., Nazeeruddin, M., Diau, E. W.-G., Yeh, C.-Y., Zakeeruddin, S. M., and Grätzel, M. Porphyrin-Sensitized Solar Cells with Cobalt (ii/iii)–Based Redox Electrolyte Exceed 12 Percent Efficiency. *Science*, 334(6056):629–634, 2011. ISSN 0036-8075. URL https://doi.org/10.1126/science.1209688.

[31] Kojima, A., Teshima, K., Shirai, Y., and Miyasaka, T. Organometal Halide Perovskites as Visible-Light Sensitizers for Photovoltaic cells. *Journal of the American Chemical Society*, 131(17):6050–6051, May 2009. URL https://doi.org/10.1021/ja809598r.

[32] Im, J.-H., Lee, C.-R., Lee, J.-W., Park, S.-W., and Park, N.-G. 6.5% efficient perovskite quantum-dot-sensitized solar cell. *Nanoscale*, 3(10):4088, 2011. URL https://doi.org/10.1039/c1nr10867k.

[33] Kim, H.-S., Lee, C.-R., Im, J.-H., Lee, K.-B., Moehl, T., Marchioro, A., Moon, S.-J., Humphry-Baker, R., Yum, J.-H., Moser, J. E., Grätzel, M., and Park, N.-G. Lead Iodide Perovskite Sensitized All-Solid-State Submicron Thin Film Mesoscopic Solar Cell with Efficiency Exceeding 9%. *Scientific Reports*, 2(1), August 2012. URL https://doi.org/10.1038/srep00591.

[34] Snaith, H. J., Abate, A., Ball, J. M., Eperon, G. E., Leijtens, T., Noel, N. K., Stranks, S. D., Wang, J. T.-W., Wojciechowski, K., and Zhang, W. Anomalous Hysteresis in Perovskite Solar Cells. *The Journal of Physical Chemistry Letters*, 5(9):1511–1515, April 2014. URL https://doi.org/10.1021/jz500113x.

[35] Yoo, J. J., Seo, G., Chua, M. R., Park, T. G., Lu, Y., Rotermund, F., Kim, Y.-K., Moon, C. S., Jeon, N. J., Correa-Baena, J.-P., Bulović, V., Shin, S. S., Bawendi, M. G., and Seo, J. Efficient perovskite solar cells via improved carrier management. *Nature*, 590(7847):587–593, Feb 2021. ISSN 1476-4687. URL https://doi.org/10.1038/s41586-021-03285-w.

[36] NREL,. Best Research-Cell Efficiency Chart, 2020. URL https://www.nrel.gov/pv/cell-efficiency.html.

[37] Jena, A. K., Kulkarni, A., and Miyasaka, T. Halide Perovskite Photovoltaics: Background, Status, and Future Prospects. *Chemical Reviews*, 119(5):3036–3103, Mar 2019. ISSN 0009-2665. URL https://doi.org/10.1021/acs.chemrev.8b00539.

[38] Meng, L., You, J., and Yang, Y. Addressing the stability issue of perovskite solar cells for commercial applications. *Nature Communications*, 9(1), December 2018. URL https://doi.org/10.1038/s41467-018-07255-1.

[39] Kim, J. Y., Lee, J.-W., Jung, H. S., Shin, H., and Park, N.-G. High-Efficiency Perovskite Solar Cells. *Chemical Reviews*, 120(15):7867–7918, July 2020. URL https://doi.org/10.1021/acs.chemrev.0c00107.

[40] Stoumpos, C. C., Malliakas, C. D., and Kanatzidis, M. G. Semiconducting tin and Lead Iodide Perovskites with Organic Cations: Phase Transitions, High Mobilities, and Near-Infrared Photoluminescent Properties. *Inorganic*

Chemistry, 52(15):9019–9038, July 2013. URL https://doi.org/10.1021/ic401215x.

[41] Correa-Baena, J.-P., Abate, A., Saliba, M., Tress, W., Jacobsson, T. J., Grätzel, M., and Hagfeldt, A. The rapid evolution of highly efficient perovskite solar cells. *Energy & Environmental Science*, 10(3):710–727, 2017. URL https://doi.org/10.1039/c6ee03397k.

[42] Jordan, D. C., Silverman, T. J., Wohlgemuth, J. H., Kurtz, S. R., and VanSant, K. T. Photovoltaic failure and degradation modes. *Progress in Photovoltaics: Research and Applications*, 25(4):318–326, 2017. URL https://doi.org/10.1002/pip.2866.

[43] Li, N., Niu, X., Chen, Q., and Zhou, H. Towards commercialization: the operational stability of perovskite solar cells. *Chemical Society Reviews*, 49 (22):8235–8286, 2020. URL https://doi.org/10.1039/d0cs00573h.

[44] Grancini, G., Roldán-Carmona, C., Zimmermann, I., Mosconi, E., Lee, X., Martineau, D., Narbey, S., Oswald, F., Angelis, F. D., Graetzel, M., and Nazeeruddin, M. K. One-Year stable perovskite solar cells by 2d/3d interface engineering. *Nature Communications*, 8(1), jun 2017. URL https://doi.org/10.1038/ncomms15684.

[45] Herz, L. M. Charge-Carrier Mobilities in Metal Halide Perovskites: Fundamental Mechanisms and Limits. *ACS Energy Letters*, 2(7):1539–1548, Jul 2017. URL https://doi.org/10.1021/acsenergylett.7b00276.

[46] Stranks, S. D., Eperon, G. E., Grancini, G., Menelaou, C., Alcocer, M. J. P., Leijtens, T., Herz, L. M., Petrozza, A., and Snaith, H. J. Electron-Hole Diffusion Lengths Exceeding 1 icrometer in an Organometal Trihalide Perovskite bsorber. *Science*, 342(6156):341–344, 2013. ISSN 0036-8075. URL https://doi.org/10.1126/science.1243982.

[47] Wikipedia,. Organic Semiconductor, . URL https://en.wikipedia.org/wiki/Organic_semiconductor.

[48] D.Myers, J. and Xue, J. Organic Semiconductors and their pplications in Photovoltaic Devices. *Polymer Reviews*, 52(1):1–37, 2012. URL https://doi.org/10.1080/15583724.2011.644368.

[49] K.Namsheer, and Rout, C. S. Conducting polymers: a comprehensive review on recent advances in synthesis, properties and applications. *RSC Adv.*, 11: 5659–5697, 2021. URL https://doi.org/10.1039/D0RA07800J.

[50] Trachanas, S., Antonoyiannakis, M., and Tsetseris, L. *An introduction to quantum physics: A first course for physicists, chemists, materials scientists, and engineers*. Wiley-VCH, Weinheim, 2018. ISBN 9783527412471.

[51] Bacon, G. E., Curry, N. A., and Wilson, S. A. A Crystallographic Study of Solid Benzene by Neutron Diffraction. *Proceedings of the Royal Society of London Series A*, 279(1376):98–110, may 1964. URL https://10.1098/rspa.1964.0092.

[52] MccordL,. Molecular Orbitals and the Hydrogen Molecule. URL http://ch301.cm.utexas.edu/imfs/#mo/mo-hydrogen.html.

[53] Molecular orbitals for ethene. URL https://bit.ly/35QUcBd.

[54] The pi-Electron Approximation of Conjugation. URL https://bit.ly/2T66wLd.

[55] Rasmussen, S. C. *Electrically Conducting Plastics: Revising the History of Conjugated rganic Polymers*, volume 1080 of *ACS Symposium Series*, pages 147–163. American Chemical Society, Jan 2011. ISBN 9780841226777. URL https://doi.org/10.1021/bk-2011-1080.ch010. 0.

[56] Shirakawa, H., Louis, E. J., MacDiarmid, A. G., Chiang, C. K., and Heeger, A. J. Synthesis of electrically conducting organic polymers: halogen derivatives of polyacetylene, (ch). *J. Chem. Soc., Chem. Commun.*, pages 578–580, 1977. URL https://doi.org/10.1039/C39770000578.

[57] Prosa, T. J., Winokur, M. J., Moulton, J., Smith, P., and Heeger, A. J. X-ray structural studies of poly(3-alkylthiophenes): an example of an inverse comb. *Macromolecules*, 25(17):4364–4372, Aug 1992. ISSN 0024-9297. URL https://doi.org/10.1021/ma00043a019.

[58] Yu, G. and Heeger, A. Charge separation and photovoltaic conversion in polymer composites with internal donor/acceptor heterojunctions. *Journal of Applied Physics*, 78(7):4510–4515, 1995. doi: 10.1063/1.359792. URL https://doi.org/10.1063/1.359792.

[59] Wikipedia,. Conductive polymer, . URL https://en.wikipedia.org/wiki/Conductive_polymer.

[60] Le, T.-H., Kim, Y., and Yoon, H. Electrical and Electrochemical Properties of Conducting Polymers. *Polymers*, 9(4), 2017. ISSN 2073-4360. URL https://doi.org/10.3390/polym9040150.

[61] Li, G., Chang, W.-H., and Yang, Y. Low-bandgap conjugated polymers enabling solution-processable tandem solar cells. *Nature Reviews Materials*, 2(8):17043, Jul 2017. ISSN 2058-8437. URL https://doi.org/10.1038/natrevmats.2017.43.

[62] Ramanujam, B. and Annamalai, P. K. 1-conducting polymer-graphite binary and hybrid composites: Structure, properties, and applications. In Thakur,

V. K., Thakur, M. K., and Pappu, A., editors, *Hybrid Polymer Composite Materials*, pages 1–34. Woodhead Publishing, 2017. ISBN 978-0-08-100785-3. URL https://doi.org/10.1016/B978-0-08-100785-3.00001-2.

[63] Xiang, Y., Xie, G., Li, Q., Xue, L., Xu, Q., Zhu, J., Tang, Y., Gong, S., Yin, X., and Yang, C. Feasible Modification of PEDOT:PSS by Poly(4-styrenesulfonic acid): A Universal Method to Double the Efficiencies for Solution-Processed Organic Light-Emitting Devices. *ACS Applied Materials & Interfaces*, 11(32):29105–29112, Aug 2019. ISSN 1944-8244. URL https://doi.org/10.1021/acsami.9b09346.

[64] Keene, S. T., van der Pol, T. P. A., Zakhidov, D., Weijtens, C. H. L., Janssen, R. A. J., Salleo, A., and van de Burgt, Y. Enhancement-Mode PEDOT:PSS Organic Electrochemical Transistors Using Molecular De-Doping. *Advanced Materials*, 32(19):2000270, 2020. URL https://doi.org/10.1002/adma.202000270.

[65] Yang, Q., Yu, S., Fu, P., Yu, W., Liu, Y., Liu, X., Feng, Z., Guo, X., and Li, C. Boosting Performance of Non-Fullerene Organic Solar Cells by 2d g-c_3n_4 Doped PEDOT:PSS. *Advanced Functional Materials*, 30(15):1910205, 2020. URL https://doi.org/10.1002/adfm.201910205.

[66] Han, W., Ren, G., Liu, J., Li, Z., Bao, H., Liu, C., and Guo, W. Recent Progress of Inverted Perovskite Solar Cells with a Modified PEDOT:PSS Hole Transport ayer. *ACS Applied Materials & Interfaces*, 12(44):49297–49322, Nov 2020. ISSN 1944-8244. URL https://doi.org/10.1021/acsami.0c13576.

[67] Yu, Y., Peng, S., Blanloeuil, P., Wu, S., and Wang, C. H. Wearable Temperature Sensors with Enhanced Sensitivity by Engineering Microcrack Morphology in PEDOT:PSS-PDMS Sensors. *ACS Applied Materials & Interfaces*, 12(32):36578–36588, Aug 2020. ISSN 1944-8244. URL https://doi.org/10.1021/acsami.0c07649.

[68] Xia, Y. and Dai, S. Review on applications of PEDOTs and PEDOT:PSS in perovskite solar cells. *Journal of Materials Science: Materials in Electronics*, 32(10):12746–12757, May 2021. ISSN 1573-482X. URL https://doi.org/10.1007/s10854-020-03473-w.

[69] Wikipedia,. PEDOT:PSS, . URL https://en.wikipedia.org/wiki/PEDOT:PSS.

[70] Brixi, S., Melville, O. A., Boileau, N. T., and Lessard, B. H. The influence of air and temperature on the performance of PBDB-T and P3HT in organic thin film transistors. *J. Mater. Chem. C*, 6:11972–11979, 2018. URL https://doi.org/10.1039/C8TC00734A.

[71] Holliday, S., Ashraf, R. S., Wadsworth, A., Baran, D., Yousaf, S. A., Nielsen, C. B., Tan, C.-H., Dimitrov, S. D., Shang, Z., Gasparini, N., Alamoudi, M., Laquai, F., Brabec, C. J., Salleo, A., Durrant, J. R., and McCulloch, I. High-efficiency and air-stable P3HT-based polymer solar cells with a new non-fullerene acceptor. *Nature Communications*, 7(1):11585, Jun 2016. ISSN 2041-1723. URL https://doi.org/10.1038/ncomms11585.

[72] Jung, E. H., Jeon, N. J., Park, E. Y., Moon, C. S., Shin, T. J., Yang, T.-Y., Noh, J. H., and Seo, J. Efficient, stable and scalable perovskite solar cells using poly(3-hexylthiophene). *Nature*, 567(7749):511–515, Mar 2019. ISSN 1476-4687. URL https://doi.org/10.1038/s41586-019-1036-3.

[73] Jang, G. N., Hong, S. Y., Park, H., Lee, Y. H., Park, H., Lee, H., Jeong, Y. R., Jin, S. W., Keum, K., and Ha, J. S. Highly sensitive pressure and temperature sensors fabricated with poly(3-hexylthiophene-2,5-diyl)-coated elastic carbon foam for bio-signal monitoring. *Chemical Engineering Journal*, 423:130197, 2021. ISSN 1385-8947. URL https://doi.org/10.1016/j.cej.2021.130197.

[74] Bu, L., Hu, M., Lu, W., Wang, Z., and Lu, G. Printing Semiconductor Insulator Polymer Bilayers for High-Performance Coplanar Field-Effect Transistors. *Advanced Materials*, 30(2):1704695, 2018. URL https://doi.org/10.1002/adma.201704695.

[75] Ossila,. P3HT, . URL https://www.ossila.com/products/p3ht.

[76] Bender, M., Schelkle, K. M., Järgensen, N., Schmid, S., Hernandez-Sosa, G., and Bunz, U. H. F. Photo-Cross-Linkable Polyfluorene-Triarylamine (PF-PTAA) Copolymer Based on the [2 + 2] Cycloaddition Reaction and Its Use as Hole-Transport Layer in OLEDs. *Macromolecules*, 49(8):2957–2961, Apr 2016. ISSN 0024-9297. URL https://doi.org/10.1021/acs.macromol.6b00673.

[77] Panidi, J., Paterson, A. F., Khim, D., Fei, Z., Han, Y., Tsetseris, L., Vourlias, G., Patsalas, P. A., Heeney, M., and Anthopoulos, T. D. Remarkable Enhancement of the Hole Mobility in Several Organic Small-Molecules, Polymers, and Small-Molecule:Polymer Blend Transistors by Simple Admixing of the Lewis Acid p-Dopant b(c_6f_5)$_3$. *Advanced Science*, 5(1):1700290, 2018. URL https://doi.org/10.1002/advs.201700290.

[78] Hawash, Z., Ono, L. K., and Qi, Y. Recent Advances in Spiro-MeOTAD Hole Transport Material and Its Applications in Organic–Inorganic Halide Perovskite Solar Cells. *Advanced Materials Interfaces*, 5(1):1700623, 2018. URL https://doi.org/10.1002/admi.201700623.

[79] Ossila,. PEDOT:PSS, . URL https://www.ossila.com/products/pedot-pss.

[80] Ossila,. P3HT, . URL https://www.ossila.com/products/p3ht.

[81] Aldrich, S. PTAA. URL https://www.sigmaaldrich.com/GR/en/product/aldrich/702471.

[82] Ren, Y., Yang, J.-Q., Zhou, L., Mao, J.-Y., Zhang, S.-R., Zhou, Y., and Han, S.-T. Gate-Tunable Synaptic Plasticity through Controlled Polarity of Charge Trapping in Fullerene Composites. *Advanced Functional Materials*, 28(50):1805599, 2018. URL https://doi.org/10.1002/adfm.201805599.

[83] Qiao, X. and Ma, D. Triplet-triplet annihilation effects in rubrene/c_{60} OLEDs with electroluminescence turn-on breaking the thermodynamic limit. *Nature Communications*, 10(1):4683, Oct 2019. ISSN 2041-1723. URL https://doi.org/10.1038/s41467-019-12597-5.

[84] Saliba, M., Correa-Baena, J.-P., Wolff, C. M., Stolterfoht, M., Phung, N., Albrecht, S., Neher, D., and Abate, A. How to make over 20% efficient perovskite solar cells in regular (n-i-p) and inverted (p-i-n) architectures. *Chemistry of Materials*, 30(13):4193–4201, Jul 2018. ISSN 0897-4756. URL https://doi.org/10.1021/acs.chemmater.8b00136.

[85] Wikipedia,. Phenyl-C61-butyric acid methyl ester, . URL https://en.wikipedia.org/wiki/Phenyl-C61-butyric_acid_methyl_ester.

[86] Novoselov, K. S., Geim, A. K., Morozov, S. V., Jiang, D., Zhang, Y., Dubonos, S. V., Grigorieva, I. V., and Firsov, A. A. Electric field effect in atomically thin carbon films. *Science*, 306(5696):666–669, 2004. ISSN 0036-8075. doi: 6. URL https://10.1126/science.1102896.

[87] Wikipedia,. Graphene Structure, . URL https://en.wikipedia.org/wiki/Pi-Stacking_(chemistry).

[88] Atta, N. F., Galal, A., and El-Ads, E. H. Graphene-A Platform for Sensor and Biosensor Applications. In Rinken, T., editor, *Biosensors*, chapter 2. IntechOpen, Rijeka, 2015. URL https://doi.org/10.5772/60676.

[89] Wikipedia,. Graphene Structure, . URL https://commons.wikimedia.org/wiki/File:Graphene_structure.svg.

[90] Wikipedia,. Perovskite (structure), . URL https://en.wikipedia.org/wiki/Perovskite_(structure).

[91] Peña, M. A. and Fierro, J. L. G. Chemical Structures and Performance of Perovskite Oxides. *Chemical Reviews*, 101(7):1981–2018, Jul 2001. ISSN 0009-2665. URL https://doi.org/10.1021/cr980129f.

[92] Goldschmidt, V. M. Die gesetze der krystallochemie. *Naturwissenschaften*, 14(21):477–485, May 1926. ISSN 1432-1904. URL https://doi.org/10.1007/BF01507527.

[93] Li, Z., Yang, M., Park, J.-S., Wei, S.-H., Berry, J. J., and Zhu, K. Stabilizing Perovskite Structures by Tuning Tolerance Factor: Formation of Formamidinium and Cesium Lead Iodide Solid-State Alloys. *Chemistry of Materials*, 28(1):284–292, Jan 2016. ISSN 0897-4756. URL https://doi.org/10.1021/acs.chemmater.5b04107.

[94] Bu, T., Liu, X., Zhou, Y., Yi, J., Huang, X., Luo, L., Xiao, J., Ku, Z., Peng, Y., Huang, F., Cheng, Y.-B., and Zhong, J. A novel quadruple-cation absorber for universal hysteresis elimination for high efficiency and stable perovskite solar cells. *Energy Environ. Sci.*, 10:2509–2515, 2017. URL https://doi.org/10.1039/C7EE02634J.

[95] Ossila,. Perovskites and Perovskite Solar Cells: An Introduction, . URL https://bit.ly/381Emor.

[96] Kim, B., Kim, J., and Park, N. First-principles identification of the charge-shifting mechanism and ferroelectricity in hybrid halide perovskites. *Scientific Reports*, 10(1):19635, Nov 2020. ISSN 2045-2322. URL https://doi.org/10.1038/s41598-020-76742-7.

[97] Kim, B., Kim, J., and Park, N. First-principles identification of the charge-shifting mechanism and ferroelectricity in hybrid halide perovskites. *Scientific Reports*, 10(1):19635, Nov 2020. ISSN 2045-2322. URL https://doi.org/10.1038/s41598-020-76742-7.

[98] Zhou, G., Wu, J., Zhao, Y., Li, Y., Shi, J., Li, Y., Wu, H., Li, D., Luo, Y., and Meng, Q. Application ofCesium on the Restriction of Precursor Crystallization for Highly Reproducible Perovskite Solar Cells Exceeding 20% fficiency. *ACS Applied Materials & Interfaces*, 10(11):9503–9513, February 2018. URL https://doi.org/10.1021/acsami.8b01054.

[99] Stoumpos, C. C. and Kanatzidis, M. G. Halide Perovskites: Poor Man's High-Performance Semiconductors. *Advanced Materials*, 28(28):5778–5793, 2016. URL https://doi.org/10.1002/adma.201600265.

[100] Hsiao, Y.-C., Wu, T., Li, M., Liu, Q., Qin, W., and Hu, B. Fundamental physics behind high-efficiency organo-metal halide perovskite solar cells. *J. Mater. Chem. A*, 3:15372–15385, 2015. doi: https://10.1039/C5TA01376C.

[101] Fujiwara, H., Kato, M., Tamakoshi, M., Miyadera, T., and Chikamatsu, M. Optical Characteristics and Operational Principles of Hybrid Perovskite Solar Cells. *physica status solidi (a)*, 215(12):1700730, 2018. URL https://doi.org/10.1002/pssa.201700730.

[102] Giorgi, G., Fujisawa, J.-I., Segawa, H., and Yamashita, K. Small Photocarrier Effective Masses Featuring Ambipolar Transport in Methylammonium Lead Iodide Perovskite: A Density Functional Analysis. *The Journal of Physical Chemistry Letters*, 4(24):4213–4216, Dec 2013. URL https://doi.org/10.1021/jz4023865.

[103] Herz, L. M. Charge-Carrier Mobilities in Metal Halide Perovskites: Fundamental Mechanisms and Limits. *ACS Energy Letters*, 2(7):1539–1548, Jul 2017. URL https://doi.org/10.1021/acsenergylett.7b00276.

[104] Peng, J., Chen, Y., Zheng, K., Pullerits, T., and Liang, Z. Insights into charge carrier dynamics in organo-metal halide perovskites: from neat films to solar cells. *Chem. Soc. Rev.*, 46:5714–5729, 2017. URL https://.doi.org/10.1039/C6CS00942E.

[105] Xiao, M., Huang, F., Huang, W., Dkhissi, Y., Zhu, Y., Etheridge, J., Gray-Weale, A., Bach, U., Cheng, Y.-B., and Spiccia, L. A Fast Deposition-Crystallization Procedure for Highly Efficient Lead Iodide Perovskite Thin-Film Solar Cells. *Angewandte Chemie International Edition*, 53(37):9898–9903, 2014. URL https://doi.org/10.1002/anie.201405334.

[106] Jung, M., Ji, S.-G., Kim, G., and Seok, S. I. Perovskite precursor solution chemistry: from fundamentals to photovoltaic applications. *Chem. Soc. Rev.*, 48:2011–2038, 2019. URL https://doi.org/10.1039/C8CS00656C.

[107] Yoo, J. J., Seo, G., Chua, M. R., Park, T. G., Lu, Y., Rotermund, F., Kim, Y.-K., Moon, C. S., Jeon, N. J., Correa-Baena, J.-P., Bulović, V., Shin, S. S., Bawendi, M. G., and Seo, J. Efficient perovskite solar cells via improved carrier management. *Nature*, 590(7847):587–593, Feb 2021. ISSN 1476-4687. URL https://doi.org/10.1038/s41586-021-03285-w.

[108] Hole Transport Materials in Conventional Structural (n-i-p) Perovskite Solar Cells: From Past to the Future. *Advanced Energy Materials*, 10(8):1903403, 2020. URL https://doi.org/10.1002/aenm.201903403.

[109] Hawash, Z., Ono, L. K., and Qi, Y. Moisture and Oxygen Enhance Conductivity of LiTFSI-Doped Spiro-MeOTAD Hole Transport Layer in Perovskite Solar Cells. *Advanced Materials Interfaces*, 3(13):1600117, 2016. URL https://doi.org/10.1002/admi.201600117.

[110] Meng, L., You, J., Guo, T.-F., and Yang, Y. Recent Advances in the Inverted Planar Structure of Perovskite Solar Cells. *Accounts of Chemical Research*, 49(1):155–165, Jan 2016. ISSN 0001-4842. URL https://doi.org/10.1021/acs.accounts.5b00404.

[111] Zheng, X., Hou, Y., Bao, C., Yin, J., Yuan, F., Huang, Z., Song, K., Liu, J., Troughton, J., Gasparini, N., Zhou, C., Lin, Y., Xue, D.-J., Chen, B., Johnston, A. K., Wei, N., Hedhili, M. N., Wei, M., Alsalloum, A. Y., Maity, P., Turedi, B., Yang, C., Baran, D., Anthopoulos, T. D., Han, Y., Lu, Z.-H., Mohammed, O. F., Gao, F., Sargent, E. H., and Bakr, O. M. Managing grains and interfaces via ligand anchoring enables 22.3%-efficiency inverted perovskite solar cells. *Nature Energy*, 5(2):131–140, Feb 2020. ISSN 2058-7546. URL https://doi.org/10.1038/s41560-019-0538-4.

[112] Wu, S., Zhang, J., Li, Z., Liu, D., Qin, M., Cheung, S., Lu, X., Lei, D., So, S., Zhu, Z., and Jen, A.-Y. Modulation of Defects and Interfaces through Alkylammonium Interlayer for Efficient Inverted Perovskite Solar Cells. *Joule*, 4, 04 2020. URL https://doi.org/10.1016/j.joule.2020.04.001.

[113] Li, F., Deng, X., Qi, F., Li, Z., Liu, D., Shen, D., Qin, M., Wu, S., Lin, F., Jang, S.-H., Zhang, J., Lu, X., Lei, D., Lee, C.-S., Zhu, Z., and Jen, A. K.-Y. Regulating Surface Termination for Efficient Inverted Perovskite Solar Cells with Greater Than 23% Efficiency. *Journal of the American Chemical Society*, 142(47):20134–20142, Nov 2020. ISSN 0002-7863. URL https://doi.org/10.1021/jacs.0c09845.

[114] Alsalloum, A. Y., Turedi, B., Zheng, X., Mitra, S., Zhumekenov, A. A., Lee, K. J., Maity, P., Gereige, I., AlSaggaf, A., Roqan, I. S., Mohammed, O. F., and Bakr, O. M. Low-Temperature Crystallization Enables 21.9% Efficient Single-Crystal $mapbi_3$ Inverted Perovskite Solar Cells. *ACS Energy Letters*, 5(2):657–662, Feb 2020. URL https://doi.org/10.1021/acsenergylett.9b02787.

[115] Saliba, M., Correa-Baena, J.-P., Wolff, C. M., Stolterfoht, M., Phung, N., Albrecht, S., Neher, D., and Abate, A. How to make over 20% efficient perovskite solar cells in regular (n-i-p) and inverted (p-i-n) architectures. *Chemistry of Materials*, 30(13):4193–4201, Jul 2018. ISSN 0897-4756. URL https://doi.org/10.1021/acs.chemmater.8b00136.

[116] Snaith, H. J., Abate, A., Ball, J. M., Eperon, G. E., Leijtens, T., Noel, N. K., Stranks, S. D., Wang, J. T.-W., Wojciechowski, K., and Zhang, W. Anomalous Hysteresis in Perovskite Solar Cells. *The Journal of Physical Chemistry Letters*, 5(9):1511–1515, May 2014. URL https://doi.org/10.1021/jz500113x.

[117] Kang, D.-H. and Park, N.-G. On the Current-Voltage Hysteresis in Perovskite Solar Cells: Dependence on Perovskite Composition and Methods to Remove Hysteresis. *Advanced Materials*, 31(34):1805214, 2019. URL https://doi.org/10.1002/adma.201805214.

[118] Kang, D.-H. and Park, N.-G. On the Current-Voltage Hysteresis in Perovskite Solar Cells: Dependence on Perovskite Composition and Methods to Remove

Hysteresis. *Advanced Materials*, 31(34):1805214, 2019. URL https://doi.org/10.1002/adma.201805214.

[119] Zhou, H., Chen, Q., Li, G., Luo, S., Song, T.-b., Duan, H.-S., Hong, Z., You, J., Liu, Y., and Yang, Y. Interface engineering of highly efficient perovskite solar cells. *Science*, 345(6196):542–546, 2014. ISSN 0036-8075. URL https://doi.org/10.1126/science.1254050.

[120] Shibayama, N., Kanda, H., Kim, T. W., Segawa, H., and Ito, S. Design of BCP buffer layer for inverted perovskite solar cells using ideal factor. 7(3): 031117, March 2019. URL https://doi.org/10.1063/1.5087796.

[121] Park, I., Park, M., Kim, D., Park, G., Kim, B., Son, H., Ko, M., Lee, D., Park, T., Shin, H., Park, N., Jung, H., and Kim, J. New Hybrid Hole Extraction Layer of Perovskite Solar Cells with a Planar p-i-n Geometry. *Journal of Physical Chemistry C*, 119(49):27285–27290, dec 2015. ISSN 1932-7447. URL https://doi.org/10.1021/acs.jpcc.5b09322.

[122] Li, Y., Zhao, Y., Chen, Q., Yang, Y. M., Liu, Y., Hong, Z., Liu, Z., Hsieh, Y.-T., Meng, L., Li, Y., and Yang, Y. Multifunctional Fullerene Derivative for Interface Engineering in Perovskite Solar Cells. *Journal of the American Chemical Society*, 137(49):15540–15547, Dec 2015. ISSN 0002-7863. URL https://doi.org/10.1021/jacs.5b10614.

[123] Bai, Y., Meng, X., and Yang, S. Interface Engineering for Highly Efficient and Stable Planar p-i-n Perovskite Solar Cells. *Advanced Energy Materials*, 8(5):1701883, 2018. URL https://doi.org/10.1002/aenm.201701883.

[124] Son, D.-Y., Kim, S.-G., Seo, J.-Y., Lee, S.-H., Shin, H., Lee, D., and Park, N.-G. Universal Approach toward Hysteresis-Free Perovskite Solar Cell via Defect Engineering. *Journal of the American Chemical Society*, 140(4): 1358–1364, Jan 2018. ISSN 0002-7863. URL https://doi.org/10.1021/jacs.7b10430.

[125] Min, H., Kim, M., Lee, S.-U., Kim, H., Kim, G., Choi, K., Lee, J. H., and Seok, S. I. Efficient,stable solar cells by using inherent bandgap of α-phase formamidinium lead iodide. *Science*, 366(6466):749–753, November 2019. URL https://doi.org/10.1126/science.aay7044.

[126] Gao, F., Zhao, Y., Zhang, X., and You, J. Recent Progresses on Defect Passivation toward Efficient Perovskite Solar Cells. *Advanced Energy Materials*, 10(13):1902650, 2020. URL https://doi.org/10.1002/aenm.201902650.

[127] Jiang, Q., Zhao, Y., Zhang, X., Yang, X., Chen, Y., Chu, Z., Ye, Q., Li, X., Yin, Z., and You, J. Surface passivation of perovskite film for efficient solar cells. *Nature Photonics*, 13:1, 07 2019. URL https://doi.org/10.1038/s41566-019-0398-2.

[128] Jošt, M., Kegelmann, L., Korte, L., and Albrecht, S. Monolithic Perovskite Tandem Solar Cells: A Review of the Present Status and Advanced Characterization Methods Toward 30% Efficiency. *Advanced Energy Materials*, 10 (26):1904102, 2020. URL https://doi.org/10.1002/aenm.201904102.

[129] Isikgor, F. H., Furlan, F., Liu, J., Ugur, E., Eswaran, M. K., Subbiah, A. S., Yengel, E., De Bastiani, M., Harrison, G. T., Zhumagali, S., Howells, C. T., Aydin, E., Wang, M., Gasparini, N., Allen, T. G., ur Rehman, A., Van Kerschaver, E., Baran, D., McCulloch, I., Anthopoulos, T. D., Schwingenschögl, U., Laquai, F., and De Wolf, S. Concurrent cationic and anionic perovskite defect passivation enables 27.4% perovskite/silicon tandems with suppression of halide segregation. *Joule*, 5(6):1566–1586, 2021. ISSN 2542-4351. URL https://doi.org/10.1016/j.joule.2021.05.013.

[130] Al-Ashouri, A., Köhnen, E., Li, B., Magomedov, A., Hempel, H., Caprioglio, P., Márquez, J. A., Morales Vilches, A. B., Kasparavicius, E., Smith, J. A., Phung, N., Menzel, D., Grischek, M., Kegelmann, L., Skroblin, D., Gollwitzer, C., Malinauskas, T., Jošt, M., Matič, G., Rech, B., Schlatmann, R., Topič, M., Korte, L., Abate, A., Stannowski, B., Neher, D., Stolterfoht, M., Unold, T., Getautis, V., and Albrecht, S. Monolithic perovskite/silicon tandem solar cell with >29% efficiency by enhanced hole extraction. *Science*, 370 (6522):1300–1309, 2020. ISSN 0036-8075. URL https://doi.org/10.1126/science.abd4016.

[131] Han, G., Hadi, H. D., Bruno, A., Kulkarni, S. A., Koh, T. M., Wong, L. H., Soci, C., Mathews, N., Zhang, S., and Mhaisalkar, S. G. Additive Selection Strategy for High Performance Perovskite Photovoltaics. *The Journal of Physical Chemistry C*, 122(25):13884–13893, Jun 2018. ISSN 1932-7447. URL https://doi.org/10.1021/acs.jpcc.8b00980.

[132] Eames, C., Frost, J. M., Barnes, P. R. F., O'Regan, B. C., Walsh, A., and Islam, M. S. Ionic transport in hybrid lead iodide perovskite solar cells. *Nature Communications*, 6(1):7497, Jun 2015. ISSN 2041-1723. URL https://doi.org/10.1038/ncomms8497.

[133] Yuan, Y., Wang, Q., Shao, Y., Lu, H., Li, T., Gruverman, A., and Huang, J. Electric-Field-Driven Reversible Conversion Between Methylammonium Lead Triiodide Perovskites and Lead Iodide at Elevated Temperatures. *Advanced Energy Materials*, 6(2):1501803, 2016. URL https://doi.org/10.1002/aenm.201501803.

[134] Wu, T., Ahmadi, M., and Hu, B. Giant current amplification induced by ion migration in perovskite single crystal photodetectors. *J. Mater. Chem. C*, 6: 8042–8050, 2018. URL https://doi.org/10.1039/C8TC02334D.

[135] Luo, Y., Khoram, P., Brittman, S., Zhu, Z., Lai, B., Ong, S. P., Garnett, E. C., and Fenning, D. P. Direct Observation of Halide Migration and its Effect on the Photoluminescence of Methylammonium Lead Bromide Perovskite Single Crystals. *Advanced Materials*, 29(43):1703451, 2017. URL https://doi.org/10.1002/adma.201703451.

[136] Zhao, J., Deng, Y., Wei, H., Zheng, X., Yu, Z., Shao, Y., Shield, J. E., and Huang, J. Strained hybrid perovskite thin films and their impact on the intrinsic stability of perovskite solar cells. *Science Advances*, 3 (11), 2017. doi: 10.1126/sciadv.aao5616. URL https://doi.org/10.1126/sciadv.aao5616.

[137] Rolston, N., Bush, K. A., Printz, A. D., Gold-Parker, A., Ding, Y., Toney, M. F., McGehee, M. D., and Dauskardt, R. H. Engineering Stress in Perovskite Solar Cells to Improve Stability. *Advanced Energy Materials*, 8(29): 1802139, 2018. URL https://doi.org/10.1002/aenm.201802139.

[138] Strelcov, E., Dong, Q., Li, T., Chae, J., Shao, Y., Deng, Y., Gruverman, A., Huang, J., and Centrone, A. $CH_3NH_3PbI_3$ perovskites: Ferroelasticity revealed. *Science Advances*, 3(4), 2017. URL https://doi.org/10.1126/sciadv.1602165.

[139] Lv, Q., He, W., Lian, Z., Ding, J., Li, Q., and Yan, Q. Anisotropic moisture erosion of $CH_3NH_3PbI_3$ single crystals. *CrystEngComm*, 19:901–904, 2017. doi: 10.1039/C6CE02317G. URL https://doi.org/10.1039/C6CE02317G.

[140] Habisreutinger, S. N., Leijtens, T., Eperon, G. E., Stranks, S. D., Nicholas, R. J., and Snaith, H. J. Carbon Nanotube/Polymer Composites as a Highly Stable Hole Collection Layer in Perovskite Solar Cells. *Nano Letters*, 14(10): 5561–5568, Oct 2014. ISSN 1530-6984. URL https://doi.org/10.1021/nl501982b.

[141] Chaudhary, B., Kulkarni, A., Jena, A. K., Ikegami, M., Udagawa, Y., Kunugita, H., Ema, K., and Miyasaka, T. Poly(4-Vinylpyridine)-Based Interfacial Passivation to Enhance Voltage and Moisture Stability of Lead Halide Perovskite Solar Cells. *ChemSusChem*, 10(11):2473–2479, 2017. URL https://doi.org/10.1002/cssc.201700271.

[142] Abdelmageed, G., Sully, H. R., Bonabi Naghadeh, S., El-Hag Ali, A., Carter, S. A., and Zhang, J. Z. Improved Stability of Organometal Halide Perovskite Films and Solar Cells toward Humidity via Surface Passivation with Oleic Acid. *ACS Applied Energy Materials*, 1(2):387–392, Feb 2018. URL https://doi.org/10.1021/acsaem.7b00069.

[143] Fang, H.-H., Adjokatse, S., Wei, H., Yang, J., Blake, G. R., Huang, J., Even, J., and Loi, M. A. Ultrahigh sensitivity of methylammonium lead tribromide

perovskite single crystals to environmental gases. *Science Advances*, 2(7), 2016. URL https://doi.org/10.1126/sciadv.1600534.

[144] Zohar, A., Kedem, N., Levine, I., Zohar, D., Vilan, A., Ehre, D., Hodes, G., and Cahen, D. Impedance Spectroscopic Indication for Solid State Electrochemical Reaction in $(ch_3nh_3)pbi_3$ Films. *The Journal of Physical Chemistry Letters*, 7(1):191–197, Jan 2016. URL https://doi.org/10.1021/acs.jpclett.5b02618.

[145] Leijtens, T., Eperon, G. E., Pathak, S., Abate, A., Lee, M. M., and Snaith, H. J. Overcoming ultraviolet light instability of sensitized TiO_2 with meso-superstructured organometal tri-halide perovskite solar cells. *Nature Communications*, 4(1):2885, Dec 2013. ISSN 2041-1723. URL https://doi.org/10.1038/ncomms3885.

[146] Hoke, E. T., Slotcavage, D. J., Dohner, E. R., Bowring, A. R., Karunadasa, H. I., and McGehee, M. D. Reversible photo-induced trap formation in mixed-halide hybrid perovskites for photovoltaics. *Chem. Sci.*, 6:613–617, 2015. doi: 10.1039/C4SC03141E. URL https://doi.org/10.1039/C4SC03141E.

[147] Roose, B., Wang, Q., and Abate, A. The Role of Charge Selective Contacts in Perovskite Solar Cell Stability. *Advanced Energy Materials*, 9(5):1803140, 2019. URL https://doi.org/10.1002/aenm.201803140.

[148] Kato, Y., Ono, L. K., Lee, M. V., Wang, S., Raga, S. R., and Qi, Y. Silver Iodide Formation in Methyl Ammonium Lead Iodide Perovskite Solar Cells with Silver Top Electrodes. *Advanced Materials Interfaces*, 2(13):1500195, 2015. URL https://doi.org/10.1002/admi.201500195.

[149] Han, G., Hadi, H. D., Bruno, A., Kulkarni, S. A., Koh, T. M., Wong, L. H., Soci, C., Mathews, N., Zhang, S., and Mhaisalkar, S. G. Additive Selection Strategy for High Performance Perovskite Photovoltaics. *The Journal of Physical Chemistry C*, 122(25):13884–13893, Jun 2018. ISSN 1932-7447. URL https://doi.org/10.1021/acs.jpcc.8b00980.

[150] Habisreutinger, S. N., Leijtens, T., Eperon, G. E., Stranks, S. D., Nicholas, R. J., and Snaith, H. J. Carbon nanotube/polymer composites as a highly stable hole collection layer in perovskite solar cells. *Nano Letters*, 14(10): 5561–5568, Oct 2014. ISSN 1530-6984. URL https://doi.org/10.1021/nl501982b.

[151] Ossila,. Contact Angle: A Guide to Theory and Measurement, . URL https://www.ossila.com/pages/contact-angle-theory-measurement.

[152] Wikipedia,. Surface tension, . URL https://en.wikipedia.org/wiki/Surface_tension.

[153] Nano, and GMBH, M. What is Atomic Force Microscopy (AFM). URL https://www.nanoandmore.com/what-is-atomic-force-microscopy.

[154] Pavan M. V. Raja & Andrew R. Barron, C. L. T. Uv-Visible Spectroscopy. URL https://bit.ly/3k3RQrd.

[155] Yuan, F., Li, Z., Zhang, T., Miao, W., and Zhang, Z. Enhanced light absorption of amorphous silicon thin film by substrate control and ion irradiation. *Nanoscale research letters*, 9:173, 04 2014. doi: https://doi.org/10.1186/1556-276X-9-173.

[156] Zanatta, A. R. Revisiting the optical bandgap of semiconductors and the proposal of a unified methodology to its determination. *Scientific Reports*, 9(1):11225, Aug 2019. ISSN 2045-2322. URL https://doi.org/10.1038/s41598-019-47670-y.

[157] DeNovix,. Smartpath and High absorbance. URL https://bit.ly/3wueLyb.

[158] Macfarlane, G. G., McLean, T. P., Quarrington, J. E., and Roberts, V. Fine Structure in the Absorption-Edge Spectrum of Si. *Physical Review*, 111 (5):1245–1254, September 1958. URL https://doi.org/10.1103/physrev.111.1245.

[159] Huang, B., Fu, Q., Ai, Q., Tan, L., Chen, L., and Chen, Y. Optimization of perovskite by 3D twisted diketopyrrolopyrrole for efficient perovskite solar cells. *Mater. Chem. Front.*, 1:1179–1184, 2017. URL https://doi.org/10.1039/C6QM00210B.

[160] Graham, D. J. What is Cyclic Voltammetry?, . URL https://sop4cv.com/chapters/WhatIsCyclicVoltammetry.html.

[161] Elgrishi, N., Rountree, K. J., McCarthy, B. D., Rountree, E. S., Eisenhart, T. T., and Dempsey, J. L. A Practical Beginner's Guide to Cyclic Voltammetry. *Journal of Chemical Education*, 95(2):197–206, Feb 2018. ISSN 0021-9584. URL https://doi.org/10.1021/acs.jchemed.7b00361.

[162] Graham, D. J. Cyclic Voltammetry:Basic Principles % setup, . URL https://sop4cv.com/.

[163] McEwen, J. Jablonski Diagram, August 2020. URL https://bit.ly/3koGpKO.

[164] Wikipedia,. Quenching (fluorescence), . URL https://en.wikipedia.org/wiki/Quenching_(fluorescence).

[165] Ossila,. Perovskite Solar Cells:Passivation techniques, . URL https://www.ossila.com/pages/perovskite-solar-cells-passivation-techniques.

[166] Fox, M. *Optical properties of solids*. Oxford University Press, Oxford New York, 2010. ISBN 9780199573370.

[167] Instruments, E. TCSPC - What is Time-Correlated Single Photon Counting? URL https://www.edinst.com/blog/what-is-tcspc/.

[168] Zhang, Y., Kou, C., Zhang, J., Liu, Y., Li, W., Bo, Z., and Shao, M. Crosslinked and dopant free hole transport materials for efficient and stable planar perovskite solar cells. *J. Mater. Chem. A*, 7:5522–5529, 2019. URL https://doi.org/10.1039/C8TA12060A.

[169] Ibrahim Dar, M., Abdi-Jalebi, M., Arora, N., Moehl, T., Grätzel, M., and Nazeeruddin, M. K. Understanding the Impact of Bromide on the Photovoltaic Performance of $CH_3NH_3PbI_3$ Solar Cells. *Advanced Materials*, 27 (44):7221–7228, 2015. URL https://doi.org/10.1002/adma.201503124.

[170] Zhang, F., Huang, Q., Song, J., Zhang, Y., Ding, C., Liu, F., Liu, D., Li, X., Yasuda, H., Yoshida, K., Qu, J., Hayase, S., Toyoda, T., Minemoto, T., and Shen, Q. Growth of Amorphous Passivation Layer Using Phenethylammonium Iodide for High-Performance Inverted Perovskite Solar Cells. *Solar RRL*, 4 (2):1900243, 2020. URL https://doi.org/10.1002/solr.201900243.

[171] Si, H., Liao, Q., Kang, Z., Ou, Y., Meng, J., Liu, Y., Zhang, Z., and Zhang, Y. Deciphering the NH_4PbI_3 Intermediate Phase for Simultaneous Improvement on Nucleation and Crystal Growth of Perovskite. *Advanced Functional Materials*, 27(30):1701804, 2017. URL https://doi.org/10.1002/adfm.201701804.

[172] Kirchartz, T., Mrquez, J. A., Stolterfoht, M., and Unold, T. Photoluminescence-Based Characterization of Halide Perovskites for Photovoltaics. *Advanced Energy Materials*, 10(26):1904134, 2020. URL https://doi.org/10.1002/aenm.201904134.

[173] Resolved Fluorescence Wiki, T. Pile-up effect. URL https://www.tcspc.com/doku.php/glossary:pile-up_effect.

[174] Lorchat, E., Lpez, L. E. P., Robert, C., Lagarde, D., Froehlicher, G., Taniguchi, T., Watanabe, K., Marie, X., and Berciaud, S. Filtering the photoluminescence spectra of atomically thin semiconductors with graphene. *Nature Nanotechnology*, 15(4):283–288, Apr 2020. ISSN 1748-3395. URL https://doi.org/10.1038/s41565-020-0644-2.

[175] Krockemeier, L., Krogmeier, B., Liu, Z., Rau, U., and Kirchartz, T. Understanding Transient Photoluminescence in Halide Perovskite Layer Stacks and Solar Cells. *Advanced Energy Materials*, 11(19):2003489, 2021. URL https://doi.org/10.1002/aenm.202003489.

[176] PVEducation,. Fill Factor. URL https://bit.ly/3Di8r1E.

[177] Esen, V., Şafak Sağlam,, and Oral, B. Light sources of solar simulators for photovoltaic devices: A review. *Renewable and Sustainable Energy Reviews*, 77:1240–1250, 2017. ISSN 1364-0321. URL https://doi.org/10.1016/j.rser.2017.03.062.

[178] Wikipedia,. Air mass (solar energy), . URL https://en.wikipedia.org/wiki/Air_mass_(solar_energy).

[179] Ossila,. Solar Cells: A Guide to Theory and Measurement, . URL https://www.ossila.com/pages/solar-cells-theory.

[180] Köntges, M., Kurtz, S., Packard, C., Jahn, U., Berger, K., Kato, K., Friesen, T., Liu, H., Van Iseghem, M., Wohlgemuth, j., Miller, D., Kempe, M., Hacke, P., Reil, F., Bogdanski, N., Herrmann, W., Buerhop, C., Razongles, G., and Friesen, G. Review of failures of photovoltaic modules, 01 2014.

[181] Stolterfoht, M., Wolff, C. M., Márquez, J. A., Zhang, S., Hages, C. J., Rothhardt, D., Albrecht, S., Burn, P. L., Meredith, P., Unold, T., and Neher, D. Visualization and suppression of interfacial recombination for high-efficiency large-area pin perovskite solar cells. *Nature Energy*, 3(10): 847–854, Oct 2018. ISSN 2058-7546. URL https://doi.org/10.1038/s41560-018-0219-8.

[182] Qiu, F., Chu, J., Liu, Z., Xiang, J., Yang, J., and Wang, C. Insight into the Origins of Figures of Merit and Design Strategies for Organic/Inorganic Lead-Halide Perovskite Solar Cells. *Solar RRL*, 4(12):2000452, 2020. URL https://doi.org/10.1002/solr.202000452.

[183] TUDelft,. EQE – Purpose and Setup. URL https://ocw.tudelft.nl/course-lectures/eqe-prupose-and-setup/.

[184] PVEducation,. Quantum Efficiency. URL https://www.pveducation.org/pvcdrom/solar-cell-operation/quantum-efficiency.

[185] Rhr, J. A., Moia, D., Haque, S. A., Kirchartz, T., and Nelson, J. Exploring the validity and limitations of the Mott–Gurney law for charge-carrier mobility determination of semiconducting thin-films. *Journal of Physics: Condensed Matter*, 30(10):105901, feb 2018. URL https://doi.org/10.1088/1361-648x/aaabad.

[186] Murgatroyd, P. N. Theory of space-charge-limited current enhanced by Frenkel effect. *Journal of Physics D: Applied Physics*, 3(2):151–156, feb 1970. URL https://doi.org/10.1088/0022-3727/3/2/308.

[187] Bube, R. H. Trap Density Determination by Space Charge Limited Currents. *Journal of Applied Physics*, 33(5):1733–1737, 1962. URL https://doi.org/10.1063/1.1728818.

[188] Petrovic, M., Maksudov, T., Panagiotopoulos, A., Serpetzoglou, E., Konidakis, I., Stylianakis, M. M., Stratakis, E., and Kymakis, E. Limitations of a polymer-based hole transporting layer for application in planar inverted perovskite solar cells. *Nanoscale Adv.*, 1:3107–3118, 2019. URL https://doi.org/10.1039/C9NA00246D.

[189] Li, R., Wang, P., Chen, B., Cui, X., Ding, Y., Li, Y., Zhang, D., Zhao, Y., and Zhang, X. Niox/Spiro Hole Transport Bilayers for stable Perovskite solar Cells with Efficiency Exceeding 21%. *ACS Energy Letters*, 5(1):79–86, Jan 2020. URL https://doi.org/10.1021/acsenergylett.9b02112.

[190] Kumar, V., Jain, S. C., Kapoor, A. K., Poortmans, J., and Mertens, R. Trap density in conducting organic semiconductors determined from temperature dependence of J-V characteristics. *Journal of Applied Physics*, 94(2):1283–1285, 2003. URL https://doi.org/10.1063/1.1582552.

[191] Zhang, L. *Device physics of perovskite solar cells*. PhD thesis. URL https://doi.org/10.31274/etd-180810-5932.

[192] Shi, D., Adinolfi, V., Comin, R., Yuan, M., Alarousu, E., Buin, A., Chen, Y., Hoogland, S., Rothenberger, A., Katsiev, K., Losovyj, Y., Zhang, X., Dowben, P. A., Mohammed, O. F., Sargent, E. H., and Bakr, O. M. Low trap-state density and long carrier diffusion in organolead trihalide perovskite single crystals. *Science*, 347(6221):519–522, January 2015. URL https://doi.org/10.1126/science.aaa2725.

[193] Li, Y., Shi, J., Yu, B., Duan, B., Wu, J., Li, H., Li, D., Luo, Y., Wu, H., and Meng, Q. Exploiting Electrical Transients to Quantify Charge Loss in Solar Cells. *Joule*, 4(2):472–489, 2020. ISSN 2542-4351. URL https://doi.org/10.1016/j.joule.2019.12.016.

[194] Palomares, E., Montcada, N. F., Mendez, M., Jimenez-Lopez, J., Yang, W., and Boschloo, G. Photovoltage/photocurrent transient techniques. In Pazoki, M., Hagfeldt, A., and Edvinsson, T., editors, *Characterization Techniques for Perovskite Solar Cell Materials*, Micro and Nano Technologies, pages 161–180. Elsevier, 2020. ISBN 978-0-12-814727-6. URL https://doi.org/10.1016/B978-0-12-814727-6.00007-4.

[195] Sandberg, O. J., Tvingstedt, K., Meredith, P., and Armin, A. Theoretical Perspective on Transient Photovoltage and Charge Extraction Techniques. *The Journal of Physical Chemistry C*, 123(23):14261–14271, Jun 2019. ISSN 1932-7447. URL https://doi.org/10.1021/acs.jpcc.9b03133.

[196] Yaghoobi Nia, N., Méndez, M., Paci, B., Generosi, A., Di Carlo, A., and Palomares, E. Analysis of the Efficiency Losses in Hybrid Perovskite/PTAA Solar Cells with Different Molecular Weights: Morphology versus Kinetics. *ACS Applied Energy Materials*, 3(7):6853–6859, Jul 2020. URL https://doi.org/10.1021/acsaem.0c00956.

[197] Tsikritzis, D., Rogdakis, K., Chatzimanolis, K., Petrović, M., Tzoganakis, N., Najafi, L., Martín-García, B., Oropesa-Nuñez, R., Bellani, S., Del Rio Castillo, A. E., Prato, M., Stylianakis, M. M., Bonaccorso, F., and Kymakis, E. A two-fold engineering approach based on Bi_2Te_3 flakes towards efficient and stable inverted perovskite solar cells. *Mater. Adv.*, 1:450–462, 2020. URL https://doi.org/10.1039/D0MA00162G.

[198] Jiménez-López, J., Cambarau, W., Cabau, L., and Palomares, E. Charge Injection, Carriers Recombination and HOMO Energy Level Relationship in Perovskite Solar Cells. *Scientific Reports*, 7(1):6101, Jul 2017. ISSN 2045-2322. URL https://doi.org/10.1038/s41598-017-06245-5.

[199] Ossila,. Spin Coating: Complete Guide to Theory and Techniques, . URL https://www.ossila.com/pages/spin-coating.

[200] Technology, G. Spin Coating process Troubleshooting. URL https://bit.ly/3fmcu2m.

[201] Martin-Palma, R. J. and Lakhtakia, A. Chapter 15 - Vapor-Deposition Techniques. In Lakhtakia, A. and Martin-Palma, R. J., editors, *Engineered Biomimicry*, pages 383–398. Elsevier, Boston, 2013. ISBN 978-0-12-415995-2. URL https://doi.org/10.1016/B978-0-12-415995-2.00015-5.

[202] Liu, T., Chen, K., Hu, Q., Zhu, R., and Gong, Q. Inverted Perovskite Solar Cells: Progresses and Perspectives. *Advanced Energy Materials*, 6(17): 1600457, 2016. URL https://doi.org/10.1002/aenm.2016004577.

[203] Kang, D.-H. and Park, N.-G. On the Current-Voltage Hysteresis in Perovskite Solar Cells: Dependence on Perovskite Composition and Methods to Remove Hysteresis. *Advanced Materials*, 31(34):1805214, 2019. URL https://onlinelibrary.wiley.com/doi/abs/10.1002/adma.201805214.

[204] Zhang, Z., Sheri, M., Page, Z. A., Emrick, T., Saeki, A., Liu, Y., and Russell, T. P. Understanding Hole Extraction of Inverted Perovskite Solar Cells. *ACS Applied Materials & Interfaces*, 12(50):56068–56075, Dec 2020. ISSN 1944-8244. URL https://doi.org/10.1021/acsami.0c18108.

[205] Stolterfoht, M., Caprioglio, P., Wolff, C. M., Mrquez, J. A., Nordmann, J., Zhang, S., Rothhardt, D., Hrmann, U., Amir, Y., Redinger, A., Kegelmann, L., Zu, F., Albrecht, S., Koch, N., Kirchartz, T., Saliba, M., Unold, T., and

Neher, D. The impact of energy alignment and interfacial recombination on the internal and external open-circuit voltage of perovskite solar cells. *Energy Environ. Sci.*, 12:2778–2788, 2019. URL https://doi.org/10.1039/C9EE02020A.

[206] Bidikoudi, M. and Kymakis, E. Novel approaches and scalability prospects of copper based hole transporting materials for planar perovskite solar cells. *J. Mater. Chem. C*, 7:13680–13708, 2019. URL https://doi.org/10.1039/C9TC04009A.

[207] Fan, X., Nie, W., Tsai, H., Wang, N., Huang, H., Cheng, Y., Wen, R., Ma, L., Yan, F., and Xia, Y. PEDOT:PSS for Flexible and Stretchable Electronics: Modifications, Strategies, and Applications. *Advanced Science*, 6(19):1900813, 2019. doi: 3. URL https://doi.org/10.1002/advs.201900813.

[208] Kim, S.-M., Kim, C.-H., Kim, Y., Kim, N., Lee, W.-J., Lee, E.-H., Kim, D., Park, S., Lee, K., Rivnay, J., and Yoon, M.-H. Influence of PEDOT:PSS crystallinity and composition on electrochemical transistor performance and long-term stability. *Nature Communications*, 9(1):3858, Sep 2018. ISSN 2041-1723. URL https://doi.org/10.1038/s41467-018-06084-6.

[209] Bracher, C., Freestone, B. G., Mohamad, D. K., Smith, J. A., and Lidzey, D. G. Degradation of inverted architecture $CH_3NH_3PbI_{3-X}cl_X$ perovskite solar cells due to trapped moisture. *Energy Science & Engineering*, 6(1): 35–46, 2018. URL https://doi.org/10.1002/ese3.180.

[210] Hu, L., Sun, K., Wang, M., Chen, W., Yang, B., Fu, J., Xiong, Z., Li, X., Tang, X., Zang, Z., Zhang, S., Sun, L., and Li, M. Inverted Planar Perovskite Solar Cells with a High Fill Factor and Negligible Hysteresis by the Dual Effect of NaCl-Doped PEDOT:PSS. *ACS Applied Materials & Interfaces*, 9(50):43902–43909, Dec 2017. ISSN 1944-8244. URL https://doi.org/10.1021/acsami.7b14592.

[211] Liu, X., Li, B., Zhang, N., Yu, Z., Sun, K., Tang, B., Shi, D., Yao, H., Ouyang, J., and Gong, H. Multifunctional RbCl dopants for efficient inverted planar perovskite solar cell with ultra-high fill factor, negligible hysteresis and improved stability. *Nano Energy*, 53:567–578, 2018. ISSN 2211-2855. doi: https://doi.org/10.1016/j.nanoen.2018.09.023.

[212] Jiang, K., Wu, F., Zhang, G., Chow, P. C. Y., Ma, C., Li, S., Wong, K. S., Zhu, L., and Yan, H. Inverted planar perovskite solar cells based on CsI-doped PEDOT:PSS with efficiency beyond 20% and small energy loss. *J. Mater. Chem. A*, 7:21662–21667, 2019. doi: https://doi.org/10.1039/C9TA08995K.

[213] Wang, Q., Chueh, C.-C., Eslamian, M., and Jen, A. K.-Y. Modulation of PEDOT:PSS pH for Efficient Inverted Perovskite Solar Cells with Reduced

Potential Loss and Enhanced Stability. *ACS Applied Materials & Interfaces*, 8(46):32068–32076, Nov 2016. ISSN 1944-8244. URL https://doi.org/10.1021/acsami.6b11757.

[214] Reza, K. M., Gurung, A., Bahrami, B., Mabrouk, S., Elbohy, H., Pathak, R., Chen, K., Chowdhury, A. H., Rahman, M. T., Letourneau, S., Yang, H.-C., Saianand, G., Elam, J. W., Darling, S. B., and Qiao, Q. Tailored PEDOT:PSS hole transport layer for higher performance in perovskite solar cells: Enhancement of electrical and optical properties with improved morphology. *Journal of Energy Chemistry*, 44:41–50, 2020. ISSN 2095-4956. URL https://doi.org/10.1016/j.jechem.2019.09.014.

[215] Al-Ashouri, A., Magomedov, A., Ro, M., Jošt, M., Talaikis, M., Chistiakova, G., Bertram, T., Mrquez, J. A., Khnen, E., Kasparaviius, E., Levcenco, S., Gil-Escrig, L., Hages, C. J., Schlatmann, R., Rech, B., Malinauskas, T., Unold, T., Kaufmann, C. A., Korte, L., Niaura, G., Getautis, V., and Albrecht, S. Conformal monolayer contacts with lossless interfaces for perovskite single junction and monolithic tandem solar cells. *Energy Environ. Sci.*, 12:3356–3369, 2019. URL https://doi.org/10.1039/C9EE02268F.

[216] Cao, Y., Chen, W., Sun, H., Wang, D., Chen, P., Djuri, A. B., Zhu, Y., Tu, B., Guo, X., Tang, B.-Z., and He, Z. Efficient Perovskite Solar Cells with a Novel Aggregation-Induced Emission Molecule as Hole-Transport Material. *Solar RRL*, 4(2):1900189, 2020. URL https://doi.org/10.1002/solr.201900189.

[217] Holzhey, P. and Saliba, M. A full overview of international standards assessing the long-term stability of perovskite solar cells. *J. Mater. Chem. A*, 6:21794–21808, 2018. doi: 10.1039/C8TA06950F. URL https://doi.org/10.1039/C8TA06950F.

[218] Wang, R., Mujahid, M., Duan, Y., Wang, Z.-K., Xue, J., and Yang, Y. A Review of Perovskites Solar Cell Stability. *Advanced Functional Materials*, 29(47):1808843, 2019. URL https://doi.org/10.1002/adfm.201808843.

[219] Lee, J. J., Lee, S. H., Kim, F. S., Choi, H. H., and Kim, J. H. Simultaneous enhancement of the efficiency and stability of organic solar cells using PEDOT:PSS grafted with a PEGME buffer layer. *Organic Electronics*, 26:191–199, 2015. ISSN 1566-1199. URL https://doi.org/10.1016/j.orgel.2015.07.022.

[220] Yun, J.-M., Yeo, J.-S., Kim, J., Jeong, H.-G., Kim, D.-Y., Noh, Y.-J., Kim, S.-S., Ku, B.-C., and Na, S.-I. Solution-Processable Reduced Graphene Oxide as a Novel Alternative to PEDOT:PSS Hole Transport Layers for Highly Efficient and Stable Polymer Solar Cells. *Advanced Materials*, 23(42):4923–4928, 2011. URL https://doi.org/10.1002/adma.201102207.

[221] Ma, S., Qiao, W., Cheng, T., Zhang, B., Yao, J., Alsaedi, A., Hayat, T., Ding, Y., Tan, Z., and Dai, S. Opticalβ€Electricalβ€Chemical Engineering of PEDOT:PSS by Incorporation of Hydrophobic Nafion for Efficient and Stable Perovskite Solar Cells. *ACS Applied Materials & Interfaces*, 10(4): 3902–3911, Jan 2018. ISSN 1944-8244. URL https://doi.org/10.1021/acsami.7b19053.

[222] Mann, D. S., Seo, Y.-H., Kwon, S.-N., and Na, S.-I. Efficient and stable planar perovskite solar cells with a PEDOT:PSS/SrGO hole interfacial layer. *Journal of Alloys and Compounds*, 812:152091, 2020. ISSN 0925-8388. URL https://doi.org/10.1016/j.jallcom.2019.152091.

[223] Chochos, C. L., Katsouras, A., Gasparini, N., Koulogiannis, C., Ameri, T., Brabec, C. J., and Avgeropoulos, A. Rational Design of High-Performance Wide-Bandgap (≈2 ev) Polymer Semiconductors as Electron Donors in Organic Photovoltaics Exhibiting High Open Circuit Voltages (≈1 v). *Macromolecular Rapid Communications*, 38(2):1600614, 2017. URL https://doi.org/10.1002/marc.201600614.

[224] Park, S., Heo, J. H., Cheon, C. H., Kim, H., Im, S. H., and Son, H. J. A [2,2]paracyclophane triarylamine-based hole-transporting material for high performance perovskite solar cells. *J. Mater. Chem. A*, 3:24215–24220, 2015. URL https://doi.org/10.1039/C5TA08417B.

[225] Sun, Y., Wang, C., Zhao, D., Yu, J., Yin, X., Grice, C. R., Awni, R. A., Shrestha, N., Yu, Y., Guan, L., Ellingson, R. J., Tang, W., and Yan, Y. A New Hole Transport Material for Efficient Perovskite Solar Cells With Reduced Device Cost. *Solar RRL*, 2(1):1700175, 2018. URL https://doi.org/10.1002/solr.201700175.

[226] Saliba, M., Matsui, T., Domanski, K., Seo, J.-Y., Ummadisingu, A., Zakeeruddin, S. M., Correa-Baena, J.-P., Tress, W. R., Abate, A., Hagfeldt, A., and Grätzel, M. Incorporation of rubidium cations into perovskite solar cells improves photovoltaic performance. *Science*, 354(6309):206–209, 2016. ISSN 0036-8075. doi: 7. URL https://doi.org/10.1126/science.aah5557.

[227] Liu, J., Liu, W., Aydin, E., Harrison, G. T., Isikgor, F. H., Yang, X., Subbiah, A. S., and De Wolf, S. Lewis-Acid Doping of Triphenylamine-Based Hole Transport Materials Improves the Performance and Stability of Perovskite Solar Cells. *ACS Applied Materials & Interfaces*, 12(21):23874–23884, May 2020. ISSN 1944-8244. URL https://doi.org/10.1021/acsami.0c03660.

[228] Xu, B., Zhang, J., Hua, Y., Liu, P., Wang, L., Ruan, C., Li, Y., Boschloo, G., Johansson, E. M., Kloo, L., Hagfeldt, A., Jen, A. K.-Y., and Sun, L. Tailor-Making Low-Cost Spiro[fluorene-9,9β-xanthene]-Based 3D Oligomers

for Perovskite Solar Cells. *Chem*, 2(5):676–687, 2017. ISSN 2451-9294. URL https://doi.org/10.1016/j.chempr.2017.03.011.

[229] Budiawan, W., Lai, K.-W., Karuppuswamy, P., Jadhav, T. S., Lu, Y.-A., Ho, K.-C., Wang, P.-C., Chang, C.-C., and Chu, C.-W. Asymmetric Benzotrithiophene-Based Hole Transporting Materials Provide High-Efficiency Perovskite Solar Cells. *ACS Applied Materials & Interfaces*, 12 (26), Jul 2020. ISSN 1944-8244. URL https://doi.org/10.1021/acsami.0c02204.

[230] Zhang, W., Wan, L., Fu, S., Li, X., and Fang, J. Reducing energy loss and stabilising the perovskite/poly (3-hexylthiophene) interface through a polyelectrolyte interlayer. *J. Mater. Chem. A*, 8:6546–6554, 2020. URL https://doi.org/10.1039/D0TA01860K.

[231] Du, X., Heumueller, T., Gruber, W., Classen, A., Unruh, T., Li, N., and Brabec, C. J. Efficient Polymer Solar Cells Based on Non-fullerene Acceptors with Potential Device Lifetime Approaching 10 Years. *Joule*, 3(1):215–226, 2019. ISSN 2542-4351. URL https://doi.org/10.1016/j.joule.2018.09.001.

[232] Chochos, C. L., Spanos, M., Katsouras, A., Tatsi, E., Drakopoulou, S., Gregoriou, V. G., and Avgeropoulos, A. Current status, challenges and future outlook of high performance polymer semiconductors for organic photovoltaics modules. *Progress in Polymer Science*, 91:51–79, 2019. ISSN 0079-6700. URL https://doi.org/10.1016/j.progpolymsci.2019.02.00.

[233] Tavakoli, M. M., Po, R., Bianchi, G., Carbonera, C., and Kong, J. Efficient and Stable Mesoscopic Perovskite Solar Cells Using a Dopant-free D-A Copolymer Hole-Transporting Layer. *Solar RRL*, 5(4):2000801, 2021. URL https://doi.org/10.1002/solr.202000801.